UC Berkeley
UC Berkeley Electronic Theses and Dissertations

Title
Single-Molecule Studies of Intraflagellar Transport in Chlamydomonas

Permalink
https://escholarship.org/uc/item/0qf2w9x8

Author
Shih, Sheng-Min

Publication Date
2014

Peer reviewed|Thesis/dissertation

eScholarship.org Powered by the California Digital Library
University of California

Single-Molecule Studies of Intraflagellar Transport in *Chlamydomonas*

By

Sheng-Min Shih

A dissertation submitted in partial satisfaction of the

requirements for the degree of

Doctor of Philosophy

In

Physics

in the

Graduate Division

of the

University of California, Berkeley

Committee in charge:

Professor Ahmet Yildiz, Chair
Professor Eva Nogales
Professor Michael DeWeese

Spring 2014

Abstract

Single-Molecule Studies of Intraflagellar Transport in *Chlamydomonas*

By

Sheng-Min Shih

Doctor of Philosophy in Physics

University of California, Berkeley

Professor Ahmet Yildiz, Chair

Intraflagellar transport (IFT) is a universal process that is required for the assembly and maintenance of all eukaryotic cilia and flagella. Defects in IFT are linked to a wide range of human diseases, including polycystic kidney disease and retinal degeneration. IFT has been implicated in sensory and motile ciliary functions, but the mechanisms of this relationship remain unclear.

We used *Chlamydomonas* flagellar surface motility (FSM) as a model to test whether IFT provides force for gliding of cells across solid surfaces, and whether IFT transports flagellar membrane glycoproteins (FMGs). We show that IFT trains are coupled to FMGs in a Ca^{2+}-dependent manner. IFT trains transiently pause through surface adhesion of their FMG cargos, and dynein-1b motors pull the cell towards the distal tip of the axoneme. Using the IFT-FMG linkage, we performed optical trapping studies to measure the force produced by single IFT trains. The stall force measurements show that each IFT train is transported by at least four active motors. Opposite-polarity motors are reciprocally coordinated to avoid a tug-of-war. Our results demonstrate the mechanism of *Chlamydomonas* gliding motility and suggest that IFT plays a major role in adhesion-induced ciliary signaling pathways.

To understand the regulation mechanism of IFT, key information needs to be acquired by monitoring IFT remodeling at the turnaround zones. However, the collective behavior of IFT particles poses unique challenges, because individual IFT trains often cannot be resolved at the flagellar tips and bases. We developed a photobleaching gate assay to track single molecules in dense specimens. The assay controls the number of fluorescent particles in a region of interest by photobleaching its boundary. To test this method, we tracked GFP-labeled receptors at a 100 ms temporal resolution on a live cell membrane, even though the

average distance between the receptors is less than 50 nm. We directly observed ligand-induced dimerization of epidermal growth factor receptor (EGFR) on a cell membrane.

We applied the photobleaching gate method to IFT in *Chlamydomonas*. We tracked individual IFT complexes along the length of a cilium and observed their remodeling at the ciliary tip. After transported by kinesin-2 to the flagellar tip, IFT trains split and recombine, and are transported back to the flagellar base bydynein-1b. Kinesin associated protein (KAP), on the other hand, diffuses back to the base after reaching the tip. On the basis of the results above, we propose new models for mixing and remodeling of IFT particles at the flagellar tip, coordination of IFT motors and flagellar length control.

This dissertation is dedicated to my family,
for always providing the support that I needed.

Table of Contents

Chapter 1. Intraflagellar Transport in *Chlamydomonas* 1
1.1 Intraflagellar Transport 1
1.2 Flagellar Surface Motility (FSM) in *Chlamydomonas* 3
Chapter 2. Retrograde IFT Trains Power Gliding Motility Through FMGs 4
2.1 Introduction 4
2.2 Methods 5
2.3 Results 7
2.4 Discussion 11
Chapter 3. Coordination of Kinesin-2 and Dynein on IFT Trains 24
3.1 Introduction 24
3.2 Methods 24
3.3 Results 27
3.4 Discussion 29
Chapter 4. Photobleaching Gate Assay 39
4.1 Introduction 39
4.2 Methods 40
4.3 Results 41
4.4 Discussion 44
Chapter 5. Single Molecule Analysis of IFT Turnover at Flagellar Tip of *Chlamydomonas* 51
5.1 Introduction 51
5.2 Methods 51
5.3 Results 53
5.4 Discussions 57
References 71

List of Figures

Figure 2.1 IFT transports FMG1B 13
Figure 2.2 Additional examples of simultaneous tracking of bead motility and IFT. 14
Figure 2.3 Dynein-1b drives gliding motility 15
Figure 2.4 The procedure for Fourier space direction analysis 16
Figure 2.5 Lag time between IFT pausing and initiation of gliding motility 17
Figure 2.6 Kymograph of gliding uniflagellate IFT27-GFP cells 18
Figure 2.7 Ciliobrevin D inhibits dynein-1b and stops gliding motility 19
Figure 2.8 Mechanisms of reversal in gliding motility 20
Figure 2.9 Ca^{2+} is required for the pausing of IFT trains at flagellar adhesion sites 22
Figure 2.10 The analysis of IFT pausing in the presence and absence of free Ca^{2+} in media 23
Figure 3.1 Stall force measurements on single IFT trains 31
Figure 3.2 Three additional examples of simultaneous bead trapping and IFT27-GFP fluorescence tracking 32
Figure 3.3 The offset between the bead position and IFT trains 33
Figure 3.4 Additional examples for bead motility under fixed trap 34
Figure 3.5 The effect of antibody concentration on peak forces measurements 35
Figure 3.6 Viscous drag of the membrane slows down the motility of IFT trains that carry beads 36
Figure 3.7 Measurement of viscous drag on bead movement along the surface of the flagellar membrane 37
Figure 3.8 Force measurements on temperature-sensitive mutants 38
Figure 4.1 MSD Plot of Non-Diffusive Behavior 45
Figure 4.2 Observing Single EGF Receptors with the Photobleaching Gate Assay 46
Figure 4.3 Photobleaching Gate Setup 47
Figure 4.4 Diffusion Study of EGF Receptors 48
Figure 4.5 Counting Fluorophores on EGFR Clusters 50
Figure 5.1 Photobleaching Gate Assay on *Chlamydomonas* IFT 59
Figure 5.2 Speed of IFT trains 60
Figure 5.3 1D Photobleaching Gate Setup 61
Figure 5.4 Additional Examples of Photobleaching Gate Result on IFT 62
Figure 5.5 Partial mixing of IFT trains at flagellar tips 63
Figure 5.6 Modeling the IFT Return Time 64
Figure 5.7 Calibration of the Cylindrical Lens 65
Figure 5.8 Sub-diffraction Limited Detection of IFT Trains 66
Figure 5.9 Additional Examples for High resolution Tracking of IFT27 67
Figure 5.10 Return of single KAP clusters 68
Figure 5.11 Measuring Diffusion Constant of KAP by the FRAP Assay 69

Figure 5.12 Additional Examples for High-resolution Tracking of KAP 70

Acknowledgements

First and foremost, I would like to thank my Professor, Ahmet Yildiz, for providing an opportunity and taking me on me as a student, colleague and friend these years. Words cannot express the gratitude I have for his unconditional support and the tremendous opportunities he has afforded me. This PhD would not have been possible without the guidance he has provided. It has truly been a privilege to work with and learn from such a successful scholar.

I would also like to express my gratitude to my collaborators Benjamin Engel, Wallace Marshall, Yongjian Huang, John Kuriyan, and Arne Gennerich who provided methodological support and inspiring suggestions as the project evolved. I sincerely appreciate the brilliant collaboration and the tireless support of such wonderful friends and colleagues.

Many others have of course contributed to my time here, and I will inevitably fail to mention most of them, but many thanks go out to Frank Cleary, Vlad Belyy, Jigar Bandaria, Mark DeWitt, Sara Wichner for wonderful ideas, and Huimin Huang and Pamela Duboc for helping me with the *Chlamydomonas* cells. I would also like to say a very special thank you to Thomas Bilyard for all of his help and all the useful discussions as the project developed. Finally, I would like to thank everyone else in the Yildiz groups; this work was made possible through your incredible support. Thank you all for the valuable input and for constantly reassuring me that there is a light at the end of the tunnel.

This PhD has provided me with countless opportunities to have intellectual sparkles and exchange of inspiring ideas with many other talents in the field. I have also developed skills that I never knew existed until I began this journey and one that I cannot imagine being without now. My sincerest gratitude goes to all my friends and colleagues from around the world who have embraced this work, supported my journey and made this PhD completely worthwhile. To be involved and working in such an incredible atmosphere filled with wonderful people is truly a blessing.

I would like to say a huge Thank You to Yvonne whom I met at UC Berkeley. As I have reached and accomplished a significant milestone academically, our new life adventure is just about to begin. I believe we can always conquer anything we put our hearts to and support each other just like how we have always been here for each other.

Finally, I would like to thank my wonderful family, mom, dad and my brother for their unconditional support and patience as I slowly establish myself in this world. I thank you for everything that you do for me.

Chapter 1. Intraflagellar Transport in *Chlamydomonas*

1.1 Intraflagellar Transport

The precise distribution of organelles and proteins in eukaryotic cells is mainly achieved through rapid and efficient transport of intracellular components (e.g. organelles, membranous vesicles, receptor molecules) to various destinations within the cytoplasm. Intraflagellar transport (IFT) is a type of intracellular transport that is highly conservative in all cilia and flagella in eukaryotes. Cilia and flagella (terms that refer to structurally identical organelles) are microtubule-based organelles that power the locomotion of many organisms, generate fluid flow over multiciliated surfaces, and mediate cell signaling (Liem et al., 2012). IFT is required for the assembly, maintenance, and sensory function of all eukaryotic cilia and flagella. Defects in IFT are linked to a wide range of human diseases, including polycystic kidney disease and retinal degeneration (Ishikawa and Marshall, 2011; Rosenbaum and Witman, 2002), and Bardet-Biedl syndrome (Lechtreck et al., 2009; Ou et al., 2005; Wei et al., 2012).

IFT was first discovered in *Chlamydomonas reinhardtii*. Using video-enhanced differential interference contrast (DIC) microscopy, Kozminski and colleagues observed granule-like particles moving bidirectionally along the length of the flagella (Kozminski et al., 1993). Under transmission electron microscopy (TEM), electronic dense particles are observed between the outer microtubule doublets and the flagellar membrane (Kozminski et al., 1993; Detler et al. 2005; Pederson et al. 2006; Pigino et al., 2009). Those particles, later named as IFT trains, are formed by repeated multiprotein complexes (Pigino et al., 2009). IFT trains are in close contact with the flagellar membrane, and they carry receptors, ion channels, and other membrane proteins, in addition to axonemal precursors required for flagellar elongation and maintenance (Qin et al., 2004; Qin et al., 2007; Rosenbaum and Witman, 2002). IFT trains are also connected to the outer microtubule doublets by the motor proteins, which provide force to transport the IFT trains back and forth along the flagellum.

The first motor protein identified in IFT is *fla10*, a kinesin-like protein, later identified as the kinesin-2 heavy chain. EM immunogold localization of *fla10* shows that they are located between outer microtubule doublets and the flagellar membrane (Kozminski et al., 1995). In addition to two heavy chains, kinesin-2 also has an accessory subunit, KAP (*fla3*) that is required for localization of kinesin-2 to the site of flagellar assembly and anterograde transport of IFT trains (Mueller et al., 2005). KAP is highly conserved and forms a large globular domain at the base of the kinesin-2 complex (Wedaman et al. 1996, Yamazaki et al. 1996). Temperature-sensitive (*ts*) mutation of *fla3* affects IFT and flagellar assembly at the permissive temperature and leads to deflagellation at the restrictive temperature (Mueller et al., 2005). The *ts* mutant of *fla10* leads to absence of IFT transport at the restrictive

temperature and flagellum shrinking, showing that kinesin is the anterograde motor required for IFT and maintenance of the flagella (Kozminski et al., 1995). Similarly, mutations in kinesin-2-related sequences inhibit the assembly of motile cilia in *Tetrahymena* (Brown et al. 1999) and sensory cilia in *C. elegans* (Shakir et al. 1993) and *Drosophila* (Sarpal et al. 2004).

LC8, a dynein light chain, is the first retrograde motor subunit identified to be associated with IFT. LC8 mutant has short flagella compared to WT, and retrograde IFT movement was not present under both DIC and EM imaging (Pigino et al., 2009; Parzour et al., 1998). However, LC8 is also present in the dynein arms and radial spoke, so it was not specific to IFT. A dynein heavy chain (DHC1b) is later found to be essential for IFT. Unlike LC8, DHC1b is specific to retrograde transport of IFT trains. DHC1b mutant has very short flagella with IFT trains accumulate at the flagellar tips (Parzour et al., 1998).

IFT trains move unidirectionally from the basal body at the flagellar base to the flagellar tip, switch direction, and move unidirectionally back to the flagellar base. Therefore, IFT is an ideal model system to study how opposite polarity motors are coordinated to determine the distribution and delivery of intracellular cargos. In *Chlamydomonas*, IFT remains unabated for hours after the complete inhibition of protein synthesis, suggesting that motors need to be recycled in this process (Iomini et al. 2001). Early models suggested that dynein is transported as a cargo by kinesin toward the flagellar tip, and kinesin is transported back to the flagellar base by the retrograde trains (Rosenbaum and Witman, 2002). However, there was evidence showing that kinesin-2 can exit the flagella independent of the dynein-1b light intermediate chain (LIC) and IFT particles (Pederson et al., 2006). It remained unknown whether the opposite polarity motors operate in a tug-of-war manner, in which kinesin and dynein pull against each other, or in a coordinated manner, in which only kinesin or dynein is active at a time.

Chlamydomonas is a simple and robust IFT model system that provides unique advantages to address these questions:

- In flagella, all microtubules are stable and unipolar, with the plus ends located at the tip of the flagella.
- Only two motor proteins, kinesin-2 and dynein-1b are involved in the transport.
- Autofluorescence of a flagellum is negligible because it extends out of the cell body, and there is no pigment or chloroplast in the flagellum.
- The motility of *Chlamydomonas* flagella has been studied for decades, and various mutants on IFT cargos and motors are available in *Chlamydomonas* database.
- The flagella can be paralyzed and immobilized on the glass surface, which allows us to apply single-molecule techniques such as total internal reflection microscopy (TIRF) and optical trapping.

1.2 Flagellar Surface Motility (FSM) in *Chlamydomonas*

Chlamydomonas is a major model organism to study ciliary beating and swimming motility. It uses breast-stroke beating behavior to swim in liquid environments. This beating motility is powered by inner and outer dynein arms, and radial spokes in the axoneme. The axoneme is formed by nine outer microtubule doublets and two central microtubules. The radial spokes located on the outer doublets are used to move with respect to the central microtubules, and the dynein arms, which are also located on the outer doublets, are used to move with respect to the other outer doublets. Therefore, axonemes bends in patterned behavior that enables beating motility.

Although *Chlamydomonas* can translocate rapidly by swimming motility, it mostly attaches to a solid substrate in nature and uses gliding motility for translocation. In order to glide, *Chlamydomonas* adheres one or both of its flagella to the surface. Gliding motility is central to understanding the function and evolution of cilia, as it may have existed in early cilia before the establishment of axonemal beating. Cells are able to glide even though axonemal bending described above is inhibited in paralyzed flagella (*pf*) mutants, suggesting that swimming and gliding motilities are driven by distinct force production mechanisms. However, force generation mechanism for gliding motility remained unclear. Flagellar membrane surface is highly dynamic and beads attach to the flagellar surface and perform saltatory movement toward both directions (Bloodgood 1995). It is possible that the transport of IFT trains underneath the flagellar membrane provide force to the exterior of a flagellum. However, IFT and gliding motilities differ in many aspects, and it has been proposed that these two processes are driven by different force generation mechanism (Bloodgood and Salomonsky, 1990).

In this dissertation, I use single-molecule techniques to investigate gliding and bead motility, and their interaction with IFT in *Chlamydomonas* cells. Later, I focus on the dynamics of IFT trains at the flagellar tip to investigate the coordination of IFT motors and flagellar length control.

Chapter 2. Retrograde IFT Trains Power Gliding Motility Through FMGs

2.1 Introduction

Cell motility plays crucial roles in the development, survival and mating of many eukaryotes. Cilia and flagella are microtubule-based organelles that power the locomotion of many organisms, generate fluid flow over multiciliated surfaces, and mediate cell signaling. *Chlamydomonas* is a unicellular biflagellate alga that exhibits two different types of whole-cell motility, both of which involve flagella. Cells swim in water through a breast-stroke motion of their two flagella and glide over solid surfaces (Bloodgood, 2009). The mechanism of gliding motility appears to be distinct from swimming; a wide range of mutant strains deficient in axonemal bending have unaffected cellular gliding (Bloodgood and Salomonsky, 1990; Kozminski et al., 1993). The force transduction mechanism for gliding is not well understood, but it may involve a minus-end directed microtubular motor and formation of adhesion points between the flagellar membrane and the surface (Bloodgood, 2009).

The flagellar membrane of *Chlamydomonas* exhibits dynamic features, such as the directed movement of flagellar membrane glycoproteins (FMGs) along the flagellar membrane of vegetative cells and the migration of flagellar contact sites during mating (Bloodgood, 2009). FMG1B, the most abundant FMG in *Chlamydomonas*, is a 410 kDa protein that consists of an unusually short (17 amino acids) C-terminal cytoplasmic tail, a single transmembrane domain, and a large extracellular domain with many N-glycosylation sites (Bloodgood, 2009). Gliding motility and microsphere movement both require ligation of FMG1B into large clusters (Bloodgood and Salomonsky, 1998), which is accompanied by a Ca^{2+} dependent signaling pathway and dephosphorylation of a gliding-associated kinase (Bloodgood and Salomonsky, 1994).

Microsphere movement and gliding motility may share the same force-transduction machinery, as they move at comparable speed (Bloodgood, 1977) and most non-gliding mutant strains also have defects in microsphere motility (Bloodgood and Salomonsky, 1990). However, certain mutants defective in gliding motility do display microsphere movement (Kozminski et al., 1995), suggesting that there are distinct features between the two processes. While gliding is driven by the pulling motion of the leading flagellum, microsphere movement is bidirectional (Bloodgood, 1977), implying that the two motilities may employ different types of microtubule motors (Bloodgood, 2009).

Intraflagellar transport (IFT) trains appear to make multiple connections with the flagellar membrane (Kozminski et al., 1995), suggesting that IFT may generate force for gliding and microsphere motility. Supporting this hypothesis, inhibition of kinesin-2 in the temperature-sensitive mutant *fla10*^{ts} stops both IFT and gliding motility (Kozminski et al.,

1995). However, IFT differs significantly from FSM in that it is unidirectional and processive along the length of the flagellum (Dentler, 2005; Iomini et al., 2001), moves at faster speeds, and is calcium independent (Kozminski et al., 1993). There is currently no direct evidence that IFT carries FMGs as cargo (Qin et al., 2004), and in *fla10*^{ts} gametes, sexual agglutinins can migrate from cell bodies into flagella in the absence of IFT (Pan and Snell, 2002). Mutations of the LC8 subunit of dynein-1b do not inhibit microsphere movement (Pazour et al., 1998), but gliding motility cannot be reliably assayed in these mutants because they have very short flagella. The motors for FSM may be different than those that drive IFT. It has been suggested that a minus-end directed kinesin calmodulin-binding protein (KCBP), which is localized to *Chlamydomonas* flagella (Dymek et al., 2006), may be specifically involved in gliding motility.

In this chapter, we investigated three types of flagellar motility in live *Chlamydomonas* cells using a combination of advanced single-molecule techniques. We observed that FMG1B rapidly associate and dissociate from IFT trains and are transported by IFT back and forth along the flagellum. Retrograde IFT trains transiently pause along the length of flagellum and dynein-1b motors attached to paused IFT trains produce a pulling force upon the microtubule track, causing the whole cell to start gliding in the opposite direction. A single IFT train is transported by multiple motors in both directions, and opposite-polarity motors do not engage in a tug-of-war on their cargo. On the basis of these findings, we provide a mechanistic model for the regulation of IFT and the production of FSM.

2.2 Methods

Strains and Culture Conditions

Vegetative *Chlamydomonas reinhardtii* cells were grown in Tris-acetate-phosphate (TAP) media in an illuminated plant growth chamber at 22 ℃. Wild-type mt+ (cc125), *pf18* mt- (cc1297), and *pf18* mt+ (cc1036) strains were obtained from the *Chlamydomona* Resource Center. The IFT20-GFP ΔIFT20 strain was provided by K. Lechtreck and G. Witman. The IFT27-GFP mt+ strain and *pf1 fla10-1*^{ts} were provided by J. Rosenbaum. IFT27-GFP *pf18* strain was generated through crosses (Engel et al., 2009). *pf1 fla10-1*^{ts} cells were incubated at 37 ˚C for 15 min for heat inactivation of kinesin-2, and the data were collected within 30 min at 37 ˚C, before the complete impairment of IFT and the start of flagellar resorption (Kozminski et al., 1993). In *dhc1b-3*^{ts} mt- mutant strain (cc4422) (Engel et al., 2012), dynein-1b is inhibited after 6-hour incubation at 37 ℃. Paralyzed flagella (*pf*) strains and paralyzing compounds (Engel et al., 2011) were utilized to impair swimming motility. Ciliobrevin D was dissolved in DMSO and then added to the *pf18* cell culture to inhibit dynein activity. IFT and gliding motility were recorded simultaneously 2 minutes after addition of 0 – 150 μM ciliobrevin D to the flow chamber.

Single-Molecule Fluorescence Imaging

The IFT and FSM imaging assays were performed with an objective-type total internal reflection fluorescent (TIRF) microscope (DeWitt et al., 2012). The GFP signal was recorded by an electron multiplied charge-coupled device (EM-CCD) camera (Andor), with an effective pixel size of 106 nm. IFT27-GFP *pf18* and IFT20-GFP ΔIFT20 strains were used for tracking individual IFT trains (Engel et al., 2009). The sample chamber was pre-treated with 0.7 mg/ml poly-L-lysine to adhere flagella on a glass surface. 15 µl cells in TAP media were applied to cover glass and inverted onto slides. Gliding motility assays were performed without polylysine treatment and cells were imaged under bright-field illumination. *ts* mutants were assayed at permissive (22 ˚C) and restrictive (37 ˚C) conditions by controlling the temperature with an objective heater (Bioptechs). Because paralyzed cells glide 30-40% faster than non-paralyzed cells (Bloodgood, 1995), gliding speeds of *ts* mutants of kinesin-2 (*pf1 fla10-1*^{ts}) and dynein-1b (*dhc1b-3*^{ts}) were compared to those of both *pf18* and WT cells at permissive (22 ℃) and restrictive (37 ℃) temperatures.

Bead-Motility Imaging

To visualize bead movement along the flagellar surface, 200-nm carboxyl-modified nile-red fluorescent beads (Invitrogen) were coated with anti-FMG1B antibody (Bloodgood et al., 1986) by EDC-NHS cross linking. 1 mL *pf18* cell culture was spun down at 400 *g* for 1 min and resuspended in 100 µL 5-fold diluted TAP media. 1 µL bead stock solution (25 mg/ml) was then added to 20 µL of resuspended cell culture and the mixture was incubated in ice for 10 minutes, in order to slow down IFT movement for bead attachment. 1 µL of 20mM $CaCl_2$ was then added, the cell culture was incubated at room temperature for 10 minutes for bead movement to recover. To immobilize cells on a glass surface, the cover glasses (18 x 18 mm) were pre-treated with 0.7 mg/ml poly-L-lysine (MW = 150-300 kDa, Sigma) for 5 minutes. The nile-red beads fluorescence was recorded with Andor iXon 128x128 EM-CCD at 400 µs per frame. To prevent deflagellation of cells under intense (100 mW) laser illumination, only the flagellar regions of immobilized cells were excited. Flagellar membrane adsorption of carboxylated 100 nm beads was significantly reduced without antibody crosslinking (~50 fold), and only two bead motility events were observed in 500 cells.

Multicolor-Tracking Assays

To simultaneously monitor the movement of IFT-trains and FMG1B proteins, IFT27-GFP *pf18* cells were incubated with anti-FMG1B coated dark-red beads. The GFP and dark-red bead fluorescence were simultaneously recorded at 200 ms per frame. The crosstalk between the two fluorescent channels was below 0.1%. The image was split into two fluorescent channels, which were registered to a sub-pixel accuracy (DeWitt et al., 2012) with respect to each other, prior to live-cell imaging.

Various concentrations of EGTA were added to IFT27-GFP pf18 cells grown in TAP media (contains 0.34 mM of Ca^{2+}) and the data were collected within 15 minutes after EGTA addition. The concentration of free Ca^{2+} in the assay buffer as a function of added EGTA was calculated from the Chelator program (http://maxchelator.stanford.edu). Only the cells with fully grown flagella (8-12 μm in length) were analyzed. Immotile IFT trains from the beginning to the end of the image acquisition were excluded from data analysis. The pausing frequency was calculated from dividing the total number of pausing events by the image acquisition time.

Data Analysis

Speeds were measured from linear fits to the displacement traces observed in kymographs. In order to distinguish between IFT trains moving in anterograde and retrograde directions and IFT trains pausing over a period of time, we assigned different colors to individual IFT trains as a function of their velocity by Fourier space directional analysis (Figure 2.4). The image was then transformed back into real space to recover the kymographs. To perform IFT kymography analysis during gliding motility, we separately determined the position of IFT trains relative to the cell body, and the position of the cell body relative to the glass surface (Figure 2.6). Correlation between the movements of beads and IFT trains were demonstrated by rejecting the null hypothesis (IFT and bead movement was uncorrelated) using Kolmogorov-Smirnov statistics.

2.3 Results

To dissect the mechanism of FSM, we directly observed IFT, FMG1B and gliding motilities using single-molecule imaging techniques. We monitored the movement of individual IFT trains by using TIRF illumination to image *pf* mutant cells that had adhered to the glass surface with both flagella. To establish a link between FMG1B transport and IFT, we simultaneously tracked the movement of FMG1B antibody-coated fluorescent beads (200 nm diameter, dark red) and IFT27-GFP in the pf18 strain. The beads performed short processive runs with reversals of direction whereas IFT trains moved in a regular and unidirectional manner. Multicolor kymography analysis shows that the beads transiently dissociated from one IFT train, diffused for a period of time and then bound to another IFT train (Figure 2.1A) similar to the movement of extraflagellar particles observed along the flagellar membrane (Dentler, 2005). Diffraction-limited images of beads and IFT trains were fitted to a two-dimensional Gaussian to achieve a higher localization precision (Yildiz et al., 2003). Figure 1B shows the colocalization of a membrane-attached bead with an individual IFT train as it moves unidirectionally for >500 nm. The movements of the bead and the colocalized IFT trains correlate strongly (>0.99) with each other during the processive run (N = 30, see Figure 2.1B, and Figure 2.2 for more examples), excluding the possibility that microspheres coincidentally moved together with IFT trains. We measured the distance

between microspheres and the nearest IFT trains moving in the same direction for both the experimental data and randomly generated kymographs. The Kolmogorov-Smirnov test ($p = 7 \times 10^{-9}$, Figure 2.1C) demonstrates that IFT trains colocalize with FMG1B along the flagellar membrane (Figure 2.1D).

We next investigated whether IFT plays a direct role in gliding motility by monitoring individual IFT trains in IFT20-GFP and IFT27-GFP pf18 cells as they glided on coverslips. A small fraction of IFT trains displayed rare pauses (0.125 s^{-1} per cell, $N_{cells} = 23$, $N_{pauses} = 247$) as they moved either in the retrograde or anterograde direction. Remarkably, the pausing of IFT trains was required for the initiation of whole-cell movements (Figure 2.3A and Figure 2.4). We did not observe the start of a gliding event without a paused IFT train. We were able to determine the directionality of 60% of the paused IFT trains, and all of the trains correspondent to the initiation of gliding motility stopped moving during retrograde transport (N = 148). To rule out the possibility that IFT pausing events and initiation of gliding motility are simply coincidental, we quantified the lag time between the pausing of the last retrograde IFT train and the initiation of gliding motility. The average lag time was 0.48 ± 0.05 s. In comparison, we observed individual IFT pausing events (including both anterograde and retrograde pauses) every 8.25 ± 0.96 s per cell. The student's t-test excludes the null hypothesis that the timing of retrograde IFT pausing and gliding motility are independent of each other (p-value <0.0001). Anterograde trains also displayed rare pauses (~0.02 s^{-1} per cell, N = 27), but we never observed pausing of an anterograde train before the initiation of gliding motility.

In 24% of all cases (N = 50), a single paused train appeared sufficient to pull the entire cell (Figure 2.3A). In other cases, multiple trains paused before the start of gliding motility (Figure 2.3B). Pauses occurred in the leading flagellum, and cells moved in the opposite direction relative to the transport trajectory of the paused trains. Gliding motility either stopped when paused IFT trains resumed movement (Figure 2.3A), or continued until the cell bodies reached the paused trains (Figure 2.3B). We never observed the cell body gliding further than the position of the paused IFT train(s).

We found compelling evidence that dynein-1b is the primary motor responsible for gliding motility. First, uniflagellate wild-type (WT) cells always glided with the flagellum leading the cell body at 1.49 ± 0.10 µm/s (mean ± s.e.m.) (Figure 2.3C, Figure 2.5) (Bloodgood, 2009), suggesting that gliding motility is driven by pulling forces generated through a minus end directed microtubular motor. In contrast to WT cells, uniflagellate dynein-1b ts cells (*dhc1b-3*^{ts}) (Engel et al., 2012) were unable to display robust gliding at restrictive temperatures. We observed only short-range (<500 nm) gliding-like motion in 54% of these cells, compared to robust unidirectional gliding motility observed over 5 µm in WT cells. These short-range motions were bidirectional (Figure 2.6) and significantly slower (forward: 0.35 ± 0.09 µm/s, backward: 0.47 ± 0.16 µm/s) than the gliding speed of WT cells

(Figure 2.3C, Figure 2.6). Second, inactivation of dynein-1b in biflagellate *dhc1b-3^{ts}* cells decreased the fraction of gliding cells from 100% to 52% and reduced the gliding speed from 0.86 ± 0.08 µm/s to 0.18 ± 0.03 µm/s. In contrast, inactivation of kinesin-2 in *fla10^{ts}* cells resulted in a two-fold increase in gliding speed (Figure 2.3D), indicating that kinesin plays an inhibitory role during dynein-1b driven gliding motility. These results agree with our observations that the pausing of anterograde trains does not initiate gliding motility.

To further test the role of dynein 1b in gliding motility, we treated the cells with a small molecule inhibitor of dynein, ciliobrevin D (Firestone et al., 2012). We treated cells with 0 – 150 µM ciliobrevin D and monitored IFT in surface-immobilized cells 2 minutes after drug treatment (Figure 2.7A). Both anterograde and retrograde IFT train frequencies dropped with increasing concentrations of ciliobrevin D (Figure 2.7B), and at >100 µM ciliobrevin D we observed accumulation of IFT trains at the flagellar tip (see example kymograph in Figure 2.7A). At 150 µM ciliobrevin D, retrograde IFT frequency was reduced by 92% compared to the 70% decrease observed after 6 hours of heat inactivation of *dhc1b-3^{ts}* cells (Engel et al., 2012). The velocities of retrograde and anterograde trains also decreased by 60% and 36%, respectively (Figure 2.7C). Importantly, inhibition of dynein-1b resulted in a significant reduction in the speed (79%) and frequency (79%) of gliding motility (N = 50, Figure 2.7D). These results further support our conclusion that dynein 1b motors produce the force for gliding motility.

Based on these results, we propose a model to describe the function of IFT motors, IFT trains and FMG1B transport in gliding motility (Figure 2.3E). Surface adhesion of the FMG1B cargo through its large extracellular carbohydrate domain (Bloodgood, 2009) stops the retrograde IFT train. Dynein motors previously engaged in transporting the paused IFT train exert force towards the microtubule minus end, causing the whole cell to move toward the plus-end flagellar tip. Thus, gliding motility works similarly to microtubule gliding assays, in which surface-immobilized dyneins glide microtubules with their plus-end tips in the lead.

To investigate how cells reverse gliding direction, we developed a kymography method for monitoring IFT trains as the cells reorient their flagella during gliding (Figure 2.8A–B, Video 5). During 60% of reversals (N = 40), the cell lifted one of its flagella and the paused IFT trains on the surface-adhered flagellum drove the motility (Bloodgood, 2009). In other cases, single or multiple paused IFT trains accumulated in one flagellum, and the cell body glided toward this cluster until the paused trains either detached from the glass surface or reached the flagellar base. We also observed cases with paused IFT trains in both flagella where the cell remained immotile, likely due to the balance of forces between bound dynein-1b motors (Figure 2.8C–D). There were no indications of coordination of the pausing events between the two flagella. Different modes of reversals in gliding motility may allow cells to

search through the environment by a random walk when they adhere both of their flagella, and to move in unidirectional manner by lifting one of the flagella.

Gliding motility in *Chlamydomonas* is controlled by a Ca^{2+}-calmodulin regulated kinase and requires micromolar levels of Ca^{2+} in the media (Bloodgood and Spano, 2002). We tested whether the pausing of IFT trains depends on Ca^{2+} (Figure 2.9A–B) by analyzing the kymographs of IFT at different Ca^{2+} concentrations. To quantify pausing in flagella, we used Fourier space direction analysis (FSDA, see Figure 2.4) to separate the traces of paused IFT trains and moving IFT trains into two kymographs. Kymographs of paused IFT trains in Figure 5A,B show that pausing along the length of the flagellum was significantly reduced in Ca^{2+}-deprived cells (see additional examples in Figure 2.10). After Ca^{2+} depletion, IFT trains rarely paused in the middle regions of flagella and accumulated at the base (Figure 2.9B, middle). Figure 5C plots the total fluorescence intensity of paused IFT trains (N_{cells} = 30 for each case) along the lengths of flagella at different Ca^{2+} levels. The frequency of pausing in Ca^{2+}-deprived cells was significantly lower than IFT pausing in cells at a normal Ca^{2+} concentration. In regular TAP media (free [Ca^{2+}] = 0.34 mM), 95% of all surface-adhered cells displayed gliding motility and individual pausing events were observed every ~8 s per flagellum, on average. In contrast, both the fraction of gliding cells and IFT pausing frequency were reduced by ~10-fold at <1 μM Ca^{2+} (Figure 2.9D). Next, we compared the IFT pausing frequencies in gliding and non-gliding cells at different Ca^{2+} levels. The pausing frequency in non-gliding cells was low and independent of Ca^{2+} concentration. In contrast, the pausing frequency in gliding cells was high at normal Ca^{2+} levels and gradually declined to match that of non-gliding cells as the Ca^{2+} concentration decreased below 1 nM (Figure 2.9E).

In Ca^{2+}-deprived cells, the beads freely diffused on the flagellar membrane but did not move processively by IFT trains (not shown). Thus, we propose that Ca^{2+} is required for attachment of FMG1B to IFT trains, not for the activation of a motor protein that provides force for gliding, as previously suggested (Bloodgood, 2009). As the flagellar membrane is enriched with a PKD2-like Ca^{2+} channel (Pazour et al., 2005; Huang et al., 2007), Ca^{2+} signaling at flagellar adhesion sites may play a role in controlling the directionality and timing of gliding movement.

2.4 Discussion

The gliding of cells along surfaces is a common mechanism of cell motility. In Toxoplasma gondi, cell motility is driven by a glideosome. The glideosome contains myosin A and aldolase, which mediates the interaction between actin and surface adhesion (Jewett and Sibley, 2003). In the gram-negative bacterium Myxococcus xanthus, the proton motive force drives gliding motility. MotA/B motors form multi-motor stationary complexes on the cell periphery and drive the rotation of the helical MreB filamentous track to translocate the cell (Nan et al., 2011; Sun et al., 2011). The flagella-based gliding motility of *Chlamydomonas* differs from metazoan cell locomotion, which utilizes actin polymerization and myosins for force generation. In *Chlamydomonas*, the microtubule cytoskeleton is involved in force generation, and only the interactions between the flagellar plasma membrane and the surface contribute to gliding motility.

We present direct evidence for the mechanism of IFT-mediated cell-surface interactions using *Chlamydomonas* gliding motility and FMG transport as a model system. In *Chlamydomonas*, IFT trains carry FMG1B as a cargo. Interaction between IFT trains and FMG1B clusters is transient, as FMG1B board moving trains but usually unload and diffuse away before the trains arrive at the other end of flagellum. During gliding motility, IFT trains pause due to attachment of the FMG1B cargo to the surface and the dynein-1b motors engaged to the paused IFT trains generate pulling forces along the microtubule long axis. While the majority of organismal motilities rely on the actin cytoskeleton or axonemal beating, gliding motility in *Chlamydomonas* is distinct in that it is powered by intracellular transport machinery along microtubules. By providing surface adhesion points, FMGs perform an analogous function to integrins in mammalian cell motility (Bloodgood, 2009; Lecuit et al., 2011).

Our results demonstrate how different types of flagellar motility in Chlamydomonas have distinct characteristics despite being driven by the same forces. First we showed that viscous drag of the membrane slows down the motility of IFT trains that carry FMG-conjugated beads, causing gliding motility and FMG transport to proceed slower than IFT. Second, previous work showed that IFT is unaffected by changes in environmental Ca^{2+} concentration, whereas gliding motility is Ca^{2+}-dependent (Bloodgood and Salomonsky, 1990). This raised the possibility that Ca^{2+} may be required to activate a specific motor protein that provides force for gliding (Bloodgood, 2009). Our results are inconsistent with this hypothesis. We found that the presence of free Ca^{2+} leads to frequent pauses in IFT motility at flagellar adhesion sites. In the absence of Ca^{2+}, IFT moves unidirectionally without interruptions, suggesting that attachment of FMGs to IFT trains is regulated by a Ca^{2+}-dependent signaling pathway. The signaling pathway responsible for linking FMGs to IFT is incomplete. There is evidence that surface adhesion or crosslinking of FMGs into large clusters induce dephosphorylation of a transmembrane protein coimmunoprecipitates with

FMG (Bloodgood and Salomonsky, 1990, 1998). The complex may be regulated by a calcium-calmodulin dependent gliding associated kinase (GAK), which is required for the gliding motility (Bloodgood and Spano, 2002). Further investigation is required to identify the rest of the signaling pathway regulating IFT-flagellar surface interactions.

The mechanism we described for IFT pausing and force generation has broad implications for the traffic of ciliary sensory proteins as well as cell signaling at ciliary membrane adhesion points (Wang et al., 2006). For example, IFT is required for the signal transduction during the mating of ciliated organisms. The initial interaction between gametes of two mating types in *Chlamydomonas reinhardtii* can occur at any point along their flagellar membranes, but the tips of their flagella must be aligned and locked before activating gametic fusion. IFT trains transport sexual agglutinins within the flagellar membrane of gametic cells (Ferris et al., 2005). Adhesion between sexual agglutinins of opposite cell types may stall retrograde IFT movement. As a result, forces produced by IFT trains would move the flagellar contact points until a balance of forces is achieved when the flagella are properly aligned with respect to each other. Indeed, microspheres have been observed to move and accumulate at the flagellar tips during mating (Hoffman and Goodenough, 1980). We propose that the absence of retrograde bead movement may be related to the formation of adhesion contacts between the flagella and pausing of retrograde trains.

Cilia in the retina, liver, and kidney cells were recently observed to make direct physical contacts, which may serve as "bridges" for signaling networks between many cells (Ott et al., 2012). These contacts are tight adhesions between the ciliary membranes, mediated by N-linked glycoproteins. It is possible that IFT exerts force on cell-cell adhesion sites and determines the positioning of these adhesion sites by moving them along the length of the cilium. Ca^{2+} signaling at flagellar adhesion sites may play a major role in regulating attachment of IFT trains and controlling the direction of force generation. We believe that the assay we developed will be a starting point for deciphering the role of IFT in signaling, mating and development of ciliated cells.

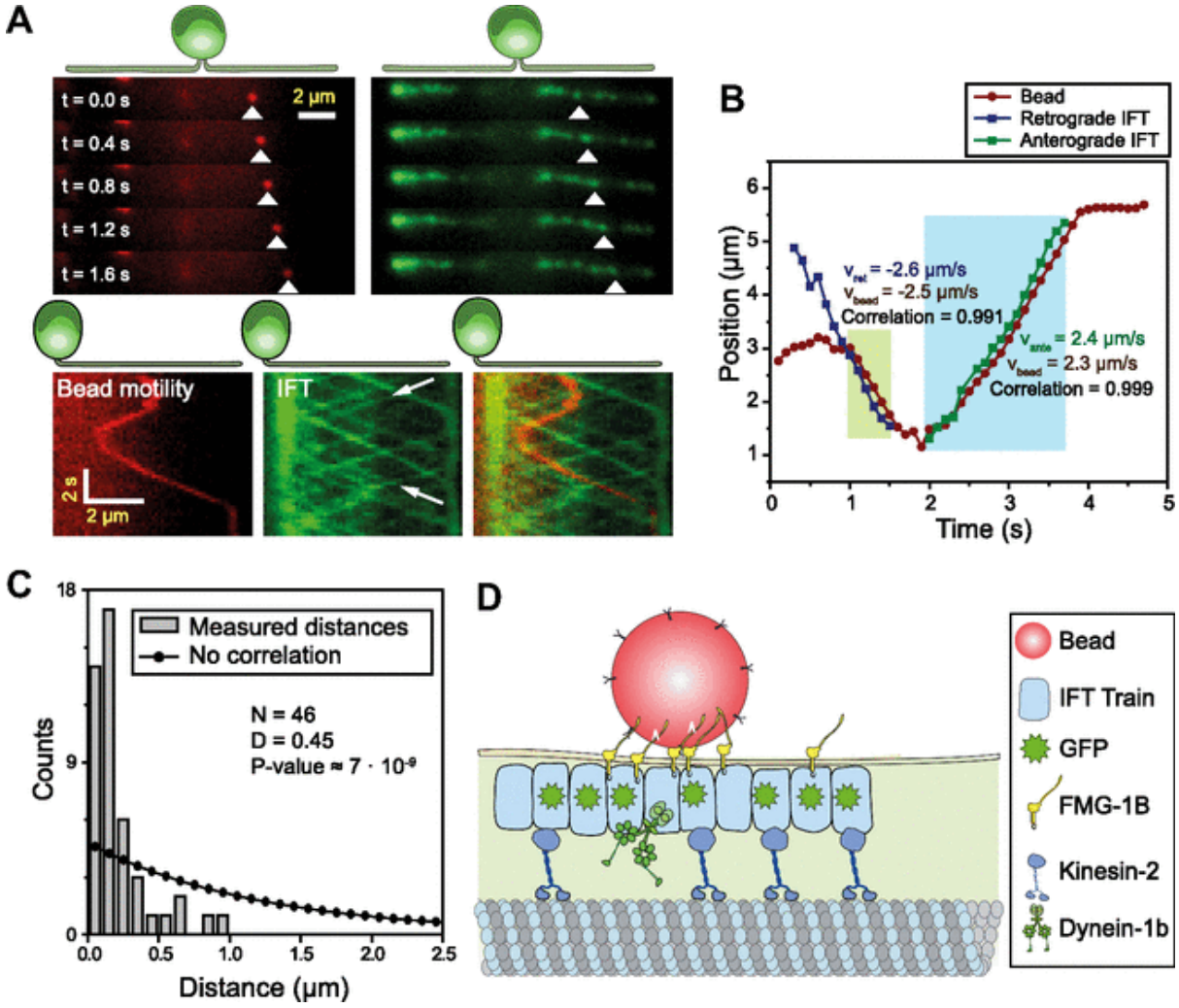


Figure 2.1 IFT transports FMG1B

(A) (Top) Simultaneous tracking of anti-FMG1B beads (red) and IFT27-GFP (green). (Bottom) Kymographs show that bead motility colocalizes with IFT trains during processive runs. Between the runs, the bead transiently attaches to and detaches from IFT trains. The white arrows indicate the IFT trains transporting the bead.

(B) Two-dimensional Gaussian fitting of the bead and IFT trains show that bead motility correlates strongly (>0.99) with the movement of individual anterograde (green shaded region) and retrograde (blue shaded region) IFT trains. The bead moves at similar speeds to IFT trains in both anterograde and retrograde directions.

(C) Comparison of distances from beads to the closest IFT train moving in the same direction (grey bars) to the predicted distribution without correlation (null hypothesis, black line). Kolmogorov-Smirnov statistics indicate that bead and IFT train positions strongly correlate with each other.

(D) A model for IFT particles transporting FMG1B. The bead is attached to FMG1B in the flagellar membrane through antibody linkages (not to scale).

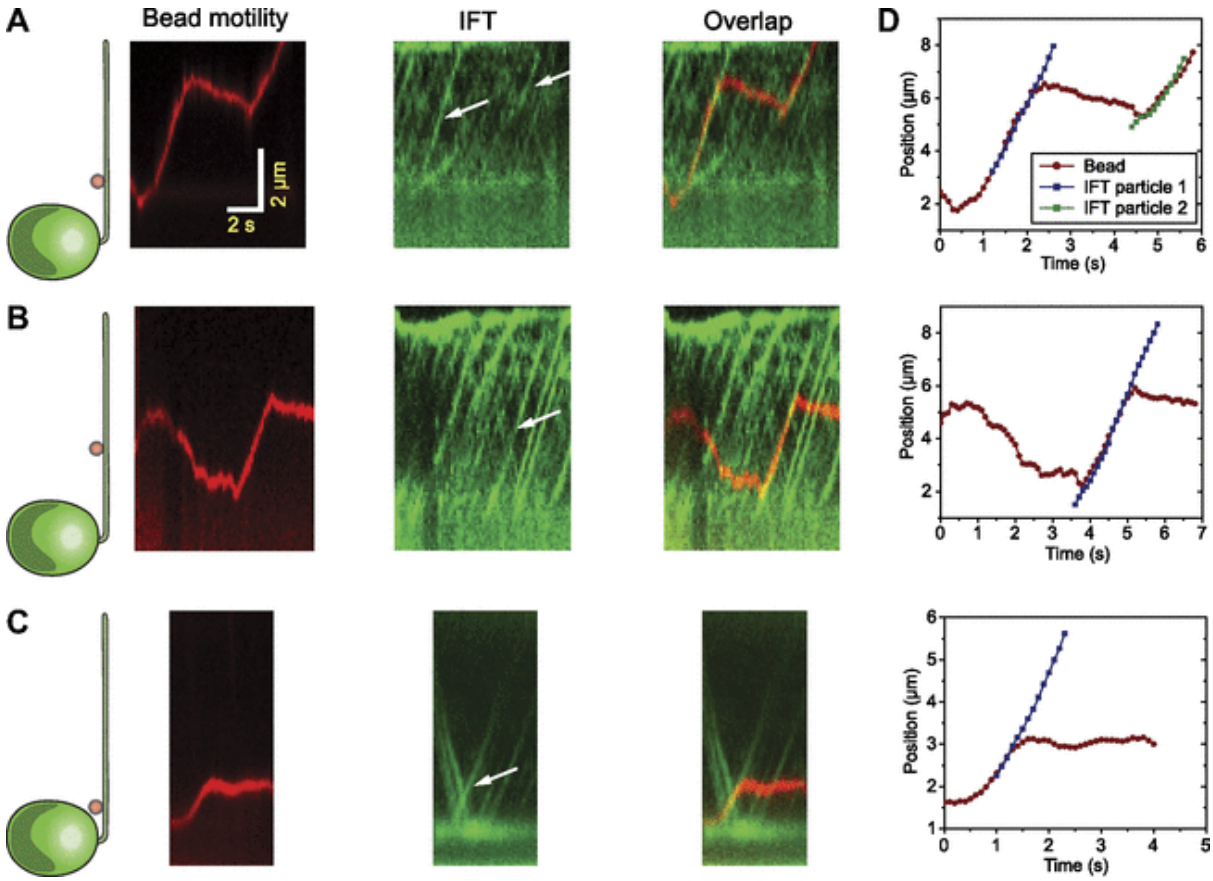


Figure 2.2 Additional examples of simultaneous tracking of bead motility and IFT.

(A–C) Three additional examples for colocalization and correlated movement of IFT trains (IFT27-GFP) and beads.

(D) Two-dimensional Gaussian fitting reveals the position of the bead and IFT individual trains as a function of time. Bead motility correlates strongly with the movement of individual IFT trains.

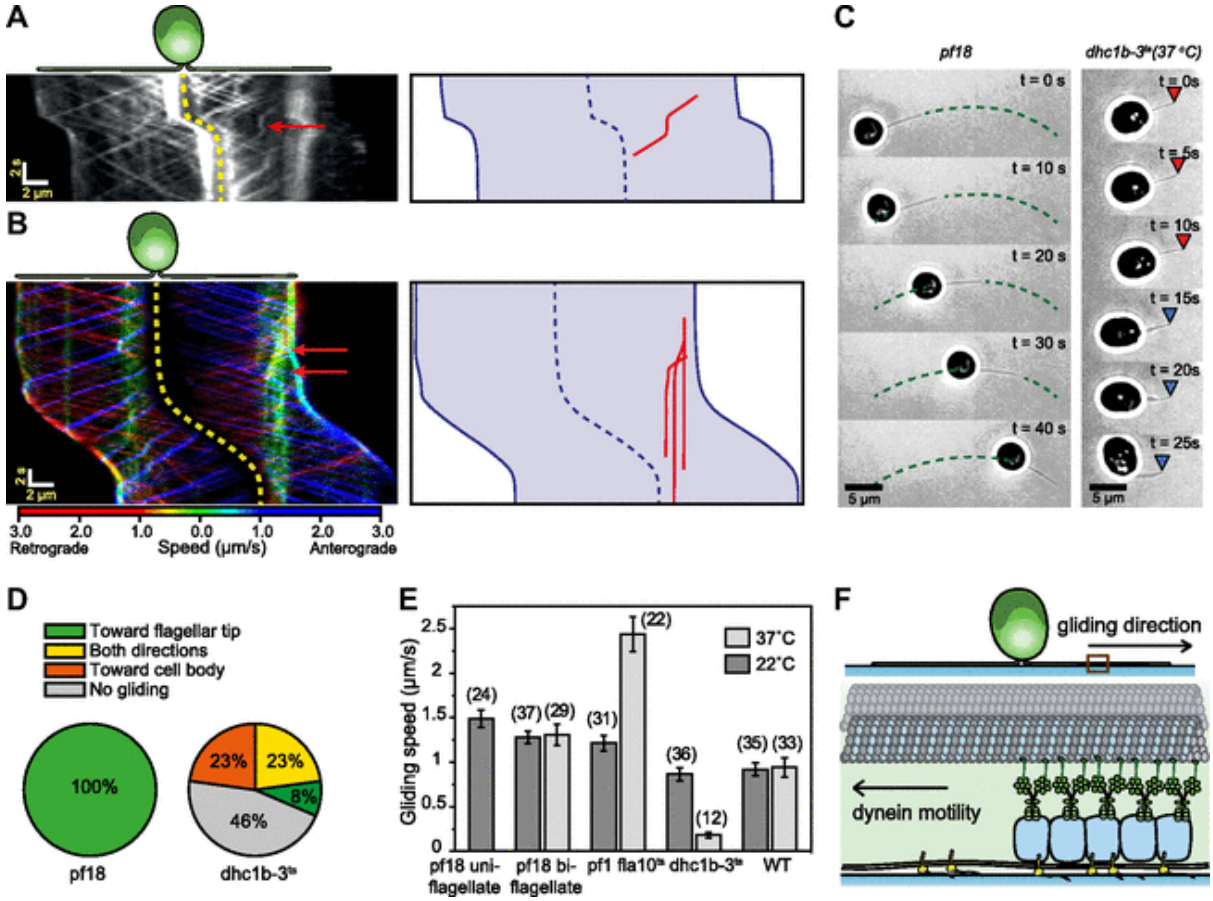


Figure 2.3 Dynein-1b drives gliding motility

(A) (Left) Kymograph of a gliding IFT20-GFP cell. A single retrograde IFT train transiently pauses (red arrow) and initiates the gliding movement of the cell toward the paused train. (Right) A schematic representing the timing and trajectory of the paused IFT train (red curve) in the gliding cell shown on the left.

(B) (Left) Kymograph of an IFT27-GFP cell, pseudo-colored to show the corresponding velocity of each IFT train. Multiple IFT trains (red arrows) pause (green color) prior to gliding motility. The cell glides until it reaches the paused IFT trains. (Right) A schematic representing the timing and trajectories of the paused IFT trains (red curves) in the gliding cell shown on the left.

(C) Gliding of uniflagellate cells under bright field illumination. A uniflagellate pf18 cell glides unidirectionally toward its flagellum. A uniflagellate *dhc1b-3^{t}* cell displays bidirectional gliding at the restrictive temperature. Red and blue arrowheads represent forward (flagellum in the lead) and backward (cell body in the lead) gliding directions.

(D) All of the uniflagellate pf18 cells glided with the flagellum in the lead. Heat inactivation of dynein-1b in *dhc1b-3^{ts}* cells at 37°C resulted in a 46% reduction in gliding frequency (N = 35) and led to bidirectional gliding motility. 8% of the cells glided with the flagellum leading the cell body (0.34 ± 0.09 µm/s, mean ± SEM), while 23% glided with the cell body leading the flagellum (0.47 ± 0.16 µm/s). 23% of the cells displayed saltatory gliding movement.

(E) Uniflagellate cells glided ~20% faster than biflagellate cells. Inhibition of dynein-1b (*dhc1b-3^{ts}*) resulted in a fivefold decrease in gliding speed, whereas inhibition of kinesin-2 (*pf1 fla10-1^{ts}*) led to a twofold speed increase (mean ± SEM). In temperature-insensitive paralyzed (pf18) and WT cells, changes in gliding speed between permissive and restrictive temperatures were negligible.

(F) A model for gliding motility. Retrograde IFT trains adhere to the glass surface through FMG1B, and the surface-tethered dynein motors pull the cell body through microtubules toward the flagellar tip.

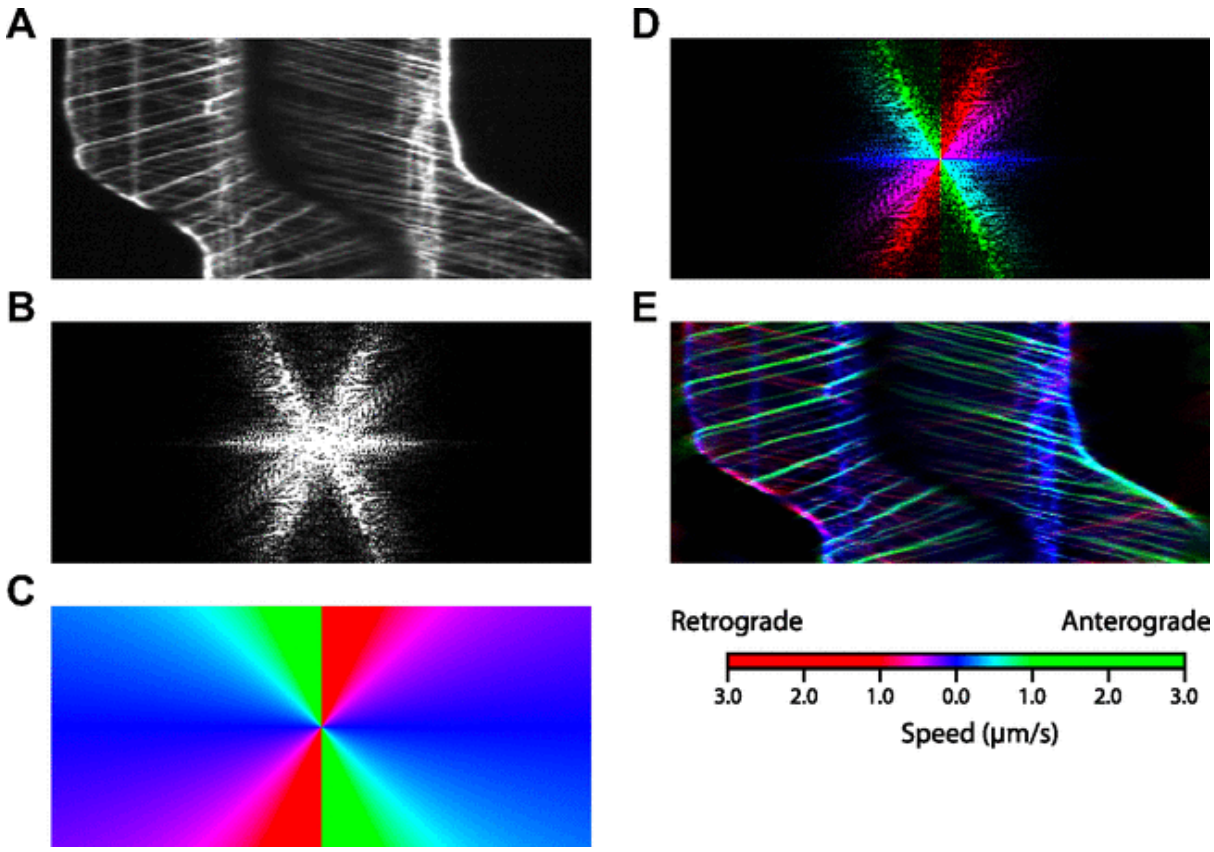


Figure 2.4 The procedure for Fourier space direction analysis

(A) The original kymograph of an IFT27-GFP cell during gliding motility.
(B) Magnitude of the fast Fourier transform of the kymograph.
(C) Mask with colors assigned to different slopes.
(D) The pattern in Fourier space was color-coded using the mask. Green and red colors represent anterograde and retrograde IFT, blue represents paused IFT trains. Only the magnitude is shown.
(E) Inverse Fourier transform of the colored Fourier pattern in (C) shows the kymograph with trajectories colored by slope.

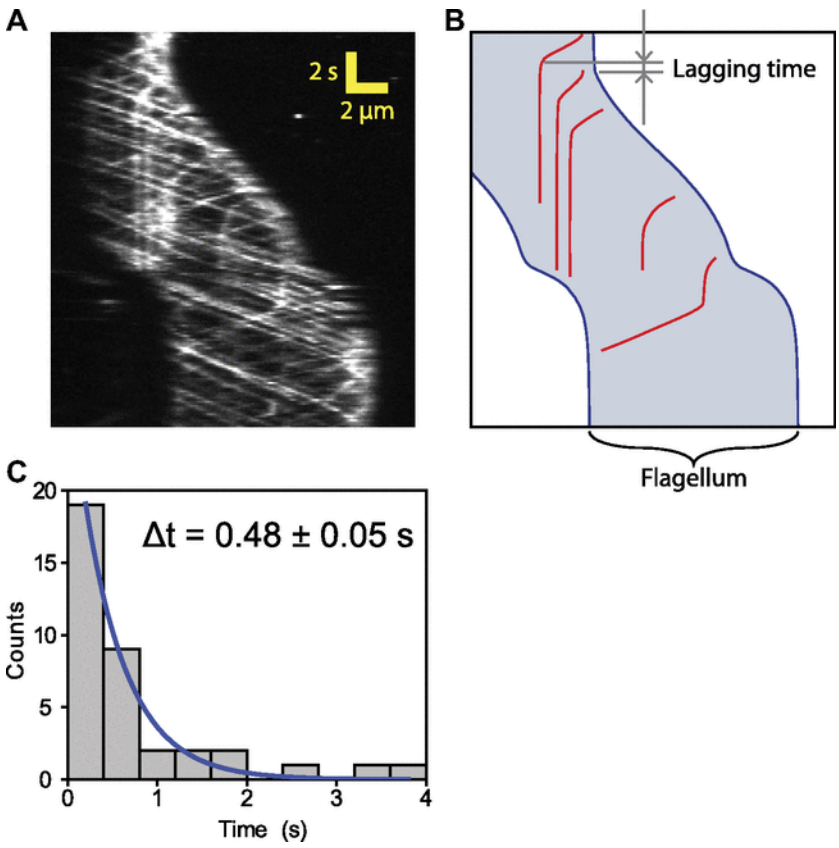


Figure 2.5 Lag time between IFT pausing and initiation of gliding motility

(A) A kymograph of IFT trains in a uniflagellate gliding cell.

(B) A schematic representing the timing and trajectories of paused IFT trains in the gliding cell shown in (A). Arrows show the time interval between the pausing of the retrograde IFT train and the start of gliding motility.

(C) The histogram shows the time between the start of gliding motility and the pausing time of the last retrograde IFT train in the leading flagellum. The histogram was fitted to a single exponential decay (blue curve). Average lag time is 0.48 ± 0.05 s (N = 36), which is significantly shorter than the average time between individual IFT pausing events (8 s).

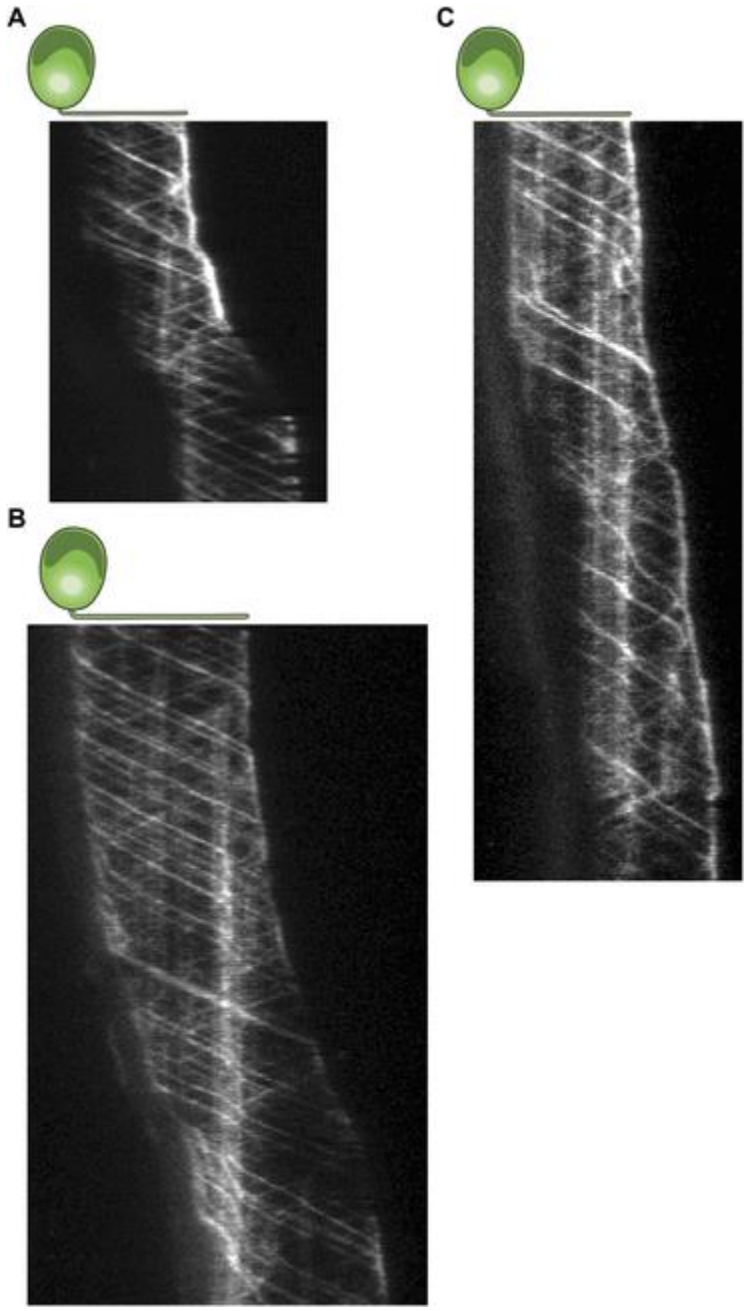


Figure 2.6 Kymograph of gliding uniflagellate IFT27-GFP cells
(A)–(C) Multiple retrograde IFT trains pause prior to gliding motility.

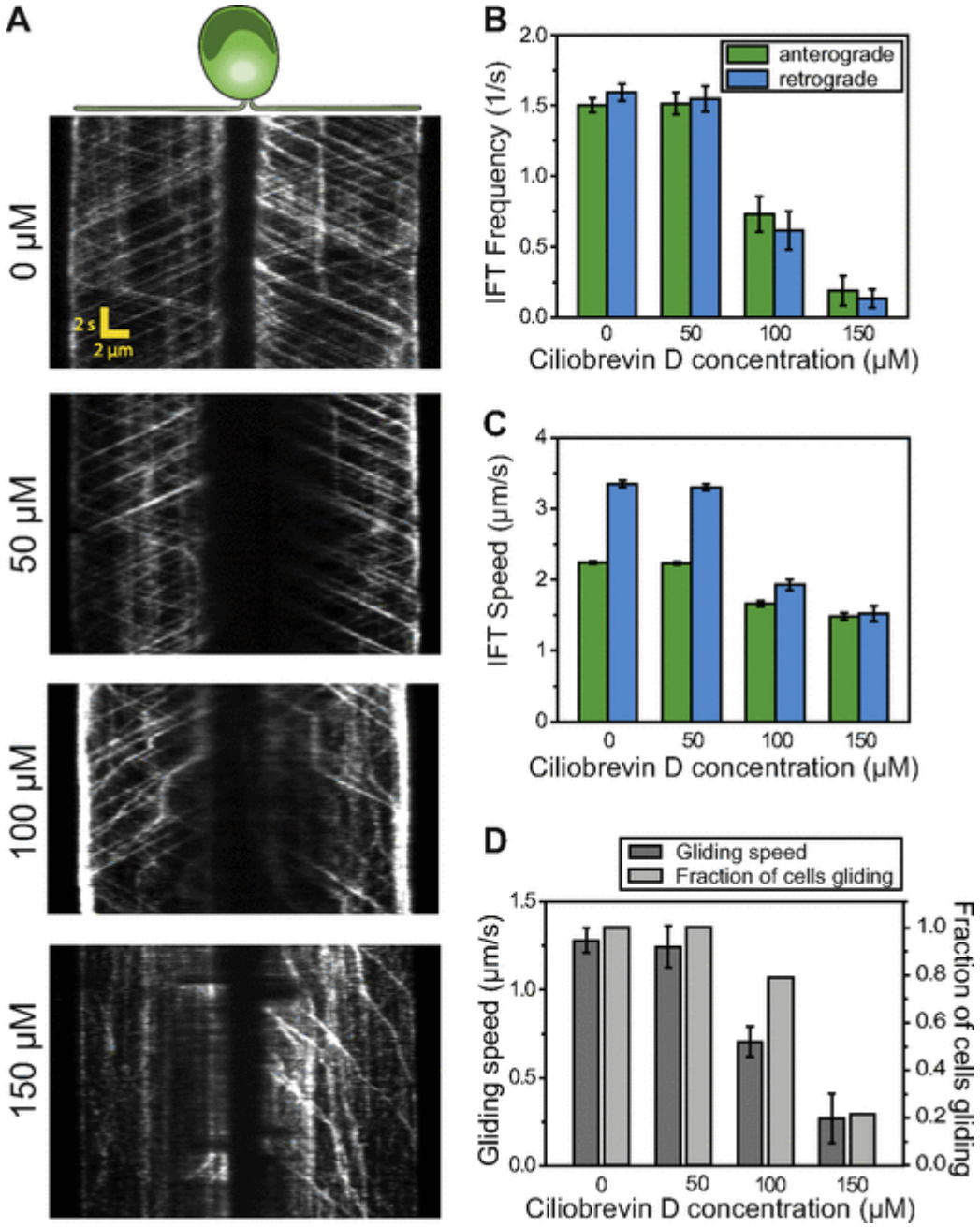


Figure 2.7 Ciliobrevin D inhibits dynein-1b and stops gliding motility

(A) Kymographs of IFT20-GFP cells treated with varying concentrations of ciliobrevin D. Images were acquired 5 min after addition of ciliobrevin D.

(B and C) Frequency and speed of retrograde and anterograde IFT trains at different ciliobrevin D concentrations. The frequency of retrograde IFT was reduced by 92% at 150 µM ciliobrevin D.

(D) The speed and fraction of gliding cells decreased by 79% at 150 µM ciliobrevin D.

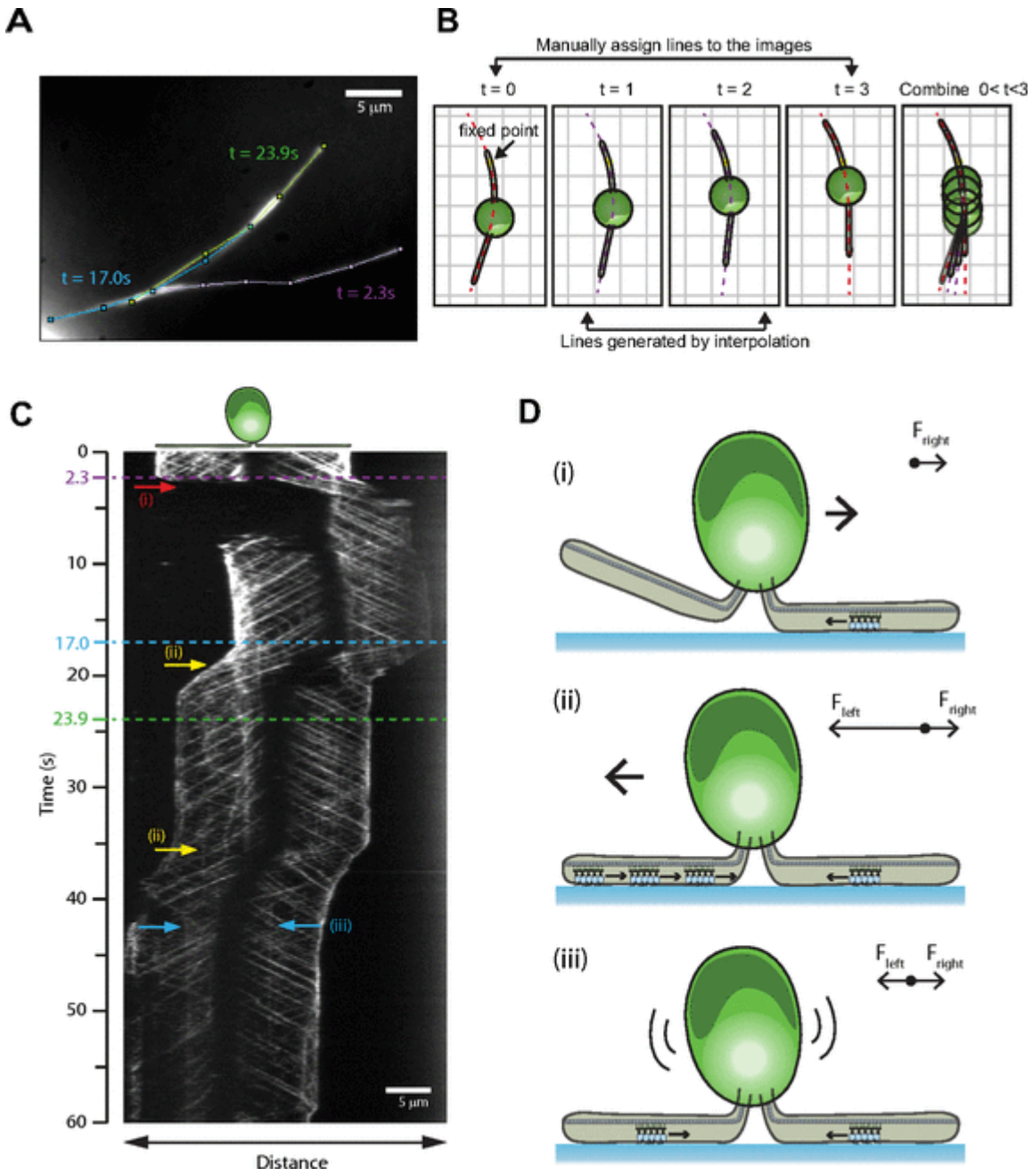


Figure 2.8 Mechanisms of reversal in gliding motility

(A) The average intensity of all the frames in a video of a gliding IFT27-GFP *pf18* cell, showing the path of the gliding flagella.

(B) To monitor IFT trains while the cells alter their flagellar orientation in gliding motility, different curves were plotted before and after cells reoriented their flagella (red dotted lines). Each curve shares at least one common point with previous and subsequent curves. Intermediary frames were analyzed by interpolation of the assigned curves, and the intensity along the line in each frame was stacked according to the fixed point (yellow dot).

(C) A kymograph generated by this method reveals multiple ways that the cell can control gliding direction. (i) When the cell lifts one flagellum (red arrow), the cell body moves toward the surface-attached flagellum. When both flagella are attached to the surface, gliding direction is determined by the balance of forces exerted by surface-tethered IFT trains. (ii) The cell glides toward the flagellum with more paused IFT particles (yellow arrow). (iii) When there are equal numbers of

surface-tethered IFT particles in both flagella (cyan arrow), opposite forces cancel out and the cell remains stationary.

(D) A schematic model representing the three different modes (i, ii, iii) of gliding direction reversal observed in (C).

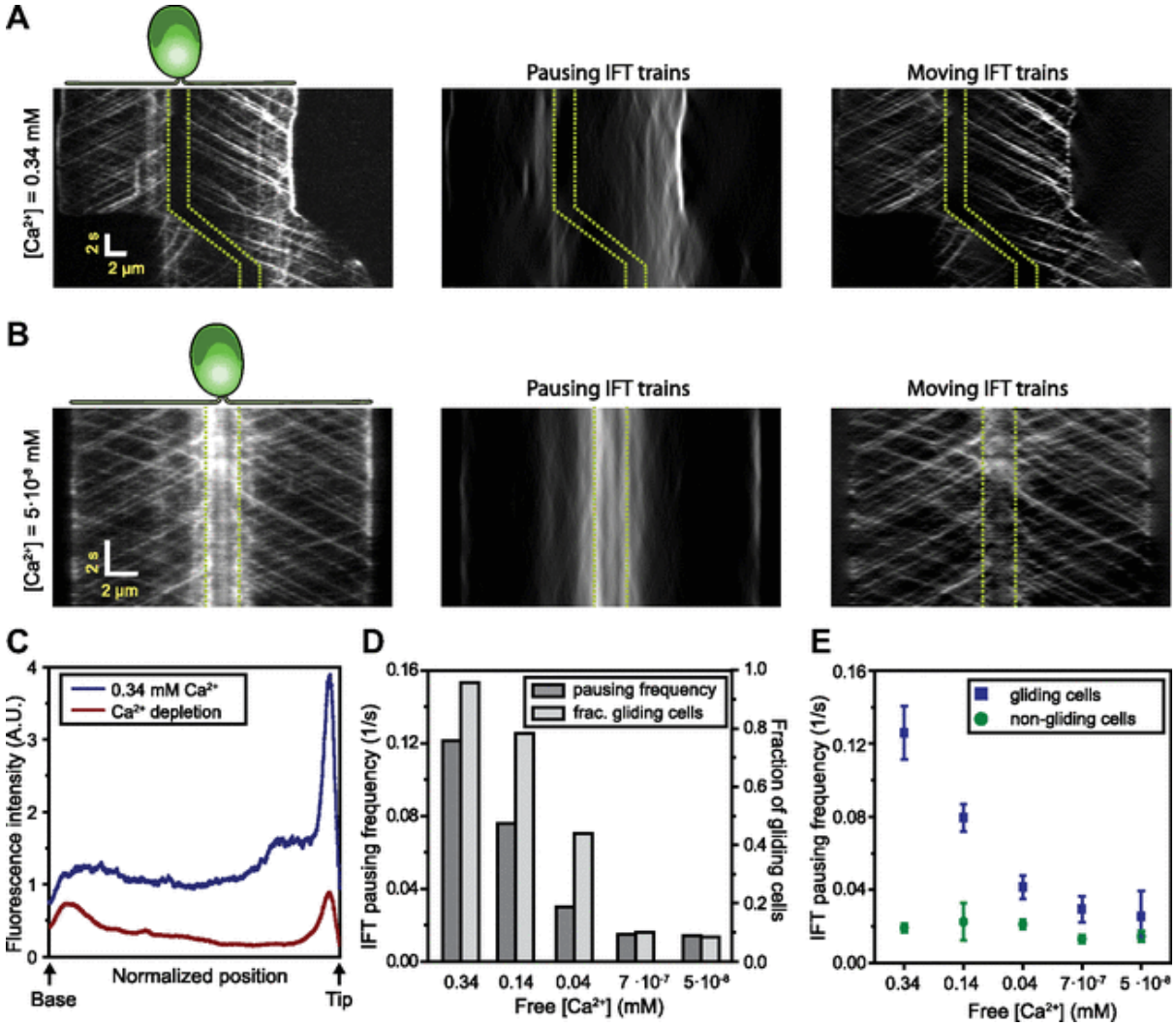


Figure 2.9 Ca^{2+} is required for the pausing of IFT trains at flagellar adhesion sites

(A) (Left) Kymograph of an IFT27-GFP cell adhering both of its flagella in the presence of 0.34 mM free Ca^{2+}. Pausing (middle) and moving (right) IFT trains were split into separate kymographs by FSDA analysis. IFT trains pause frequently along the length of the flagellum and drive gliding motility.

(B) When cells are deprived of free Ca^{2+}, immotile IFT trains accumulate near the cell body and do not display frequent pauses between the flagellar base and the tip.

(C) The average fluorescence intensity of 'pausing IFT trains' in kymographs relative to the length of the flagellum (N = 6 cells for each condition). Cells in 0.34 mM Ca^{2+} show robust pausing uniformly along the length of the flagellum. In contrast, Ca^{2+}-deprived cells show significantly reduced pausing events. Background fluorescence was excluded from the analysis.

(D) IFT pausing frequency and the fraction of gliding cells as a function of free Ca^{2+} concentration. The free Ca^{2+} concentration was controlled through Ca^{2+}-EGTA buffering.

(E) IFT pausing frequency of gliding and non-gliding cells as a function of free Ca^{2+}. At 0.34 mM Ca^{2+}, the IFT pausing frequency in gliding cells is very high compared to non-gliding cells. In Ca^{2+}-deprived cells, the pausing frequency in gliding cells is reduced to the residual level of pausing events observed in non-gliding cells.

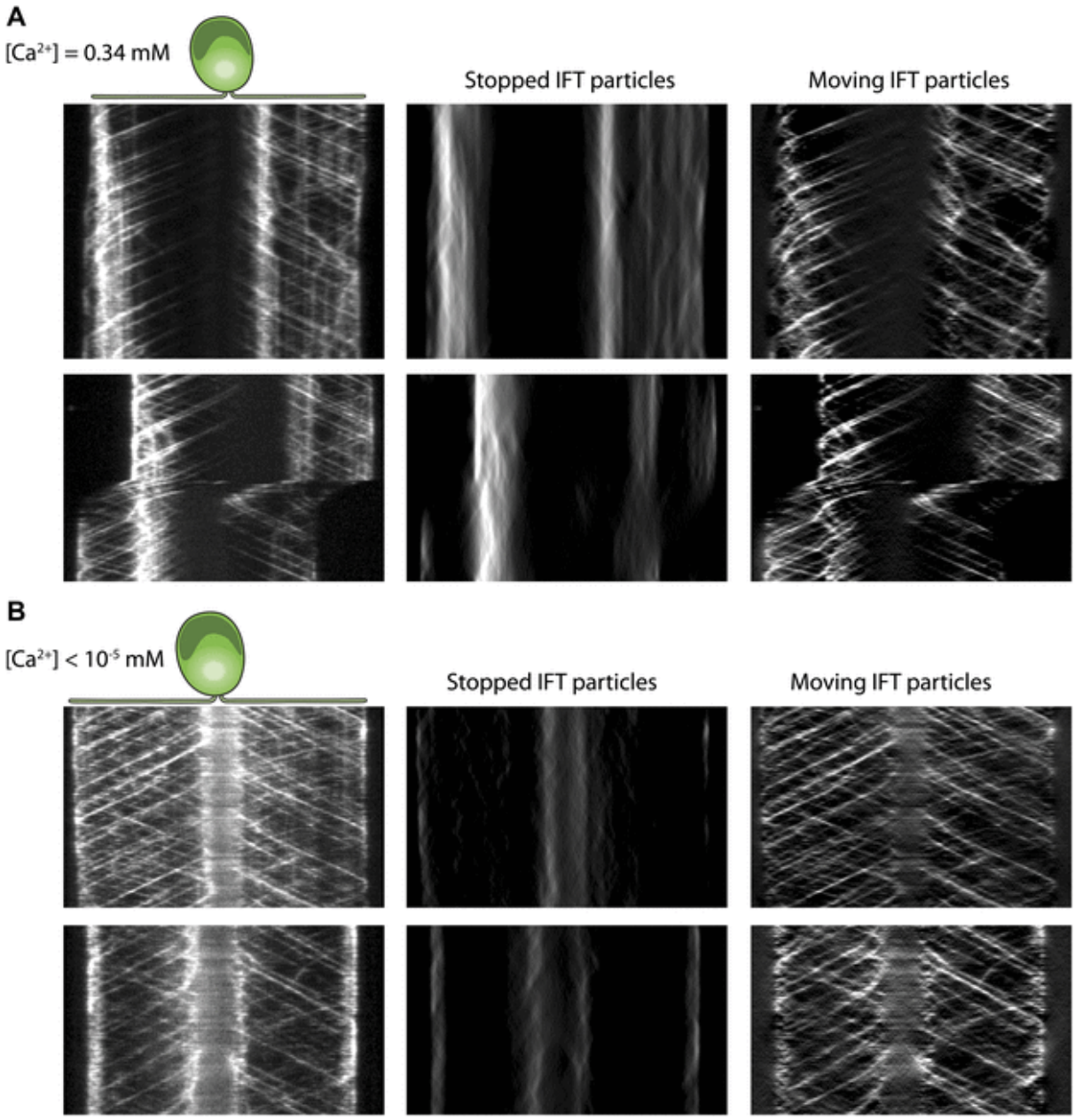


Figure 2.10 The analysis of IFT pausing in the presence and absence of free Ca^{2+} in media

(A) Two additional examples for kymographs of IFT27-GFP cells adhering both flagella to the surface in the presence of 0.34 mM free Ca^{2+}. Pausing (middle) and moving (right) IFT trains were split to separate kymographs by FSDA analysis. IFT trains pause frequently along the length of flagellum and drive gliding motility.

(B) Two additional examples for kymographs of IFT27-GFP cells adhering both flagella to the surface when cells are deprived of free Ca^{2+}. IFT trains accumulate near the cell body and do not display frequent pauses between the flagellar base and the tip.

Chapter 3. Coordination of Kinesin-2 and Dynein on IFT Trains

3.1 Introduction

Video microscopy of live *Chlamydomonas* cells revealed the intraflagellar transport (IFT) motility, in which heterogeneous arrays of multiprotein complexes (IFT trains) are moved between the flagellar membrane and the axoneme (Kozminski et al., 1993). Kinesin-2 carries IFT trains in continuous anterograde streams from cell body to flagellar tip along the unipolar microtubule array of the axoneme (Cole et al., 1998). IFT complexes are reorganized at the distal tip, then transported retrogradely to the flagellar base by cytoplasmic dynein-1b (Pazour et al., 1999; Porter et al., 1999). Electron micrographs indicate that multiple motors are cross-bridged between microtubules and IFT trains (Kozminski et al., 1993; Pigino et al., 2009). However, it remains unclear how many motors are actively engaged in the transport of a single IFT train, how opposite polarity motors interact with each other and how cargos reverse their direction at the flagellar tip and base (Laib et al., 2009). It is possible that regulatory complexes located at the base and tip of the flagellum enforce efficient transport of cargos by allowing only one type of motor to be active at a time (Vale, 2003). Alternatively, cargos may reverse their direction of motion through a tug-of-war mechanism (Hendricks et al., 2010).

Here we used combined fluorescence and optical trapping technique to show that we can measure the stall force of IFT trains by manipulating beads tethered to flagellar membrane proteins. We found out that at least four motors are active on single IFT trains. The stall force of kinesin-2 and dynein-1b *ts* mutants stays the same at the permissive and restrictive temperature, suggesting that kinesin-2 and dynein-1b are coordinated without completing with each other.

3.2 Methods

Strains and Culture Conditions

Wild-type mt+ (cc125), *pf18* mt- (cc1297), and *pf18* mt+ (cc1036) strains were obtained from the *Chlamydomonas* Resource Center (University of Minnesota, St. Paul, MN). The KAP-GFP *fla3* mt- strain (cc4296) was provided by M. Porter, and the IFT20-GFP ΔIFT20 strain was provided by K. Lechtreck and G. Witman. The IFT27-GFP mt+ strain and a paralyzed version of the *fla10* kinesin temperature-sensitive mutant strain (*pf1 fla10-1^{ts}*) were provided by J. Rosenbaum. KAP-GFP *fla3 pf18* and IFT27-GFP *pf18* strains were generated through crosses (Engel et al., 2009). The *ts* kinesin-2 mutant strain (*pf1 fla10-1^{ts}*) was incubated at 37 ˚C for 15 min for heat inactivation, and the data were collected within 30 min at 37 ˚C, before the complete inhibition of IFT and the start of flagellar resorption

(Kozminski et al., 1993). The *dhc1b*-3^{ts} mt- mutant strain (cc4422) was used to inhibit dynein-1b after incubating the cells at 37 ℃ for 6 hours. The detailed characterization of IFT in the *dhc1b*-3^{ts} strain is published elsewhere (Engel et al., 2012).

Single Molecule Fluorescence Imaging

An objective-type TIRF microscope was set up, using a Nikon TiE inverted microscope equipped with a perfect focusing unit, bright-field illumination and a 100X 1.49 NA PlanApo oil immersion objective (Nikon). A488 nm solid state laser (Coherent) was used for GFP excitation. The GFP signal was recorded by an Andor iXon 512X512 electron-multiplied charge-coupled device (EM-CCD) camera. 1.5x extra magnification was used to obtain the pixel size of 106 nm.

IFT27-GFP *pf18* and IFT20-GFP ΔIFT20 strains were used for tracking individual IFT trains and KAP-GFP *fla3* cells were used for tracking the KAP movement (Engel et al., 2009). 15 µl cells in 5-fold diluted TAP media were applied to cover glass and inverted onto slides. The GFP-tracking experiments were performed at a low laser excitation power (0.5 mW) to reduce the photobleaching rate of GFP. KAP-GFP photobleaching assays were performed with a 20-mW 5-µm diameter laser excitation in an epifluorescence mode for 200 ms. Cells were imaged simultaneously with a 0.5 mW 40 µm diameter laser beam in TIRF mode to monitor the recovery of the fluorescence signal. Surface gliding motility assays were performed on flow chambers without polylysine treatment, and the GFP signal was tracked as described above. *ts* mutants were assayed at permissive (22 ˚C) and restrictive (37 ˚C) conditions by controlling the temperature of the microscope objective with an objective heater (Bioptechs).

Optical Trapping Assays

Force measurements of IFT movement were carried out with a custom-built optical trap microscope (Gennerich et al., 2007). A 1064-nm laser (Coherent, Compass) was mounted on an inverted microscope equipped with a 100X 1.49 NA oil immersion objective (Carl Zeiss). The trapping beam was steered by a computer-controlled acousto-optic deflector (AA Electronics) at 20 kHz to capture a floating monodisperse microsphere in the object plane. Trap stiffness was calibrated for each microsphere from the amplitude of its thermal diffusion. The microspheres were trapped by a 400 mW 1064 nm laser beam to achieve an average spring constant of ~0.4 pN/nm. The microsphere displacement was detected by a quadrant photodiode (QPD) and recorded at 2 kHz. Forces between ±80 pN were measured within the linear range of the detector (200 nm).

Carboxylated latex microspheres (0.92 µm diameter, Invitrogen) were coated with the anti-carbohydrate mouse monoclonal antibody to FMG1B for flagellar membrane attachment. Cover glasses were pre-treated with 0.7 mg/ml polylysine for 5 minutes. 10 µL cell culture

was flowed into a flow chamber and incubated for 30 seconds to allow cells to attach to the cover glass. 10 µL solution including 0.2x TAP, 1mM $CaCl_2$, 0.3 mg/mL BSA, and 0.1 g/L microspheres was then flowed into the chamber to replace the buffer and wash out cells that were not adhered to the glass surface. Cells with surface-immobilized flagella were imaged under bright-field illumination. Trapped microspheres were positioned over surface immobilized flagella. The fraction of moving microspheres was measured by resting microspheres on the flagellar surface for 1 min. While 20% of the uncoated microspheres moved along the flagellar surface, antibody-coated microspheres moved at higher probabilities (~85% at 10 mg antibody per g of microspheres). Microspheres coated with 0.05 mg/ml antibody, which have a binding probability of 38%, were used as our standard in further measurements.

Trap-microsphere separations larger than 10 nm were considered motor-driven movements. Experiments were carried out with the trap position fixed. Stall forces were defined as the magnitude of the opposing force that reduces the mean velocity of the microsphere to 0 for more than 100 ms. Returning events with stalling periods shorter than 100 ms at peak forces were scored as releases. Movements of microspheres beyond the linear range of the detector were scored as escapes. Student's t-test was performed to verify the statistical difference between the stall force distributions of two populations.

The trapping assays at restrictive conditions were performed at 34˚C by heating the objective with an objective heater. The kinesin temperature-sensitive mutant cells (*pf1 fla10-1^{ts}*) were pre-incubated at 34˚C for 15 min and the objective temperature was stabilized before data collection. Data was collected between 15-30 minutes after the pre-incubation of the cells. Microsphere movement was not detectable in *pf1 fla10-1^{ts}* cells 30 min after switching to the restrictive temperature (data not shown). The dynein temperature-sensitive mutant cells (*dhc1b-3^{ts}*) were pre-incubated at 34˚C for 6 hours prior to data collection; a significant reduction in retrograde IFT frequency was observed after 6 hours.

To simultaneously track microsphere movement and individual IFT trains, IFT27-GFP cells were immobilized to the glass surface, as described above. The sample was excited with a 488 nm near-TIRF laser beam with a diameter of 10 µm, and imaged by a 512x512 Andor iXon EM-CCD camera. A 400mW 1064 nm laser was used for microsphere trapping, and a position sensitive detector (PSD) was located at the back focal plane to detect microsphere displacement. During data acquisition, bright-field illumination was turned on for ~1 s at every 1-2 min to monitor the microsphere position along the flagella and to synchronize the PSD signal and CCD image.

Data Analysis

The kymographs of GFP-tagged strains were made in ImageJ. FRAP analysis of KAP-GFP in *Chlamydomonas* flagella was performed by measuring the total intensity of the half of

the bleached area that was closer to the flagellar tip. Fluorescence traces of anterogradely moving kinesin-2 motors were manually excluded from the analysis. The fluorescence intensity of 13 different recovery traces were fitted to a one-dimensional diffusion equation under the constraint that all traces have the same halftime. The intensity of each trace was then normalized according to the initial and final intensity. The fluorescent background of IFT27-GFP and KAP-GFP was measured after the removal of anterograde and retrograde transport traces and normalized by the total intensity of the kymographs. The position on each flagellum is rescaled such that 0 represents the flagellar base and 1.0 represents the tip of the flagellum.

For the speed measurements of IFT trains and KAP, unidirectional movement of distance > 5 µm was scored as a single run. For gliding speed analysis, individual cells were monitored for 1 min under bright-field illumination and unidirectional runs longer than 1 µm were scored as gliding motility. The kymographs of IFT27-GFP and KAP-GFP were plotted in ImageJ. Speeds were measured from linear fits to the displacement traces observed in kymographs.

3.3 Results

To estimate the number of actively engaged motors on a cargo, the response of multiple motors to load has been studied *in vitro* (Vershinin et al., 2007) and *in vivo* (Shubeita et al., 2008). We tracked the movement of FMG1B-antibody coated bead motility using an optical trap to measure the forces exerted by motors bound to individual IFT trains. To rule out the possibility that loads exerted by the trap might disrupt the linkage between IFT and FMG1B, we performed TIRF imaging of IFT27-GFP and optical trapping of beads simultaneously (Figure 3.1A). We observed that IFT trains remained colocalized with trapped beads when subjected to external forces (Figure 3.1B; see Figure 3.2 for additional examples). The average offset between the positions of the trapped beads and colocalized IFT trains was 280 ± 10 nm (N = 11). This is due to the fact that the beads (920 nm diameter) and IFT trains (200 - 1,000 nm in length) (Pigino et al., 2009) are large objects relative to the resolution of conventional fluorescence imaging (~200 - 250 nm) and the forces that stretch the bead-FMG1B-IFT linkage displace the center of the bead from the IFT train (see the schematics in Figure 3.3). The data present direct evidence that IFT transports FMG1B and trap measurements correspond to forces generated by IFT motors. Since beads are outside the cell, but are physically linked to the action of IFT trains, the assay combines the advantages of precise in vitro trapping with the ability to manipulate IFT motility under load.

In a fixed trap assay, ~50% of processive bead movements terminated with a stall before returning to the trap center (Figure 3.1C, Figure 3.4). Histograms of peak forces (Figure 3.1D) show that anterograde and retrograde IFT trains moved against 21.4 ± 0.7 pN and 25.2 ± 1.3 pN (s.e.m.), respectively. We did not observe a significant difference between the force values of stall and release events. The data indicate that multiple motors attached to

an IFT train may not be able to reach their maximum stall force, defined as the stall force of a single motor multiplied by the number of bound motors (Shubeita et al., 2008). It is possible that motors do not equally share the load, and that the premature release of load-bearing motors ends a processive run. The measured forces in both directions only marginally change (<20%) under different bead antibody-coating conditions (Figure 3.5). This data argue against the possibility that antibody-coating of the beads leads to the crosslinking of more than one IFT trains, which would be expected to multiply the average peak force. 20% of retrograde runs escaped the trap by producing more than 80 pN of force, presumably via clustering of FMG1B (Bloodgood, 2009), while less than 1% escape events were observed in the anterograde direction.

Stall forces represent a lower boundary for estimates of motor copy number (Jamison et al., 2010). Assuming that IFT motors produce 6 -7 pN forces (Brunnbauer et al., 2010; Gennerich et al., 2007), we estimate that at least four motors transport IFT trains at a time, in agreement with previously reported values (Engel et al., 2009). It is possible that multiple motor engagements enhance the run length of individual IFT trains, allowing them to traverse the length of a flagellum. In addition, the fast transport of IFT trains in a viscous cellular environment and IFT's role in FSM may require forces larger than single motor stall forces.

We next investigated why the speed of gliding motility (1.49 ± 0.10 μm/s, SEM) is significantly slower than that of retrograde IFT (2.96 ± 0.14 μm/s), even though both processes are powered by dynein-1b motors actively transporting IFT trains. IFT trains that carry 1-μm beads moved ~30% slower than IFT trains that were not associated with the beads (two-tailed Student's t-test, $p = 2.1 \times 10^{-9}$ (anterograde) and 1.8×10^{-11} (retrograde), Figure 3.6A). We reasoned that the viscous drag of the membrane may slow down IFT trains transporting FMG1B clusters and led to the observed differences in speed between IFT and FSM. To estimate the drag constant of the bead-IFT complex, we analyzed individual stalling events in the optical trap assay (Figure 3.6B) and measured the recoil time of the bead after a stall (Figure 3.6C). The average drag constant of the bead-IFT complex was found to be 8.0 ± 2.8 pN s/μm (SEM, N = 30).

We hypothesized that the large drag constants we measured were due to the interaction between the bead and the membrane. Our results rule out the possibility that microtubule motors step backwards during the recoiling of the bead, as the average bead velocity was 20 μm/s (an order of magnitude faster than that of dynein and kinesin) and there were no detectable backward steps. To rule out other possible interactions between IFT trains and axonemes, we oscillated individual beads on a flagellar membrane surface in a square wave pattern and measured the recoiling time when the beads are decoupled from IFT (Figure 3.7). The average viscous drag constant was 8.4 ± 4.2 pN s/μm, which is similar to the drag that beads experience when they interact with IFT trains. Anterograde and retrograde trains moving at 2–3 μm/s would experience 16–24 pN resistive forces, comparable to the total

motor force exerted on a single IFT train (Figure 3.6D). Therefore, IFT is subjected to a high drag force when it carries a large bead along the flagellar surface, which leads to the reduction of transport velocity.

We next investigated how kinesin-2 activity reduces the speed of gliding motility (Figure 2.3E). This could theoretically be explained by a tug-of-war between active kinesin and dynein motors that are both present on the same IFT train. Alternatively, kinesin-2 and dynein-1b motors may be exclusively active on anterograde and retrograde cargos, respectively, and pausing of anterograde trains could produce forces that oppose the gliding forces of paused retrograde trains. To distinguish between tug-of-war and coordinated transport mechanisms, we examined how inhibition of one class of motors affected the forces exerted on IFT trains traveling in the opposite direction (Laib et al., 2009). At permissive temperatures, the peak forces of IFT in *fla10-1*^{ts} and *dhc1b-3*^{ts} were in close agreement with wild-type (WT) cells. Heat-inactivation of kinesin-2 reduced the frequency of anterograde runs by 66%, but did not alter the peak forces on retrograde runs (Laib et al., 2009) (Figure 3.8A). Similarly, heat inactivation of dynein-1b significantly reduced the ratio of retrograde to anterograde transport events (0.15), but had minimal effect on the peak forces of anterograde runs (Figure 3.8B). These results exclude a tug-of-war mechanism in IFT, which would lead to an increase of force from motors walking in one direction upon inactivation of the motors walking in the opposite direction. Instead, only one type of a motor remains active on IFT trains at a time, which is consistent with the result that retrograde speed of *fla10-1*^{ts} does not change after kinesin-2 is inactivated. We propose that kinesin-2 on paused anterograde trains slows down gliding motility by exerting forces in the opposite direction to that of dynein-1b on paused retrograde trains.

3.4 Discussion

We provide evidence that the activities of kinesin-2 and dynein-1b motors avoid tug-of-war. First, KAP and IFT27 only reverse direction at either end of the flagellum. Second, stepping analysis of microsphere movement revealed that cargo transport is not interrupted with frequent pauses and rarely takes backward steps. Third, reversal of the direction of processive runs during peak force measurements is uncommon, indicating that only one class of motor is active at a time. Fourth, inhibition of kinesin or dynein in *ts* mutants does not alter forces generated on IFT trains being carried by the opposite-polarity motor (Laib et al., 2009).

In vitro motility experiments show that multiple motors produce larger forces, move with higher velocities under load and carry cargos further than a single kinesin or dynein motor (Mallik et al., 2005; Vershinin et al., 2007). It remains controversial whether motor stall forces are additive at low motor copy numbers (Vershinin et al., 2007) or whether multiple motors tend to transport their cargo using only one load-bearing motor at a time (Jamison et al., 2010). Our data show that the average forces exerted on IFT trains well

exceed the force-generation capability of a single motor. Since we did not observe a significant difference between the force values of stall and release events, multiple motors attached to an IFT train may not be able to reach their maximum stall force, defined as the stall force of a single motor multiplied by the number of bound motors. It is possible that motors do not equally share the load, and that the premature release of load-bearing motors ends the processive run. Therefore, the measured peak forces represent a lower boundary for estimates of motor copy number. Assuming that *Chlamydomonas* IFT motors produce similar forces (~6 pN) to *C.elegans* kinesin-2 (Brunnbauer et al., 2010) and *S. cerevisiae* dynein-1a (Gennerich et al., 2007), we estimate that at least four motors act on an IFT cargo at a time. These motor numbers are in agreement with photobleaching studies of KAP-GFP (Engel et al., 2009).

Our force measurements show a number of similarities and differences with earlier published work. In a previous trapping assay, beads nonspecifically adsorbed to the flagellar membrane were found to exert 60 pN average peak forces (Laib et al., 2009). In contrast, our measured peaked forces are significantly lower (20 – 30 pN) than these values. Laib et al. could not determine whether the force measurements reflect the forces produced by the motors attached to IFT trains or by motors that are directly linked to FMG1 clusters. Our experiments directly link optical trap recordings of bead motility to forces generated by flagellar motors attached to IFT trains (Figure 3.1), enabling us to propose physical models for the coordination of IFT and its role in flagellar surface motility. In agreement with Laib et al., we observe reciprocal coordination of motors during anterograde transport. Additionally, our measurements of dynein-1b inactivation verify that motors do not engage in a tug-of-war while travelling in the retrograde direction.

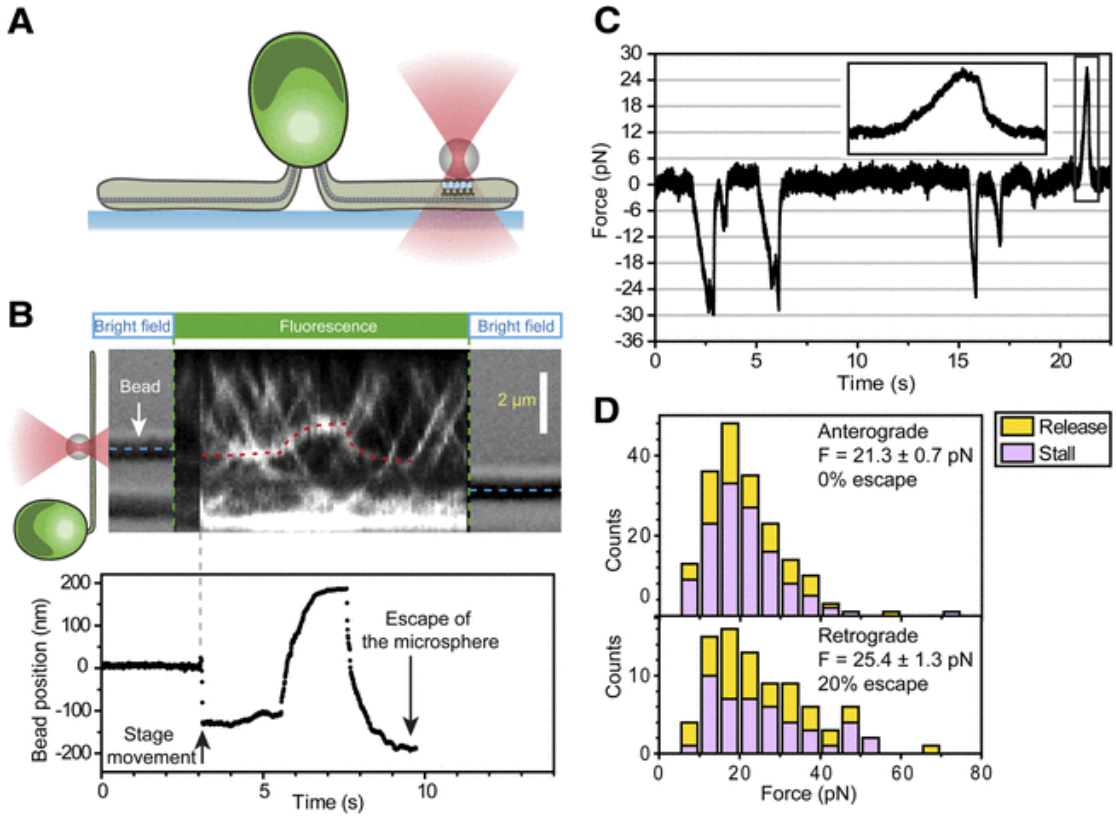


Figure 3.1 Stall force measurements on single IFT trains

(A) Schematic representation of combined optical trapping of bead motility and fluorescent tracking of IFT.

(B) Simultaneous tracking of IFT27-GFP and bead motility. At t = 3 s, the microscope stage was moved to bring the flagellum underneath the trapped bead. An IFT train stalls at the trap position (t = 5–8 s) and stays adhered to the bead until the bead escapes the trap (t = 10 s). The CCD camera is toggled between fluorescence and bright field imaging to monitor IFT trains as well as the bead when it is out of the detection range.

(C) Displacement records of bead motility show successive runs including stalling (inset) and releasing events.

(D) The peak force distributions and statistics (mean ± SEM) of stalling and releasing events in pf18 cells. IFT particles exert 25–30 pN of peak forces with slightly less force produced in the anterograde direction.

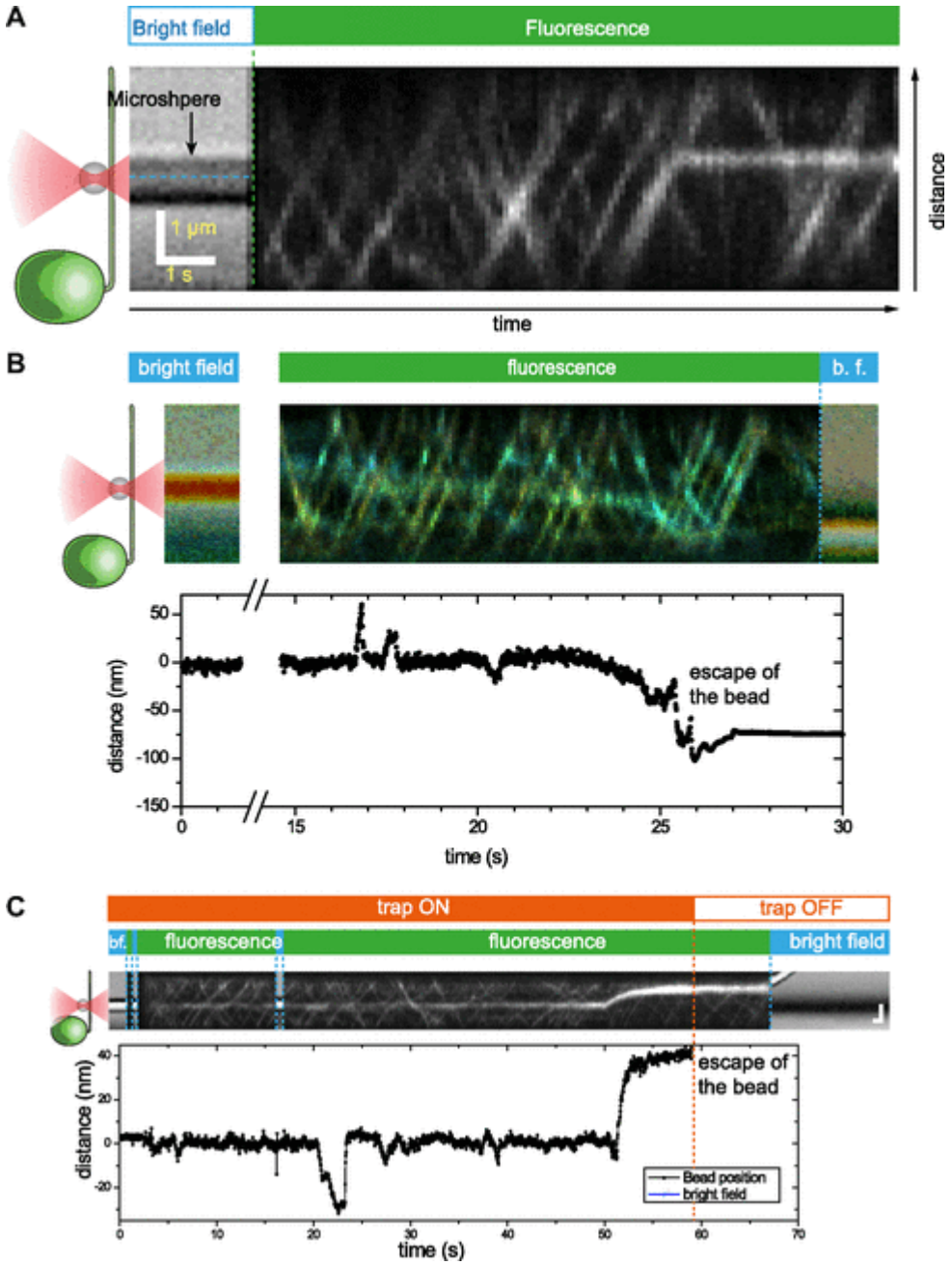


Figure 3.2 Three additional examples of simultaneous bead trapping and IFT27-GFP fluorescence tracking

(A) A single anterograde IFT train stalls directly underneath the trapped bead for 20 s.
(B and C) The bead shows multiple runs and escapes the trap. The optical trapping beam was on throughout the duration of the kymograph.

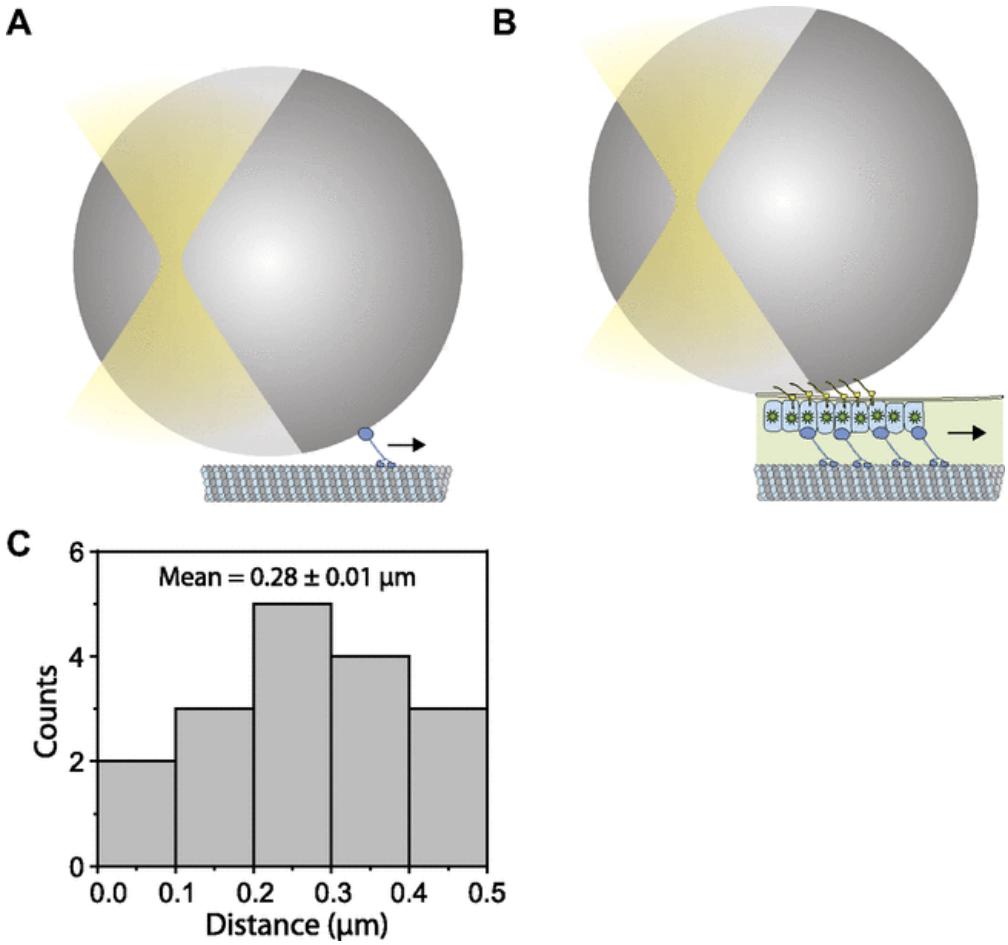


Figure 3.3 The offset between the bead position and IFT trains

(A) Schematic for an in vitro fixed-trap assay with a single motor bound to a microtubule.

(B) Schematic for the optical trap assay of *Chlamydomonas* bead motility (roughly to scale). In both (A and B), there is a large offset between the bead center and the motor/cargo. The size of the offset depends on tether length, the bead diameter and the length of IFT train.

(C) Histogram for the separation between the bead center and IFT position in the combined optical trap and fluorescence experiment. We observe up to 500 nm offset between an IFT train (~400 nm in length) and the polystyrene bead (900 nm in diameter). The average separation between the bead and IFT is 280 nm.

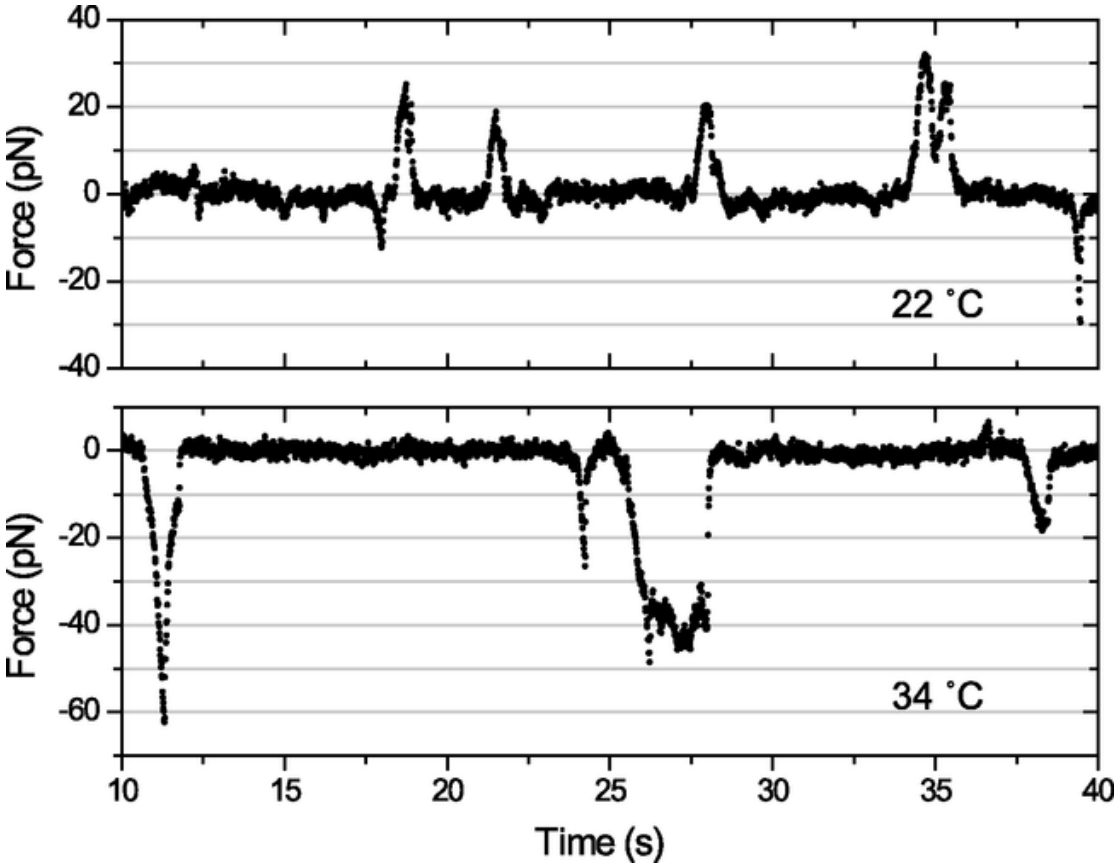


Figure 3.4 Additional examples for bead motility under fixed trap

(Top) Displacement records of bead motility in *fla10*^{ts} cells show successive runs, stalling and releasing events along the anterograde direction at permissive temperatures. (Bottom) The bead motility in *fla10*^{ts} cells displays runs, stalling and releasing events mostly along the retrograde direction at restrictive temperatures.

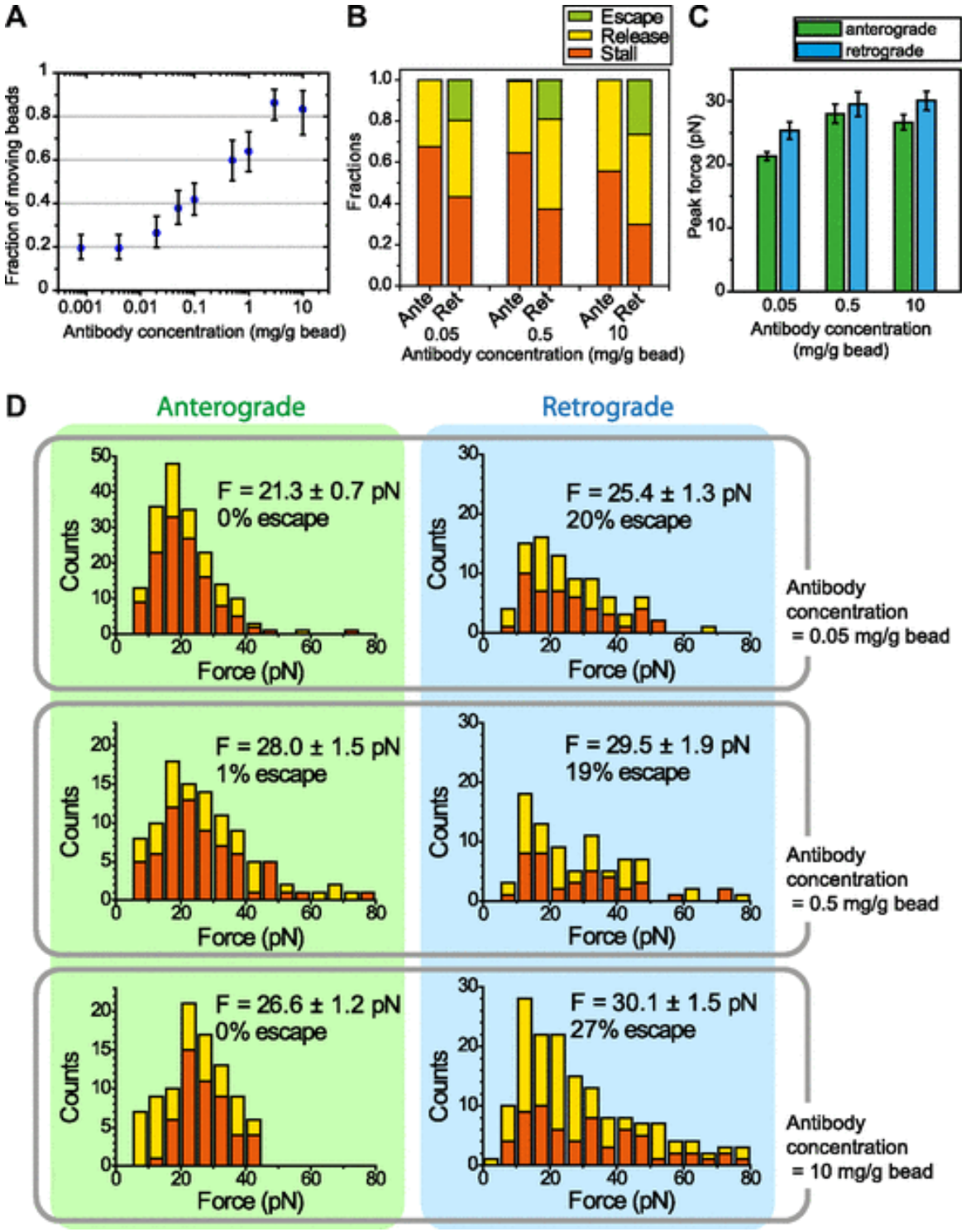


Figure 3.5 The effect of antibody concentration on peak forces measurements

(A) The fraction of beads moving along the flagellar surface as a function of the antibody concentration on the bead surface.

(B) The fraction of stall, release and escape events along the anterograde and retrograde directions in optical trapping assays as a function of antibody concentration used to coat the bead surface.

(C) Histograms of peak forces measured in the optical trap assay along the anterograde and retrograde directions in WT cells. 1 µm diameter polystyrene beads were coated with 0.05, 0.5 and 10 mg/ml FMG1B antibody.

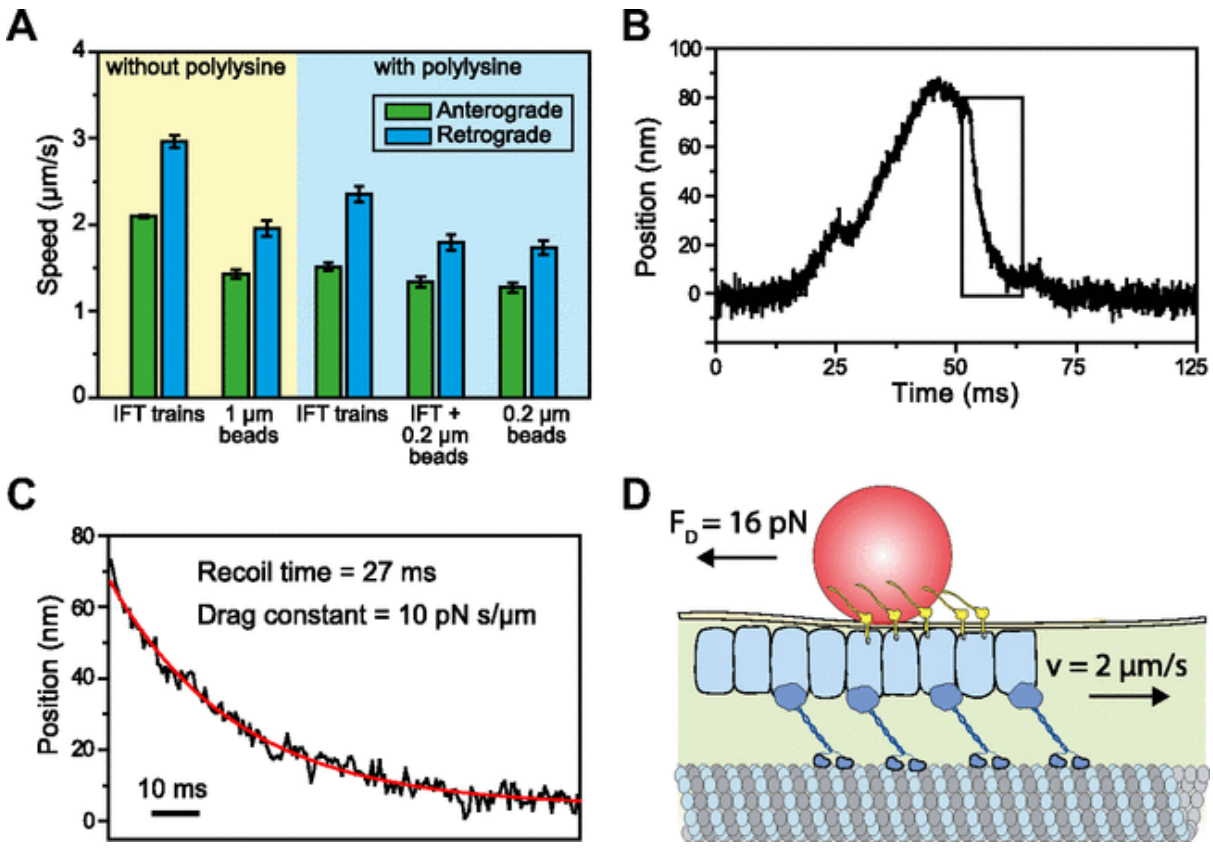


Figure 3.6 Viscous drag of the membrane slows down the motility of IFT trains that carry beads

(A) The average speed of FMG1B antibody-coated beads and IFT trains. Coating of the coverslip surface with 0.7 mg/ml polylysine led to a ~20% reduction in the speed of IFT motility (two tailed t-test, $p=5.2 \times 10^{-14}$ [anterograde] and 5.6×10^{-6} [retrograde]). IFT trains that carry 0.2-µm beads move at 10–30% slower speeds than IFT trains that are not associated with the beads ($p=1.1 \times 10^{-2}$ [anterograde] and 7.2×10^{-5} [retrograde]). IFT trains that carry 0.2-µm beads move at similar speeds to beads (p=0.4 [anterograde] and 0.6 [retrograde]) (error bars represent SEM).

(B) A typical example for stalling of bead motility by the optical trap. The bead recovers slowly to the trap center after a stall (rectangular box).

(C) The recoiling of a trapped bead to the trap center after a stall was fitted to single exponential decay. The mean drag constant of the bead-FMG1B-IFT complex is 8.0 ± 0.28 pN s/µm.

(D) The IFT-bead complex experiences large drag forces as the IFT train moves several micrometers per second inside the flagellum (not to scale).

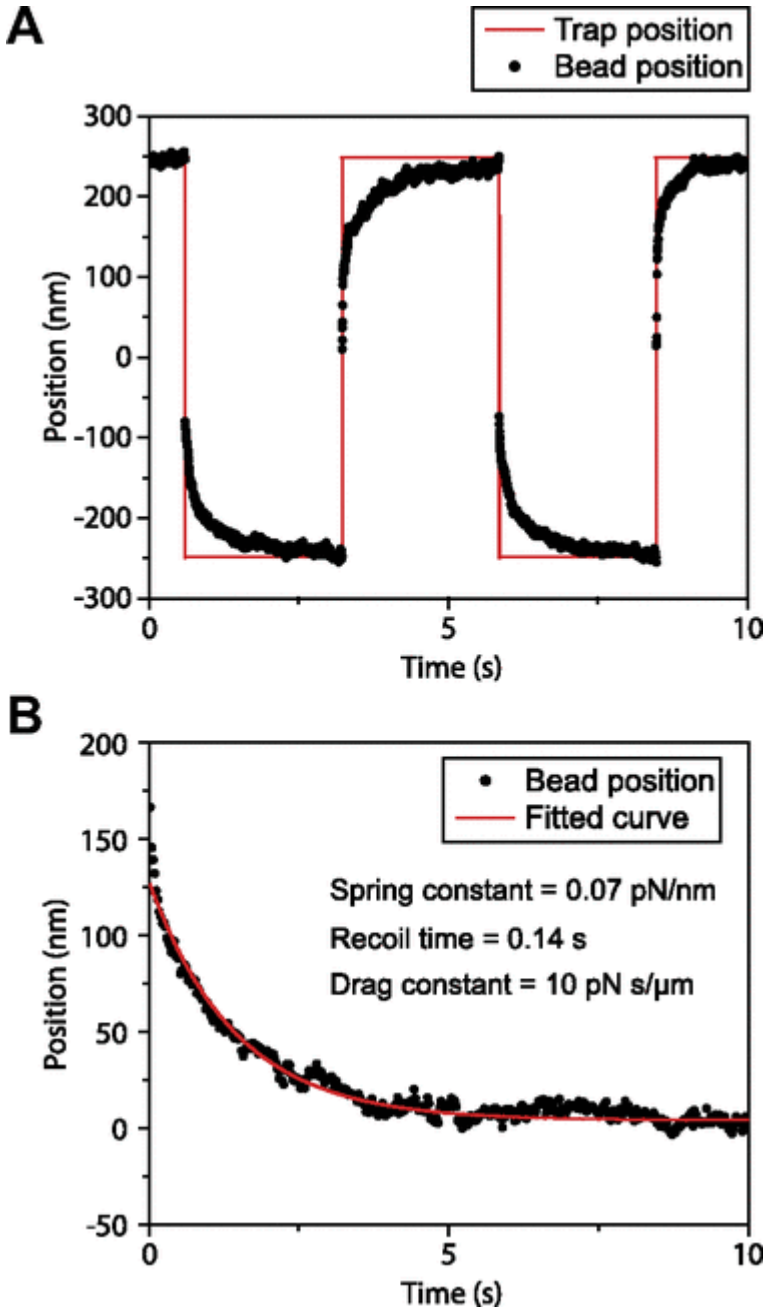


Figure 3.7 Measurement of viscous drag on bead movement along the surface of the flagellar membrane

(A) A polystyrene bead was trapped by the laser beam and brought on top of a surface-immobilized flagellum. After the bead was bound to FMG1B, the trap was oscillated 500 nm back and forth along the flagellar surface in a square wave pattern. Trap stiffness was set to 0.07 pN/nm. Due to the viscous drag of the membrane, the bead displays a relaxation curve when it follows the trap.

(B) The recoiling of a trapped bead to the trap center after a stall was fitted to single exponential decay. The mean drag constant of the bead-FMG1B-IFT complex is 8.4 ± 4.2 pN.s/µm.

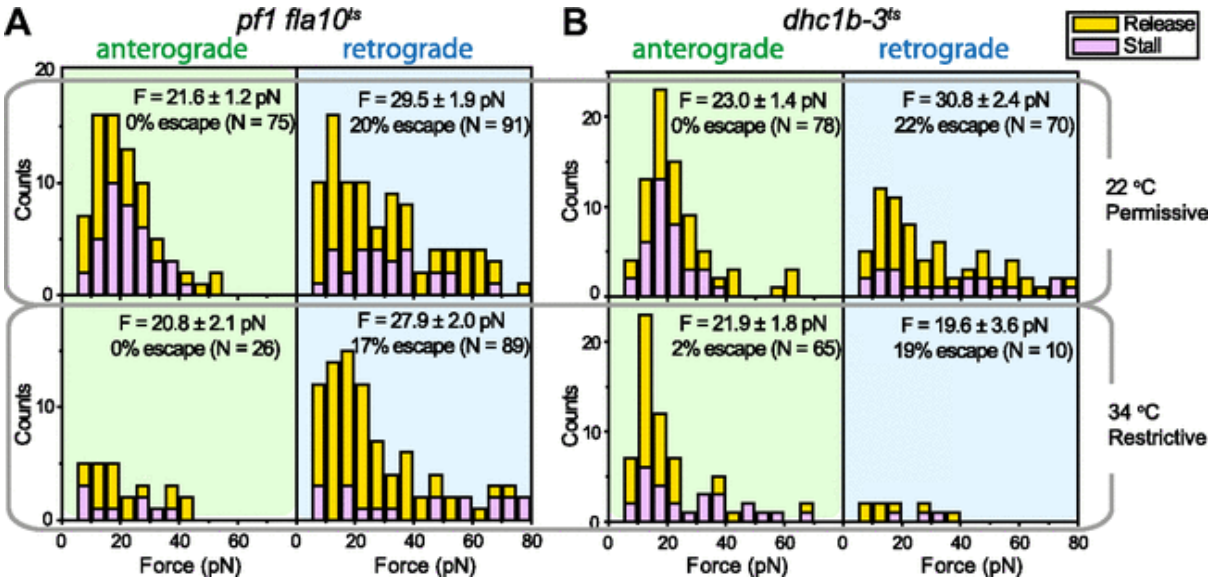


Figure 3.8 Force measurements on temperature-sensitive mutants

(A) Peak force histograms for IFT movement in *pf1 fla10-1*^{ts} cells at 22℃ and 34℃. Stalling events are less common than the release of the bead. The frequency of anterograde IFT trains is reduced after switching the temperature to 34℃. Forces along the retrograde direction remain unaltered after the inhibition of kinesin-2 (mean ± SEM).

(B) Peak force histograms for IFT in *dhc1b-3*^{ts}. The frequency and force production of retrograde IFT trains are reduced after switching the temperature to 34℃. Forces along the anterograde direction remain unaltered after the inhibition of dynein-1b (mean ± SEM).

Chapter 4. Photobleaching Gate Assay

4.1 Introduction

Tracking the dynamics of individual molecules and complexes in living cells has been a challenging task because of the complexity of cellular environments, the rapidness of molecular dynamics, and the lack of microscopic tools. In conventional light microscopy, fluorescents objects are limited by diffraction of their emitted light. The width of a diffraction limited spot is ~250 nm in the visible region of light, and molecules closer to each other than this limit cannot be readily separated from each other due to the overlap of their images. In vitro, the density of fluorescent particles can be reduced to separate individual molecules from each other. Distinct fluorescent spots can be tracked over a long period at nanometer precision by determining the center of their point spread functions (PSFs) (Yildiz et al., 2003). However, the concentration of targeted molecules is naturally dense, so individual molecules cannot be easily detected in vivo. Several methods can achieve sub-diffraction limited resolution, but they sacrifice temporal resolution (Rust et al., 2006; Betzig et al., 2006; Kner et al., 2009; Klar et al., 2000), hence unsuitable for monitoring rapid dynamic processes. Alternatively, single-molecules can be detected in dense specimens by photoactivation methods (Kuzmenko et al., 2011). However, photoactivable probes often emit less photon than most organic dyes and fluorescent proteins. Therefore, they photobleach quickly and are easily overshadowed by the autofluorescence of the cell.

Photobleaching methods are also commonly used to determine the dynamics of molecules inside the cells. In a fluorescence recovery after photobleaching (FRAP) assay (Reit et al., 2001), high-power laser beam is used to photobleach fluorescent molecules in a part of the cell. The partial recovery of the fluorescence signal is detected to determine the average diffusion constant and the percentage of mobile molecules inside cells. The recovery of fluorescent particles usually comes in continuous stream, so this method is often not suitable for single-molecule detection.

To track single molecules in dense specimens, we developed the photobleaching gate assay that selectively photobleaches fluorescent particles and only allows single (or a few) fluorophores to remain fluorescent in the region of interest (ROI). The selected fluorophores were tracked at high spatial precision for long periods of time until they photobleach under a wide-field illumination. Other surrounding fluorophores entering the ROI are photobleached by the second beam, which serves as a gate to isolate the ROI from the rest of the environment. The method tracks single molecules in dense fluorescent specimens at high spatiotemporal resolution and does not require photoswitchable probes.

Our method is broadly applicable to dynamic cellular processes including cargo transport, diffusion, assembly and disassembly, and other interactions between proteins and nucleic acids. In this study, we used a ring-shaped laser beam as the gate to track individual

EGFR molecules on the cell membrane of COS7 cells and observed the dimerization of EGFR upon addition of a growth factor.

4.2 Methods

Sample Preparation

DNA encoding the full-length human EGFR gene with a C-terminal $eGFP^{A206K}$ fusion in pEGFP-N1 (Clontech) mammalian expression vector was stably transfected into COS-7 cells. Briefly, COS-7 cells were transiently transfected using FuGENE (Roche) according to the manufacturer's instructions. Stable clones were isolated by selection in 800 μg/ml G418 for 4 weeks. Stable COS-7 cell lines were maintained in Dulbecco's Modified Eagle's Medium supplemented with 10% fetal bovine serum (FBS), streptomycin/penicillin and 200 μg/ml G418. 48 hours prior to use, cells were split into glass bottom petri dishes (Matek) with Phenol-red free DMEM. 12 hours before the experiment, cells were serum starved by replacing the medium with FBS-free medium. When noted, cells were treated with or without 16 nM EGF for 5 mins, before measurements were performed. The microscopy assays were performed at 37 ℃ under CO_2.

Microscope

An objective-type TIRF microscope was set up, using a Nikon TiE inverted microscope equipped with a perfect focusing unit, bright-field illumination and a 100X 1.49 NA PlanApo oil immersion objective (Nikon). A 488 nm solid state laser (Coherent) was used for GFP excitation. The GFP signal was recorded by an Andor iXon 512 x 512 electron-multiplied charge-coupled device (EM-CCD) camera. 1.5x extra magnification was used to obtain a pixel size of 106 nm. Data was collected at 10 Hz time resolution. Excitation of the laser beams were controlled by Uniblitz shutters. Because CCD image is saturated under intense laser illumination, shutter timing was synchronized with the camera acquisition by a data acquisition card (NI, USB-6221) to minimize the number of "dead" frames in recorded movies.

The Photobleaching Gate Assays

To effectively bleach fluorescent particles entering to the ROI, the periphery of the ROI was excited with a high-power (52 kW/cm^2) ring-shaped photobleaching beam was used in epifluorescence mode. The ring-shaped beam was generated by a pair of plano-convex axicons with a characteristic angle of 170° (Edmund Optics), with an iris placed immediately before the first axicon for cleaning up the edge of the beam. To collimate the ring-shape beam, the iris and the first axicon were placed at the conjugate plane of the image plane. The resulting beam has a 14-μm inner diameter and a 4-μm thickness. The beam profile was tested by exciting a coverslip densely coated with 20 nm diameter NileRed fluorescent beads (Invitrogen). The beam profile was reconstructed by taking the average of 100 individual images collected at different positions to avoid uneven distribution of fluorescent beads.

For the 2D photobleaching gate experiment, the position of the gate laser beam was fixed, and the sample was moved back and forth by a transitional stage (MicroStage 20E, Mad City Labs) in the horizontal direction, until a small area (~3 μm^2) at the center of the ring remains unbleached. The laser beam was then moved back to the original position to locate the unbleached area at the center of the ring-shaped beam. During data acquisition, the gate beam is turned on for 0.2 s every 1.0-2.0 s to bleach out the crossing fluorescent particles. The probability of an EGFR crossing the photobleaching gate is kept below 0.1% by optimizing the timing of the bleaching pattern and the thickness of the ring.

Data Analysis

The position of fluorescent spots was determined by fitting the PSFs to two-dimensional Gaussian function. The positions were fitted throughout the movie except at the frames when the photobleaching events happened or the frames in which the tracked particle overlapped with other fluorophores. The intensity of the spots is estimated by the volume of the 2D Gaussian peak. In a typical assay, we adjusted excitation power to achieve 20-nm localization accuracy at 10 Hz image acquisition rate. Under these conditions, individual eGFP molecules were tracked for 5 s on average.

Two-dimensional diffusion of EGFR spots were analyzed by mean-square displacement (MSD). MSD plots were fitted to quadratic functions, in which first and second order fits represent Brownian motion and unidirectional transport, respectively (Figure 4.1). Most trajectories fit well (R^2 >0.95) to a linear function with a positive y-intercept. Other trajectories were excluded from data analysis to filter out the non-diffusive particles in our dataset. The diffusion constant of individual spots was estimated by the slope of MSD fit. Histograms are fitted by maximum likelihood estimator using original datasets.

4.3 Results

Photobleaching Gate Assay

The photobleaching gate assay utilizes two separate laser beams at the same excitation wavelength. The first laser beam (40 µm diameter) is used to constantly illuminate the sample. The illuminating beam is adjusted to low laser power (0.040 kW/cm^2) to minimize the photobleaching rate. The second beam is converted from a Gaussian beam into a collimated ring-shaped beam by using a pair of axicons, lenses that feature one conical surface and one planar surface (Figure 4.2A). The diameter of the ring is adjusted by the characteristic angle and the distance between axicons. Our ring-shaped beam has a 14-µm inner diameter and a 4-µm thickness at the image plan (Figure 4.3). This gate beam has higher power (52 kW/cm^2) and acts as the photobleaching gate for pre-bleaching the ROI and for preventing new fluorescent molecules from entering the ROI while tracking single molecules.

In a typical assay, the gate beam is first moved in one direction to fully bleach fluorophores in the ROI, only leaving a small elliptical area in the center of the ring to remain fluorescent (Figure 4.2B). The gate beam is then moved back to the center position and acts like a gate to isolate the ROI from the rest of the area. In order to prevent the surrounding fluorophores from entering the imaging area, the gate beam is repeatedly turned on to photobleach the fluorophores that are entering the ROI. As a result, the density of fluorescent objects in the ROI remains low and does not increase over time, as is in the FRAP assay (Figure 4.2C-D). As the photobleaching gate is active, we were able to observe individual fluorophores in the ROI until photobleaching.

When the gate laser beam is turned on, the Raman scattering of water leads to saturation of the camera. In order to achieve single molecule sensitivity, we utilize time-sharing between the gate beam and illuminating beam. In a typical assay, the gate beam is turned on for 0.2 s to bleach fluorescent particles at the periphery of ROI, and turned off for every 2 s to image single molecules within the ROI. Because the fastest diffusing particles we observed had diffusion constants of 0.5 $\mu m^2/s$, we expect only a small fraction (2.3%) of fluorescent particles to pass through the 4-μm-thick gate region without being photobleached. For the majority of the particles (diffusion constant: 0.1 – 0.3 $\mu m^2/s$), the probably of passing the gate when the gate beam is turned off is negligible (<0.1%).

The method greatly reduces the cell autofluorescence in the ROI by repetitive photobleaching the surrounding fluorophores and hence improves the signal to noise ratio (SNR) for in vivo imaging of single fluorophores.

Tracking Single EGF Receptors on COS7 Cell Membrane

Epidermal growth factor receptor (EGFR), a type I receptor tyrosine kinase, functions as a cell surface receptor for epidermal growth factors in extracellular matrix. Mutations affecting EGFR expression has been implicated in a variety of human cancer. Binding of growth factor ligands leads to a transition from inactive monomeric form to an active homodimeric form of the receptor, which initiates EGFR signaling. Preformed inactive dimers may also exist before ligand binding. The detailed mechanism of receptor activation pathway is poorly understood, because EGFR dimerization is a dynamic process and cannot be studied directly using ensemble methods in live cells.

Early experiment used low concentration of fluorescently labeled EGF to track the behavior of single EGFR (Sako 2000). However, this method was unable to reflect the location of EGFR without attachment of EGF. Also, labeled EGF might detach on one receptor and re-attach to another receptor and lead to jump diffusion behavior. EGFR has also been tracked by antibody-coated quantum dot (Chung 2010 Nature), but the labeling of the extracellular part of EGFR might interfere with the dynamics of EGF binding.

In order to study the oligomeric states of EGFR in real time, we expressed eGFP-fusion of EGFR in COS7 cells. The cells are immobilized on a glass surface and imaged under the total internal reflection (TIR) illumination mode. Because the cell membrane was densely covered with GFP-labeled EGFR (400 ± 55 molecules/μm^2, SEM, N=36), it was not possible to track individual molecules in conventional TIR images. Using a conventional FRAP assay, we photobleached a 22-μm diameter area on a cell membrane (Figure 4.2C), and occasionally, we were able to observe single fluorophores appearing in the bleached area during the fluorescence recovery. These particles can be tracked for a few frames until the density of fluorophores increase at a level where single molecules cannot be distinguished from each other. However, the analyses of diffusional motion of those particles leads to overestimation of the average diffusion constant, because the particles that appear first at the center of ROI usually diffuse faster than most particles (D = 0.1-0.3 μm^2/s). Thus, not only FRAP is inefficient in terms of tracking time, but it also biases the diffusion constant measurement toward higher values.

We next tested whether the photobleaching gate assay provides unique advantages in tracking the diffusion of single EGFR on the mammalian cell membrane. The positions of the receptors were tracked by two-dimensional Gaussian fitting at 22 nm precision (Figure 4.2D, Figure 4.4A). We tracked the diffusional motion of single GFP spots for 5-10 s until they photobleach. The diffusion constants are estimated by linearly fitting the mean-square-displacement plot for each molecule (Figure 4.4B). We observed significant difference in diffusion constants with and without EGF (t-test, p-value <0.01). In the absence of EGF in the serum, the majority (91%) of EGFR stay at a more diffusive state (D = 0.25 μm^2/s) and only 9% were found at a less diffusive state (D = 0.12 μm^2/s, N=85) (Figure 4.4C). With the addition of EGF (concentration = 16 nM), we observed a large shift in population towards the less diffusive state. 84% of the spots (N=82) appeared in the less diffusive state, while only 16% of the population remains in the more diffusive state (Figure 4.4D). The results show that diffusion of EGFR molecules slow down approximately by a factor of two upon addition of EGF, in agreement with EGFR dimerization in the signaling pathway.

The analysis of fluorescent intensity of individual spots revealed the oligomeric state of diffusing EGFR spots. In the absence of EGF, 90% (N=31) of the EGFR molecules display one-step photobleaching (Figure 4.4E, Figure 4.5A), indicating that there is a single GFP in most fluorescent spots. In the presence of EGF, we observed 47% of the spots (N = 17) to bleach in two steps (Figure 4.4F, Figure 4.5A), suggesting that EGFR molecules form a dimer containing two GFPs per spots upon EGF addition. Spots that bleach in two steps diffuse slower (D = 0.15 μm^2/s without EGF, D = 0.13 μm^2/s with EGF) compared to molecules with only one fluorophores (D = 0.22 μm^2/s without EGF, D = 0.19 μm^2/s with EGF) (Figure 4.5B), strongly indicating that the more diffusive particles are mostly monomers and the less diffusive particles are mostly dimers. We note that the percentage of

molecules that shows two-step bleaching (47%) behavior is not as high as the percentage of molecules at the less diffusive state (84%) in 16 nM EGF. This could be due to incomplete maturation of GFP in cells. Only ~70% of GFP molecules folds properly, hence the maximum percentage of two-step bleaching that can be observed is 46%, which is similar to our observations.

The photobleaching gate method also allows us to observe state transitions of single molecules. In the presence of EGF, diffusing EGFR molecules pause transiently and then resume diffusion (Figure 4.4G). This pausing behavior may be due to docking and undocking from a stationary structure on the membrane. These stationary states may well reflect the transient interactions between EGFR and membrane domains (Low-Nam et al., 2011), as well as cortical actin meshwork (den Hartigh et al., 1992; Morone et al., 2006). As a result, tracking the individual EGFR receptors in a cell membrane using the photobleaching gate assay not only reveals their diffusional motion, but provide direct information about the oligomeric state of the receptors.

4.4 Discussion

Our method is directly comparable to photoactivation. One advantage of photoactivation is that only small number of molecules are activated per round, allowing long term of measurements without photobleaching significant portion of fluorescent molecules. The advantage of our method is that it does not rely on fusing photoactivable probe fusions to our protein of interest. As a result, the method provides single molecule sensitivity without requiring genetic modification and testing of new cell lines. Cells that express conventional fluorescent probes can be used in both photobleaching gate assay and other imaging methods (e.g. FRAP, confocal, TIRF…), making it possible to directly compare the results obtained from these assays. Most photoactive fluorescent proteins are much dimmer compared to best performing fluorescent proteins (such as eGFP) which can be used in photobleaching gate assays. Furthermore, the photobleaching gate assay is more suitable to study the cluster formation. As it is difficult to photoactivate the majority of fluorophores in a single cluster without activating the neighboring molecules, bleaching all the fluorophores except the majority on a single cluster is relatively easy to achieve. The photobleaching gate method also allows us to improve the precision of measurements by tagging the target molecules with multiple fluorophores.

To conclude, the photobleaching gate assay has allowed us to gain a number of insights into the kinetic mechanism of IFT at the single-molecule level. It provides us with abundant information with regard to the turnaround point at the flagellar tip, including mixing, splitting, remodeling, and switching between microtubules, that could not be resolved by traditional fluorescent or DIC microscopy. We anticipate that our method is broadly applicable to single particle tracking studies in live cells.

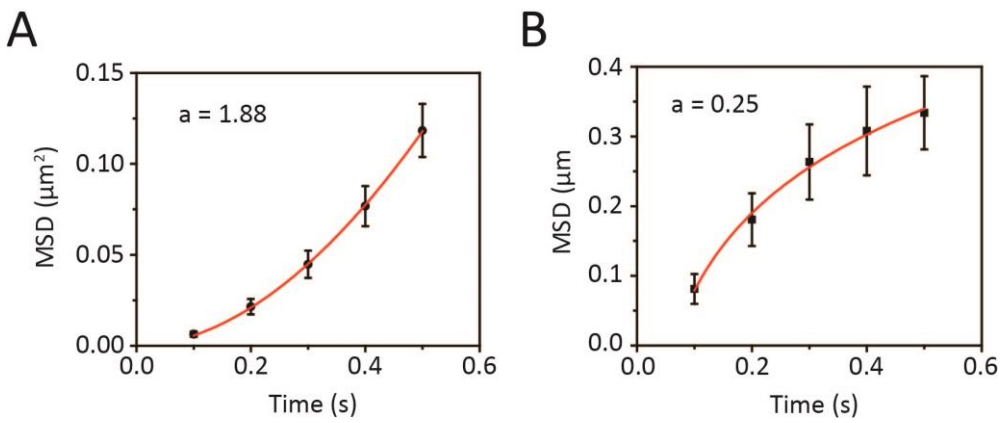


Figure 4.1 MSD Plot of Non-Diffusive Behavior

(A) MSD plot of a molecule in direct transport. The data fitted to $y = c_1 x^a + c_2$ shows an exponent larger than 1.

(B) MSD plot of a molecule in confined diffusive motion. The data fitted to $y = c_1 x^a + c_2$ shows an exponent smaller than 1.

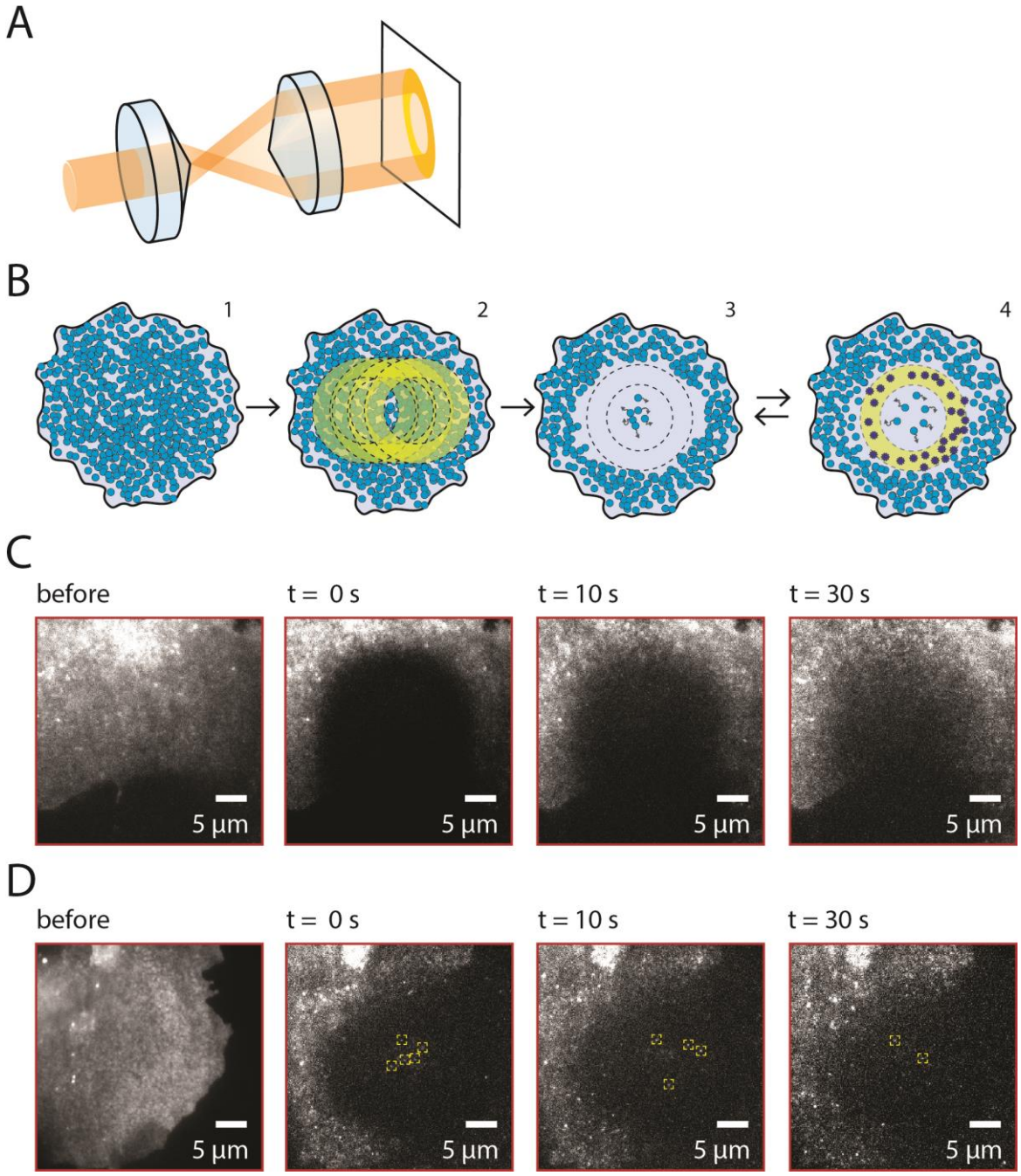


Figure 4.2 Observing Single EGF Receptors with the Photobleaching Gate Assay

(A) Schematic drawing of a ring-shaped laser beam created by a pair of axicons. The diameter of the ring is determined by the distance between the two axicons, and the thickness is determined by the size of the incoming laser beam.

(B) Schematic representation of the photobleaching gate assay. 1) Surface adhered cells are continuously monitored by a low-power TIRF illumination beam. 2) The gate beam is turned on and moved in a single direction to photobleaching all fluorophores in the ROI, except those in the middle area. 3) The gate beam is then turned off and moved to the center position. 4) The gate beam is then repeatedly turned on to photobleach the entering particles.

(C) Fluorescent images of EGFR-GFP in a FRAP experiment showing a continuous recovery of fluorescent intensity.

(D) Fluorescent images of EGFR-GFP during a photobleaching gate experiment. Single molecules identified in the ROI are marked by yellow boxes.

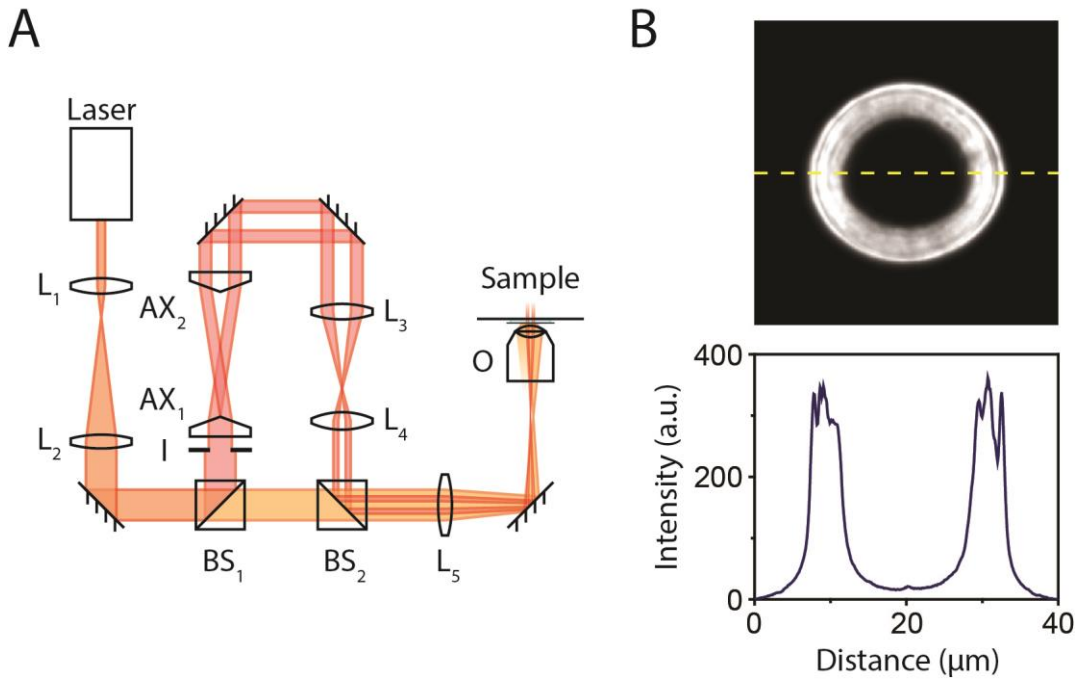


Figure 4.3 Photobleaching Gate Setup

(A) Optical path for the photobleaching gate setup. The laser beam first passes through a beam expander (L1, L2), and then are separated by a beam splitter (BS1) into two polarized laser beam. One of the polarized beams passes through an iris (I) to clean up the edge, and then is sent into a pair of axicons (AX1, AX2) to reshape into a ring-shaped beam, and is resized by a telescope (L3, L4). The two beams are combined by another polarized beam splitter (BA2) and is sent to the TIRF lens (L5) and the objective (O).

(B) (top) beam profile of the ring-shaped gate beam showing on a uniform bead sample. (bottom) Intensity of the beam in the top image across the yellow dashed line.

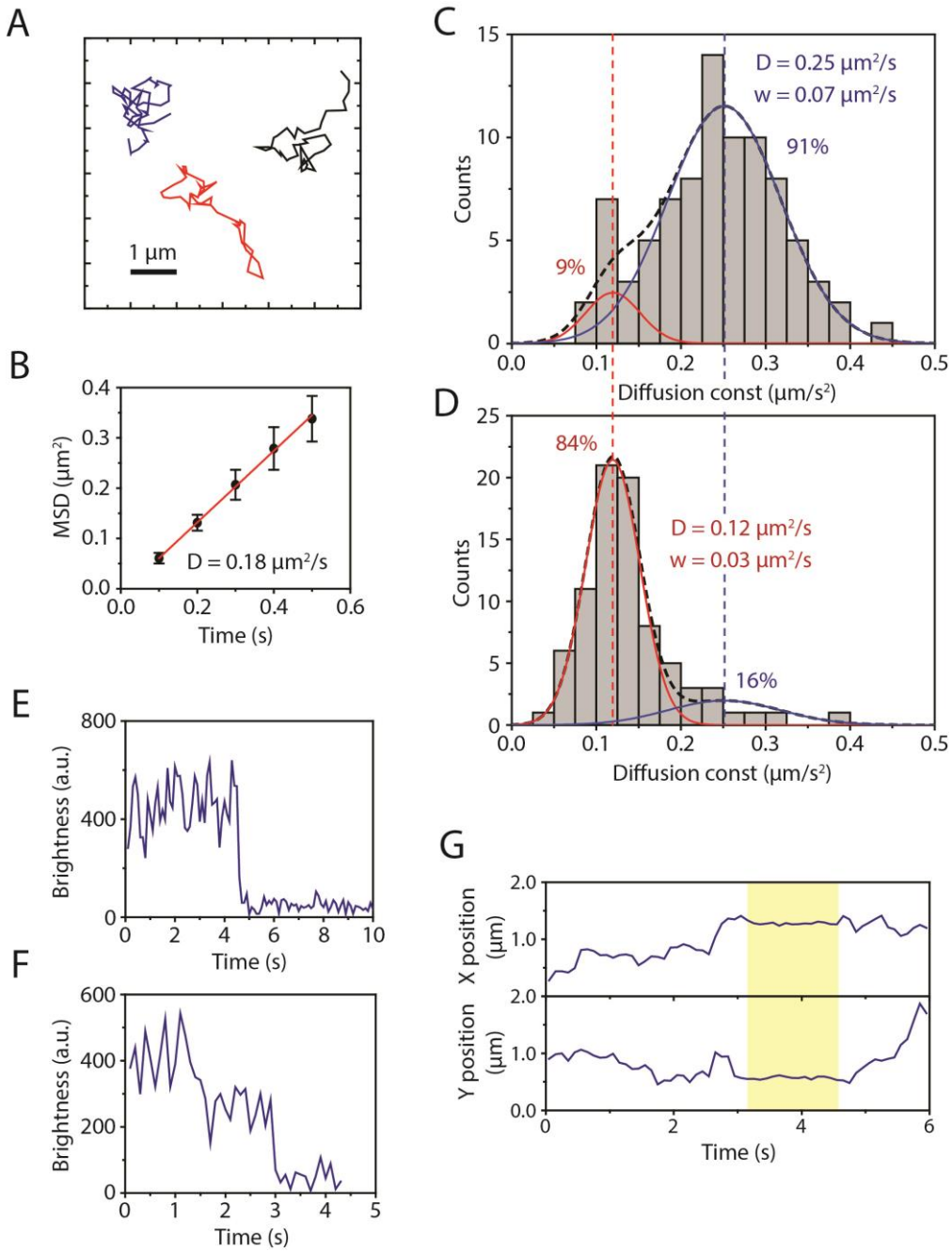


Figure 4.4 Diffusion Study of EGF Receptors

(A) Trajectories of three individual GFP-EGFR spots diffusing in a COS7 cell membrane.

(B) Mean squared displacement plot of an example trajectory. The slope of the linear fit (red line) represents the diffusion constant.

(C) Diffusion constant histogram of EGFR spots in the absence of EGF. Multiple Gaussian fit (black dotted curve) reveals two major peaks. 91% of the spots diffuses with D = 0.25 ± 0.07 $\mu m^2/s$ (more diffusive state, blue curve) and 9% with D = 0.12 ± 0.03 $\mu m^2/s$ (less diffusive state, red curve)

(D) Diffusion constant histogram of EGFR spots in the presence of 16 nM EGF. Addition of EGF results in the 75% of the spots shifting from the more diffusive to the less diffusive state.

(E) An example intensity profile of an EGFR spot shows a single step photobleaching in the absence of EGF.

(F) Intensity profile of an EGFR spot photobleaches in two-steps, showing the existence of two GFPs on a spot, in the presence of EGF.

(G) An EGFR molecule switches between diffusive state and stationary state in the presence of 16 nM EGF. The stationary state is marked with yellow background.

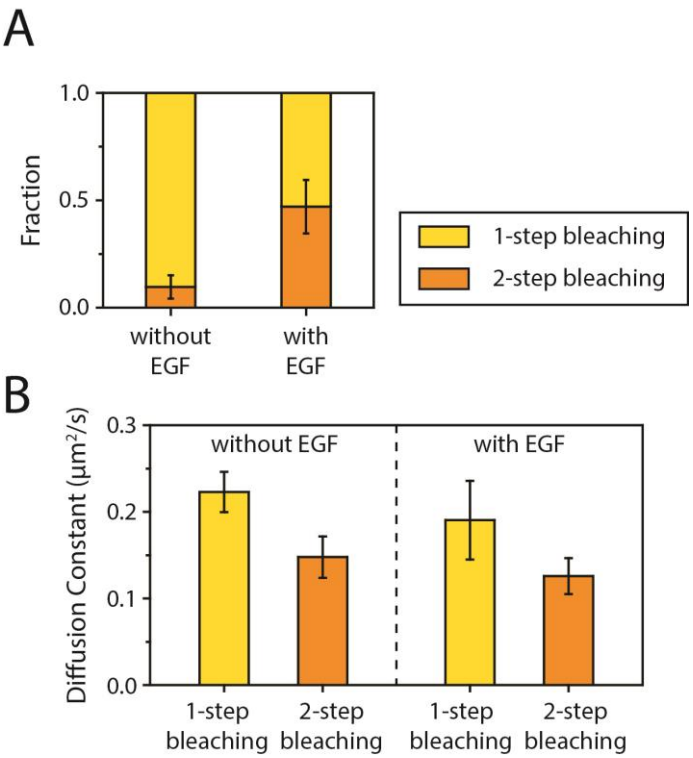


Figure 4.5 Counting Fluorophores on EGFR Clusters

(A) Fractions of one-step bleaching clusters and two-step bleaching clusters with and without EGF. (B) Diffusion constants of clusters that show one-step photobleaching and two-step photobleaching.

Chapter 5. Single Molecule Analysis of IFT Turnover at Flagellar Tip of *Chlamydomonas*

5.1 Introduction

IFT is a universal process that is required for the assembly of most eukaryotic cilia and flagella (Ishikawa and Marshall, 2011; Rosenbaum and Witman, 2002). In IFT, axonemal precursors and receptor molecules are transported by heterogeneous arrays of multiprotein complexes (IFT trains) coupled to microtubule motors between the flagellar membrane and the axoneme (Kozminski et al., 1993). Kinesin-2 motors carry IFT trains in continuous anterograde streams from cell body to flagellar tip (Cole et al., 1998). Anterograde IFT trains are larger in size and less frequent; retrograde IFT trains are smaller in size and more frequent (Pigino 2009). Therefore, IFT complexes are expected to reorganize at the distal tip and the flagellar base (Pazour et al., 1999; Porter et al., 1999). The exchange between kinesin and dynein motors is also expected to occur at the tip and base of the flagella (Pigino 2009).

Because multiple trains coexist in these turnaround zones, it is not possible to directly observe individual IFT trains reorganization by conventional TIRF imaging. Using the photobleaching gate assay, we controlled the number of fluorescent particles in flagella and detected the arrival and departure of single IFT trains and motor complexes from the flagellar tip. We observed that kinesin-2 motors dissociate from IFT trains at the tip, contrary to the current model in the field. In addition, we directly observed flagellar waiting time and splitting of IFT trains into multiple complexes under different drug treatments. The results led to a quantitative model involving IFT mixing and remodeling at the flagellar tips.

IFT motors and cargos are recycled during this process; because IFT remains unabated for several hours under inhibition of protein synthesis (Iomini et al., 2001). It remains unclear how IFT trains reverse their direction at the flagellar tip and base (Laib et al., 2009). It is possible that regulatory complexes located at the base and tip of the flagellum enforce efficient transport of cargos by allowing only one type of motor to be active at a time (Vale, 2003). Alternatively, cargos may reverse their direction of motion through a tug-of-war mechanism (Hendricks et al., 2010). In this chapter, we applied a one-dimensional photobleaching gate assay that uses a circular laser beam as the gate to monitor the dynamics of intraflagellar transport (IFT) complexes at the tip of *Chlamydomonas* flagella.

5.2 Methods

Sample Preparation

The IFT27-GFP mt+ strain was provided by J. Rosenbaum. IFT27-GFP pf18 strain was generated through crosses. The *pf18* mt- (cc1297) strain was obtained from the *Chlamydomonas* Resource Center. Vegetative cells were grown in TAP media at 22 ℃. The

IFT20-GFP ΔIFT20 strain was provided by K. Lechtreck and G. Witman. Compared to IFT27-GFP, IFT20-GFP::ΔIFT20 cells have higher level of fluorescence because IFT particles are completely labeled. This strain is used for 3D tracking because the labeled IFT trains produce more photons. *Chlamydomonas* cells were immobilized to glass surface, as described previously (Shih et al., 2013).

Microscope

An objective-type TIRF microscope was set up, using a Nikon TiE inverted microscope equipped with a perfect focusing unit, bright-field illumination and a 100X 1.49 NA PlanApo oil immersion objective (Nikon). A 488 nm solid state laser (Coherent) was used for GFP excitation. The GFP signal was recorded by an Andor iXon 512 x 512 electron-multiplied charge-coupled device (EM-CCD) camera. 1.5x extra magnification was used to obtain a pixel size of 106 nm. Data was collected at 10 Hz time resolution. Excitation of the laser beams were controlled by Uniblitz shutters. Because CCD image is saturated under intense laser illumination, shutter timing was synchronized with the camera acquisition by a data acquisition card (NI, USB-6221) to minimize the number of "dead" frames in recorded movies.

In order to determine the z position, a cylindrical lens (f = 400 mm) was inserted in front of the CCD camera, giving a detection range of ±250nm in z direction. This range covers the full extent of the thickness of a *Chlamydomonas* flagellum (~250 nm). The z-calibration is done by scanning a sample sparsely decorated with 20-nm fluorescent beads in the z direction at 30-nm increments (Figure 5.7). The PSFs of individual particles at each height are fitted by an elliptical Gaussian algorithm. z position is calibrated based on the eccentricity of the Gaussian, as demonstrated previously. Sample depth is adjusted by the including effective refraction index in a calibration routine (Huang et al., 2008).

The Photobleaching Gate Assays

The beam profile was tested by exciting a coverslip densely coated with 20 nm diameter NileRed fluorescent beads (Invitrogen) (Figure 5.3). The beam profile was reconstructed by taking the average of 100 individual images collected at different positions to avoid uneven distribution of fluorescent beads.

For the 1D photobleaching gate assays, a high-power (30 mW) collimated laser beam in epifluorescence mode with a diameter of 3 μm was used for photobleaching. Because the assay requires a sharp transition between bleached and unbleached regions, a typical Gaussian beam (TEM_{00} mode) is not ideal for excitation. To reshape the laser beam, an iris was placed at the conjugate plane of the image plane. The resulting beam at the image plane consists of a combination of higher cylindrical transverse modes (Figure 5.3). For 1D assays on IFT in *Chlamydomonas*, flagellar orientation of surface adhered cells were visualized by TIRF imaging. The microscope stage was moved to bring the gate beam at the tip of flagellum. The

stage was then moved along the flagellar orientation to prebleach the distal half of the flagellum. The gate beam is turned off when it is positioned near the base of the flagellum to allow single anterograde IFT train to enter the flagellum. The gate beam is then turned on for 0.2 s at every 1 s to bleach other anterograde trains. Because IFT trains move at slightly different speed, individual trains can be distinguished as they move along the flagellum. The locations of flagellar tips were determined by brightfield imaging (data not shown).

Data Analysis

The position of fluorescent spots was determined by fitting the PSFs to two-dimensional Gaussian function. The positions were fitted throughout the movie except at the frames when the photobleaching events happened or the frames in which the tracked particle overlapped with other fluorophores. The intensity of the spots is estimated by the volume of the 2D Gaussian peak. In a typical assay, we adjusted excitation power to achieve 20-nm localization accuracy at 10 Hz image acquisition rate. Under these conditions, individual eGFP molecules were tracked for 5 s on average.

In IFT measurements, anterograde and retrograde particles are manually assigned. For a single anterograde particle that splits into multiple retrograde particles, the return time for all retrograde particles were counted and the position of all retrograde particles were fitted individually. The return time for IFT27-GFP is defined as the time the particle stays within the tip area.

5.3 Results

We first monitored IFT in cells that had adhered both flagella to the glass surface by using TIRF illumination without photobleaching. We tracked the transport of IFT27, a core component of IFT complex B, using an IFT27-GFP pf18 strain (Qin et al., 2007). IFT trains moved unidirectionally along the length of flagella, reversing direction at the flagellar tip and the base (Figure 5.1A). The anterograde IFT27 speed was 2.1 ± 0.4 μm/s and the retrograde speed was 3.0 ± 0.7 μm/s (mean ± SD, N = 80) (Figure 5.2). Large number of trains was observed to accumulate at the tip. Therefore, it was not clear how long anterograde trains wait at the tip before moving back in retrograde direction, and whether IFT complexes in anterograde trains disassemble upon tip arrival and reassemble with other complexes at the tip to form retrograde IFT trains.

We controlled the number of fluorescent particles at a flagellum using a one-dimensional (1D) version of the photobleaching gate assay (Figure 5.1B). In this assay, we initially photobleached all of the fluorophores at distal parts of a flagellum by a large photobleaching beam. The first beam is turned off to allow fluorescent anterograde trains to enter the flagellum. We next turned on a second photobleaching beam (3-μm diameter, 420 kW/cm^2) near the base of flagellum to serve as a gate to control the number of fluorescent particles entering the flagellum. In order to create a sharp transition between bleached and

unbleached particles, we reconstructed a combination of higher cylindrical transverse modes of the laser at the image plane, instead of using a typical Gaussian beam (TEM00 mode) (Figure 5.3). In a typical assay, after allowing a single unbleached IFT train enters the flagellum, the gate beam is turned on for 0.2 s at the frequency of 1Hz. Trains moving slower than the cutoff speed (3.0 μm/s) towards the ROI were photobleached by the gate. 98% of anterograde IFT trains move slower than 3.0 μm/s, and hence cannot escape the gate.

The assay revealed the full range of movement for single complexes within the flagellum (Figure 5.1C and Figure 5.4). IFT movement can be divided into three stages: unidirectional moving toward the tip, pausing at the tip, and returning back toward the base by retrograde transport. We directly observed that a single anterograde train splits into multiple retrograde trains (Figure 5.1C), in agreement with higher frequency observed for retrograde movement, compared to anterograde IFT (Dentler et al., 2005). Remarkably, the fluorescence signal of a single anterograde train was observed on 2.4 retrograde trains on average (N=97), which was significantly higher than the ratio of retrograde to anterograde train frequencies observed in TIRF assays (Dentler et al., 2005; Engel et al., 2012). On the basis of these results, we propose that single anterograde trains do not only split into multiple retrograde trains at the tip, but also recombine with each other.

To test whether IFT trains recombine at the tip, we used a slightly modified version of the photobleaching gate method. Instead of allowing a single IFT train to enter to the distal half of the flagellum, we closed the gate after two or three fluorescent anterograde trains enter the flagellum within a two-second window (Figure 5.1D-E). We measured the number and return frequency of retrograde fluorescent traces generated as a function of numbers of bright anterograde trains. If individual trains split and return without mixing with each other, the number and frequency of the returning trains would increase linearly with the number of anterograde trains. Conversely, if there is a large pool of IFT particles present at the flagellar tip in a steady state and IFT trains mix perfectly with each other, the number and frequency of returning retrograde trains would be nearly independent on the number of incoming trains. We observed 2.4, 3.6 and 4.2 returning trains on average for one, two and three incoming trains, respectively (Figure 5.5A) (N=97, 60, 42). The return frequencies for one, two and three incoming fluorescent trains were 0.57, 0.71 and 0.76 s^{-1}, respectively (Figure 5.5B). These results show that IFT trains mix with each other at the flagellar tip.

We define the tip return time to be the average time between the arrival of an anterograde train and the initiation of the first retrograde train. The average time that IFT trains start to move retrogradely from the flagellar tip was 3.1 ± 0.3 s (Figure 5.5B-C) (N=97). The tip return time histogram of IFT trains fits well to a gamma distribution with a shape parameter of 3.09 (Figure 5.5C), indicating that the return processes consists of three rate-limiting steps.

We next calculated the return time of the 1st, 2nd, 3rd and 4th IFT trains after the arrival of a single fluorescent anterograde train. The average return time increases linearly with an increment of 1.7 s per retrograde train and the linear fit intersected the y-axis at 1.3 s (Figure 5.5B). Assuming the initiation of retrograde IFT trains is purely stochastic (e.g. a Poissonian process) after the remodeling of IFT complexes, the slope represents the inverse of the rate at which IFT trains depart at the tip, and the y-intercept represents the IFT remodeling time at the tip. By separately fitting the return time of the 1st, 2nd, 3rd and 4th IFT trains into a gamma distribution with a free shape parameter, we concluded that tip remodeling time is limited by one rate and the initiation time of retrograde IFT trains is limited by two rates (Figure 5.6).

During the IFT remodeling at the tip, it was unclear if the IFT particles stay in contact with or detach from the microtubules. If the particles return without releasing from the microtubule, we expect retrograde trains to follow the same microtubule track with the anterograde train. However, if anterograde trains dissociate from the axoneme when they arrive at the tip, we expect to observe less correlation between the microtubule tracks of anterograde and retrograde trains. To address this question, we tracked IFT trains in three dimensions by inserting a cylindrical lens into the detection path and calibrating the z-position with 22 nm accuracy from the ellipticity of the PSFs (Huang et al., 2008) (Figure 5.7). The precision in x- and y-positions of the PSF was 16 nm.

Using the photobleaching gate method, we tracked single IFT trains arriving and departing from the flagellar tip (Figure 5.8A-B), and we observed that both anterograde and retrograde trains moved linearly along the axoneme with ±21 nm standard deviation in lateral position. Assuming the fluctuation is uncorrelated with the detection noise, the trajectory of IFT trains fluctuate ±13 nm in perpendicular axis, suggesting that they follow a single microtubule track (24 nm wide) along the length of flagellum. However, the average lateral distance between anterograde and retrograde trajectories emanated from these trains was 71 nm, which is significantly higher than the width of a single microtubule filament. Therefore, we concluded that IFT trains dissociate from axonemes at the tip and retrograde trains are redistributed into the nine microtubule doublets (Figure 5.8C-D, Figure 5.9). Consistent with our results, electron micrographs showed that IFT trains detach from microtubules and associated with the membrane at the flagellar tip (Dentler et al., 2005).

We next examined the movement of kinesin-2 motors, using a KAP-GFP fla3 strain. KAP, the nonmotor subunit of heterotrimeric kinesin-2, localizes kinesin to the flagellar base, where IFT trains are assembled (Mueller et al., 2005). We observed that KAP-GFP moved primarily in the anterograde direction to the flagellar tip, at similar speeds (2.0 ± 0.3 μm/s, mean ± SD) and frequencies (1.35 s^{-1}) to anterograde IFT27-GFP (2.1 ± 0.4 μm/s and 1.06 s^{-1}). In contrast to IFT27-GFP, high GFP background fluorescence was measured throughout KAP-GFP flagella. Retrograde transport of KAP was rarely observed, and the way kinesin-2 motors move back to the cell body could not be determined by the standard TIRF assay

(Engel et al., 2012). It was unclear whether the fluorescent signal of retrograde KAP traces is over-shadowed by the background fluorescence (Engel et al., 2009) (Figure 5.10A) or kinesin-2 moves back to the cell body independent of retrograde IFT, contrary to the current model in the field (Rosenbaum and Witman, 2002; Ishikawa and Marshall, 2011).

We applied the photobleaching gate assay to determine the return mechanism of KAP to flagellar base. Fluorescent spots of KAP-GFP moved to the flagellar tip by active transport. After waiting for a short period of time at the tip, individual KAP clusters moved away from the tip by rapid saltatory motion (Figure 5.10B). Unlike IFT, KAP does not frequently split at the flagellar tip or during the saltatory movements, even though each anterograde train is driven by multiple kinesin-2 motors (Laib et al., 2009; Engel et al., 2012; Shih et al., 2013). Only 11% of the anterograde KAP clusters split into more than one separate clusters at the tip (Figure 5.10C). We tracked the position of KAP clusters at 16 nm precision. Mean square displacement (MSD) analysis showed that KAP performs one-dimensional diffusion within the flagella during this process (Figure 5.10D - F). Average diffusion constant of 27 individual traces was 1.7 $\mu m^2/s$, comparable to diffusion constants of individual complexes within the cytoplasm. We next investigated whether KAP linearly diffuses along the microtubule track, similar to a non-processive microtubule-depolymerizing kinesin, MCAK (Helenius et al., 2006). In this case, KAP clusters are not expected to move freely along the perpendicular axis of the axoneme, so the fluctuation in KAP position at the perpendicular axis would be similar to the error of the tracking method. However, the measured lateral fluctuation was ±60 nm (Figure 5.10D, Figure 5.12), indicating that KAP diffuses independent of microtubules within the flagella (Figure 5.10D).

To investigate whether diffusion of KAP clusters within the flagellum could be effectively recycled back to the cell body, we performed fluorescence recovery after photobleaching (FRAP) assay in the middle sections (~5 μm) of full-length flagella (Figure 5.11A). Directional movements of KAP-GFP trains into the photobleached area were seen from the anterograde direction, whereas recovery of GFP fluorescence from the retrograde direction was primarily due to the diffusion of the high GFP background (Figure 5.11A). Diffusion constant calculated from one dimensional FRAP analysis (1.8 ± 0.1 $\mu m^2/s$, Figure 5.11B) was comparable to the result of the MSD analysis. We also observed a concentration gradient for the fluorescent background that increases towards the tips of flagella (Figure 5.11C), suggesting that there is a net flux of KAP clusters towards the cell body. These results show that the high level of fluorescent background in flagella of the KAP-GFP strain (Figure 5.10A) was formed by KAP clusters dissociated from IFT trains at the flagellar tip.

We have applied a new photobleaching gate technique to investigate the mechanism of IFT returns. Retrograde transport of kinesin-2 during intraflagellar transport was previously observed in C. elegans cilia (Signor et al. 1999), suggesting that opposite polarity motors (kinesin and dynein) in IFT recycle each other as an inactive passenger on IFT trains. Similar

models were proposed for *Chlamydomonas* (Rosenbaum and Witman, 2002), because inhibition of one type of a motor fully stops IFT, and kinesin and dynein motors do not engage on a tug-of-war with each other (Kozminski et al., 1995; Pazour et al., 1999, Shih et al., 2013). We showed that KAP detaches from IFT trains at the flagellar tip and moves back to the cell body by diffusing inside the flagellum. It remains unclear why KAP mostly diffuses as a cluster in flagellum, instead of splitting into individual molecules. KAP subunits may be bound to each other by weak interactions, and can split up or recombine during diffusion. Because KAP is shown to provide a physical link between kinesin-2 and the IFT particle in C. elegans (Ou et al., 2005) and kinesin-2 is autoinhibited by its tail without KAP (Brunnbauer et al., 2010), we propose that the kinesin-2 heavy chain also dissociates from the IFT trains and diffuses back to the cell body in *Chlmaydomonas* Consistent with our model, the kinesin-2 heavy chain does not accumulate in flagella when retrograde IFT is impaired (Pedersen et al., 2006). Releasing of kinesin-2 at the tip may be the mechanism to avoid tug-of-war between kinesin-2 and dynein-1b during the transport of retrograde trains.

5.4 Discussions

Diffusion of kinesin-2 to the flagellar base requires a large pool of protein in the flagellum. In a 15-µm-long flagellum, it takes 7.1 s for KAP to travel from the base to the tip by retrograde transport, but recycling back to the base via diffusion takes 130 s on average. Therefore, we estimated that free KAP molecules in flagellum are 18 times more abundant than the amount of KAP required balancing of the material at a steady state if all KAP molecules were transported by IFT trains in the retrograde direction. The data imply that KAP is present in high quantities throughout the flagellum, but is only activated at the loading zone located at the base of the flagellum. Diffusion flux of KAP at a steady-state requires a fix concentration gradient, and the total amount of KAP localized to the flagellum scales with the square of its length. It is possible that diffusion of KAP, or another flagellar component, may function as a feedback mechanism to control the flagellar length. As the flagellum gets longer, the “length sensor” accumulates within the flagellum, limiting the total amount of the sensor available in the loading zone.

IFT trains move unidirectionally along the length of the flagellum and only reverse their direction at the flagellar base and the tip (Kozminski et al., 1993). The lack of saltatory IFT movement suggests that only one type of a motor is active at a time. Moreover, kinesin and dynein motors need to move back to the flagellar base and tip, respectively. In *Chlamydomonas*, motor recycling can occur for several hours, as IFT continues unabated after complete inhibition of protein synthesis (Piperno and Mead, 1997). The current model for IFT suggests that dynein-1b travels to the flagellar tip as an inactive passenger on anterograde IFT trains (Pedersen et al., 2006). At the tip, dynein is activated and kinesin is deactivated by an uncharacterized pathway to facilitate the reversal of cargo transport. The

clear implication of this model is that regulatory proteins must be localized near turnaround zones at both ends of the flagellum (Vale, 2003).

On the basis of our results, we propose a model that involves coordinated engagement of kinesin and dynein motors to IFT trains at the flagellar base and tip (Figure 7C). Kinesin-2 motors transport IFT complexes from the base to the tip. Dynein-1b is believed to be carried to the tip as a passive cargo on anterograde trains. At the flagellar tip, the KAP subunit (or the entire kinesin-2 complex) dissociates from IFT trains, and dynein-1b motors attach to IFT trains actively interact with the microtubule surface to initiate retrograde transport. This model is consistent with the reversal of cargo movement at turnaround zones and unidirectional cargo transport along the length of flagella, without requiring regulatory proteins on IFT trains to facilitate cross-activation and deactivation of kinesin and dynein. Kinesin-2 and dynein-1b may bind to a common IFT subunit (Deacon et al., 2003) and modification of this subunit (such as phosphorylation) may control detachment of kinesin-2 from IFT particles and activation of dynein-1b at the flagellar tip. Alternatively, anterograde and retrograde particles may be distinct species such that retrograde trains possess a subunit for dynein attachment, but not for kinesin. Further work is required to monitor the dynamic turnover of dynein-1b and kinesin-2 heavy chains in flagella.

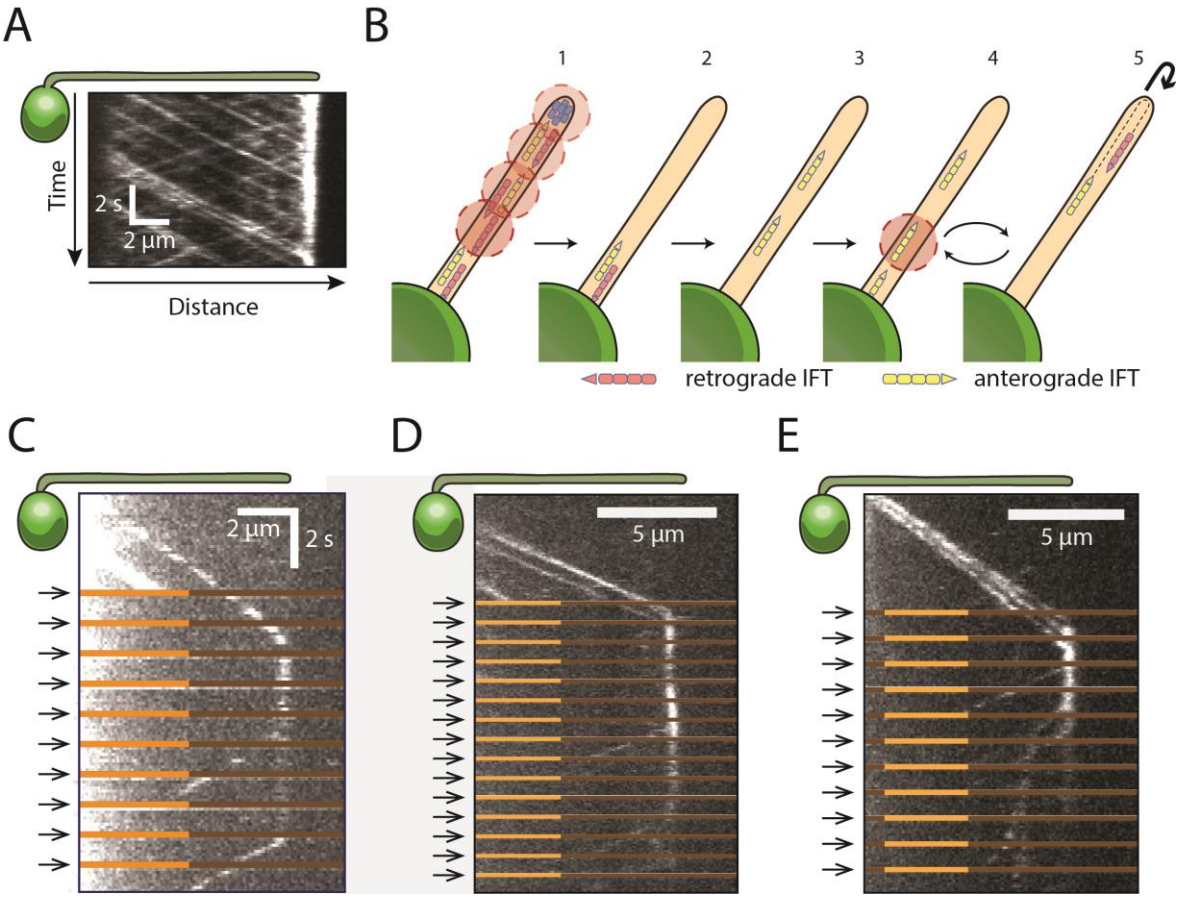


Figure 5.1 Photobleaching Gate Assay on *Chlamydomonas* IFT

(A) Kymograph of an IFT27-GFP cell, showing that IFT trains move bidirectionally along the flagellum, only reversing direction at the tip and the base. Multiple IFT trains accumulate at the flagellar tip.

(B) Schematic representation of the photobleaching gate assay. Surface adhered cells are continuously monitored by low-power TIRF illumination. 1) The distal half of the flagellum is prebleached by scanning the gate beam from the flagellar tip to the middle. 2) The gate beam is turned off to allow a single particle to enter the flagellum. 3) The gate beam is turned again on near the base of the flagellum to control the number of fluorescent particles entering the flagella. The photobleaching gate beam is then repeatedly 4) turned on for a short period of time (0.2 s) to photobleach the particles and 5) turned off for 0.8 s to allow imaging single molecules at a low fluorescent background.

(C) Kymograph analysis of an IFT27-GFP cell imaged by the photobleaching gate assay. IFT trains display processive movement in the anterograde direction, pause at the flagellar tip, and move back to the flagellar base by processive movement.

(D) Kymograph of an IFT27-GFP cell imaged by the photobleaching gate assay. Two fluorescent IFT trains are allowed to enter the flagellar, and the fluorescence was observed on two retrograde trains.

(E) Kymograph of an IFT27-GFP cell imaged by the photobleaching gate assay. Three fluorescent IFT trains are allowed to enter the flagellar, and the fluorescence was observed on three retrograde trains.

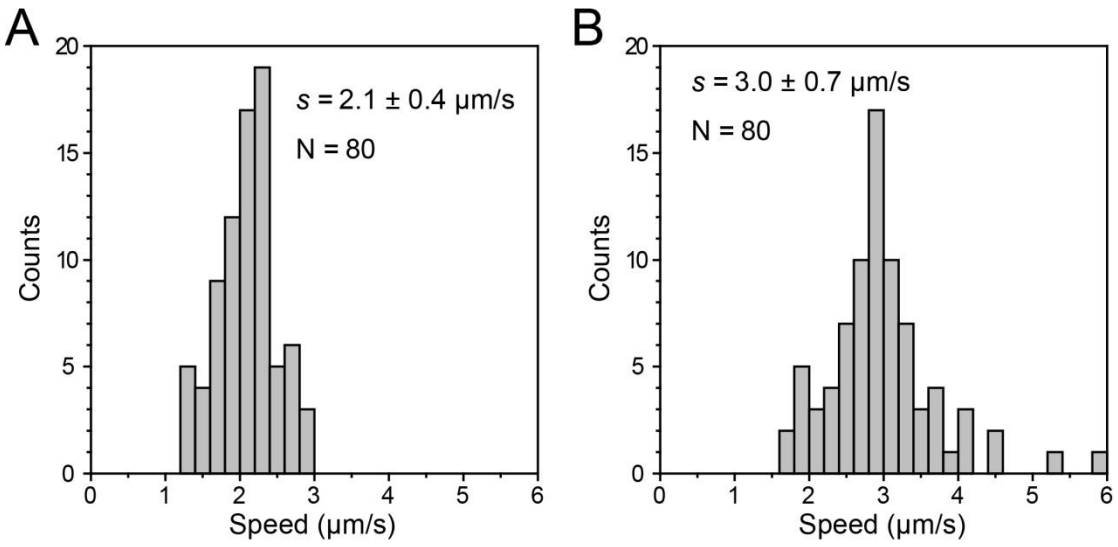


Figure 5.2 Speed of IFT trains

(A) Histogram of anterograde IFT trains speed.
(B) Histogram of retrograde IFT trains speed.

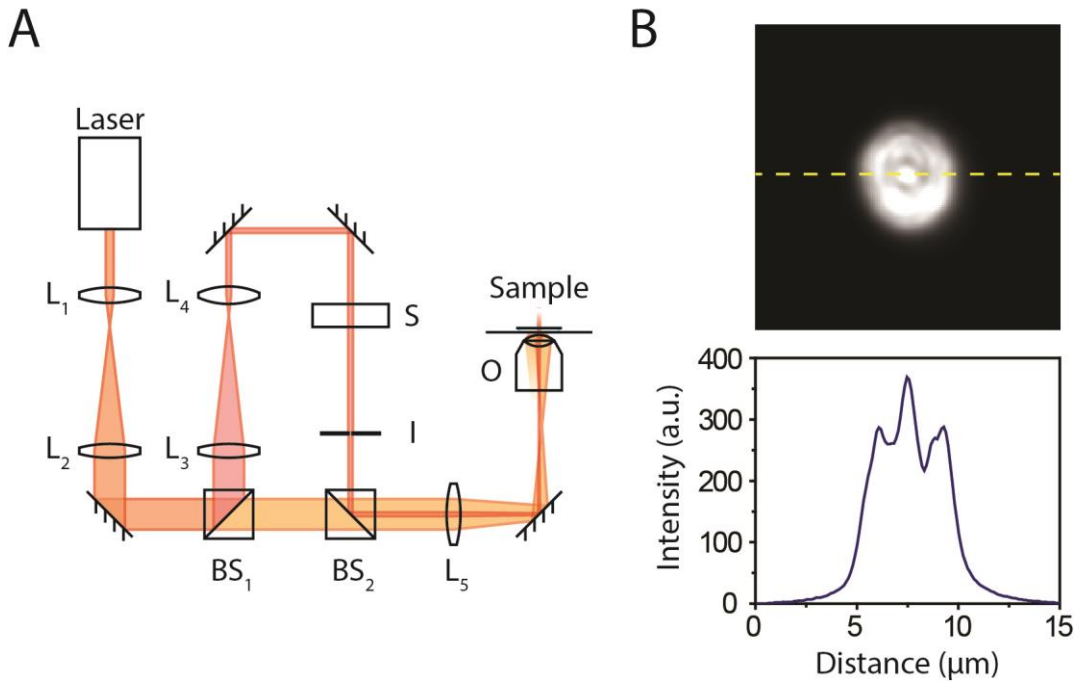


Figure 5.3 1D Photobleaching Gate Setup

(A) Optical path for the photobleaching gate setup. The laser beam first passes through a beam expander (L1, L2), and then separates into two polarized laser beam using a beam splitter (BS1). One of the polarized beams first passes through a telescope (L3, L4) to adjust the beam size, and then goes through a iris (I) to clean up the edge. The shutter (S) is used to control the timing of the laser beam. The two beams are combined by another polarized beam splitter (BA2) and sent to the TIRF lens (L5) and the objective (O).

(B) (Top) beam profile of the ring-shaped gate beam showing on a uniform bead sample. (Bottom) Intensity of the beam in the top image is shown across the yellow dashed line.

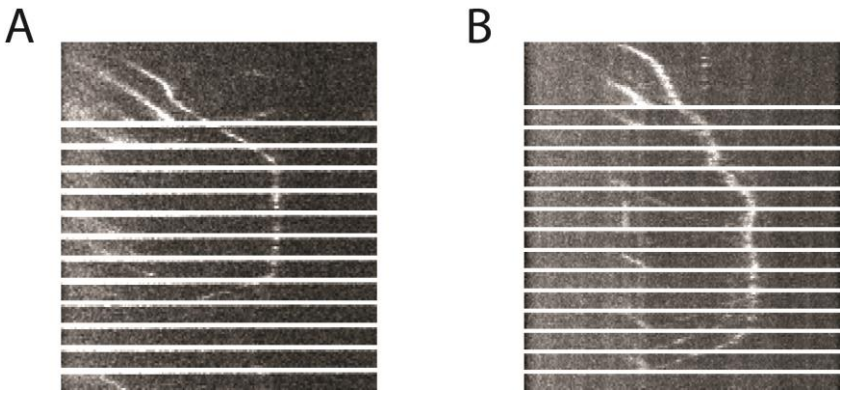


Figure 5.4 Additional Examples of Photobleaching Gate Result on IFT

(A) An example kymograph of the photobleaching gate result, showing an anterograde IFT train return as one retrograde IFT train.

(B) An example kymograph of the photobleaching gate result, showing an anterograde IFT train splits into three retrograde IFT trains at the flagellar tip.

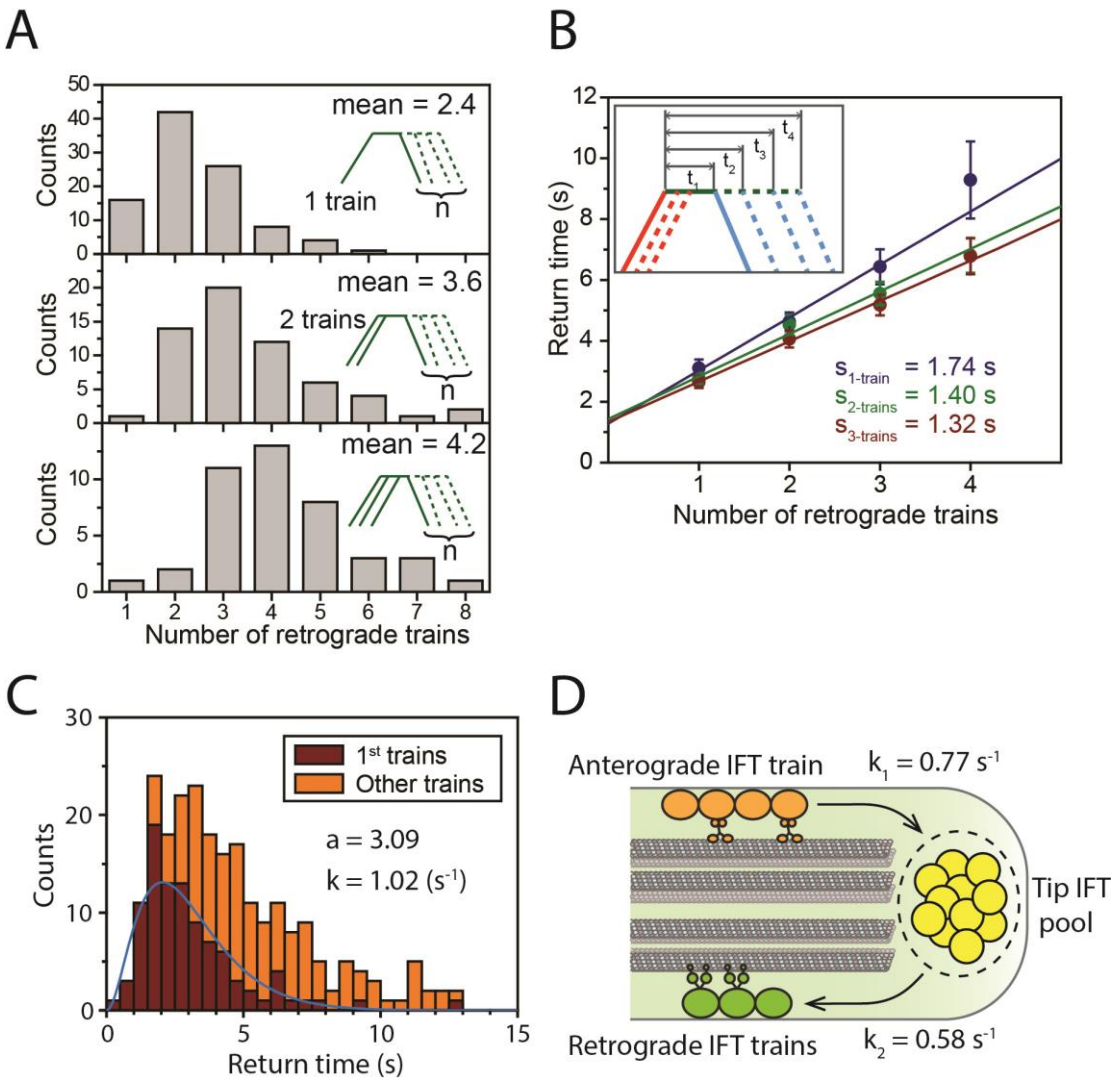


Figure 5.5 Partial mixing of IFT trains at flagellar tips

(A) We allowed one (top), two (middle) and three (bottom) bright anterograde IFT trains to enter the flagellum. The resulting histograms show the numbers of retrograde trains that the fluorescent signal appears on.

(B) (Insert) Return time of 1st, 2nd, 3rd and 4th retrograde IFT trains (t_1, t_2, t_3, t_4) generated by one (blue), two (green), and three (brown) anterograde IFT trains (mean ± sem) arriving at the tip.

(C) Return time histogram of IFT trains. The histogram of the first returning IFT trains is fitted by a gamma distribution (green line).

(D) A model for IFT remodeling. A single anterograde IFT train enters the pool of IFT particles located at the flagellar tip. The train is distributed into multiple retrograde trains assembled by a mixture of trains from the pool follow at a rate of $k_1 = 0.77\ s^{-1}$. Assembled retrograde trains enter the flagellum following a two-step process with a combined rate of $k_2 = 0.58\ s^{-1}$

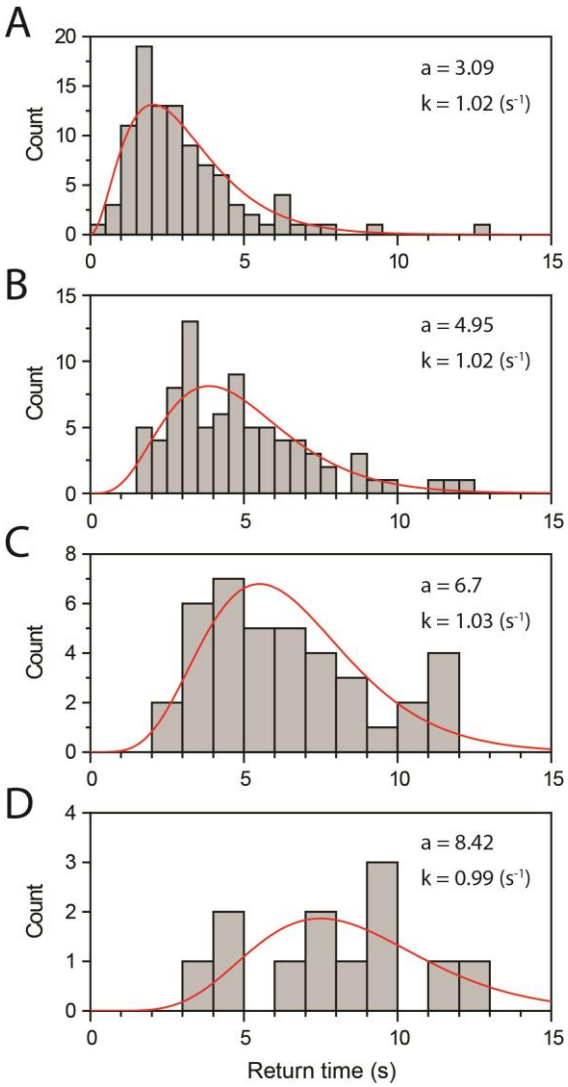


Figure 5.6 Modeling the IFT Return Time

(A) After allowing a single bright anterograde train to enter the flagellum, the return time of the first returning train fit into a gamma distribution with a shape parameter of 3.09.

(B) After allowing a single bright anterograde train to enter the flagellum, the return time of the first returning train fit into a gamma distribution with a shape parameter of 4.95.

(C) After allowing a single bright anterograde train to enter the flagellum, the return time of the first returning train fit into a gamma distribution with a shape parameter of 6.7.

(D) After allowing a single bright anterograde train to enter the flagellum, the return time of the first returning train fit into a gamma distribution with a shape parameter of 8.42.

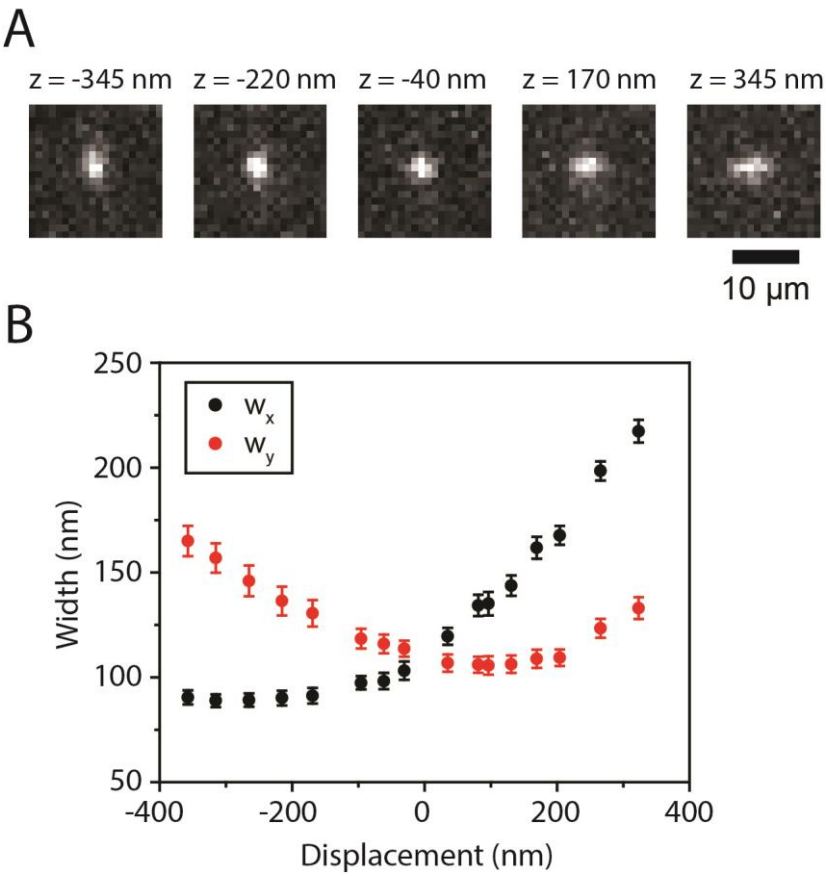


Figure 5.7 Calibration of the Cylindrical Lens

The widths of the PSF in both X and Y directions are measured at different Z position sampled by moving the objective over a range of 800 nm.

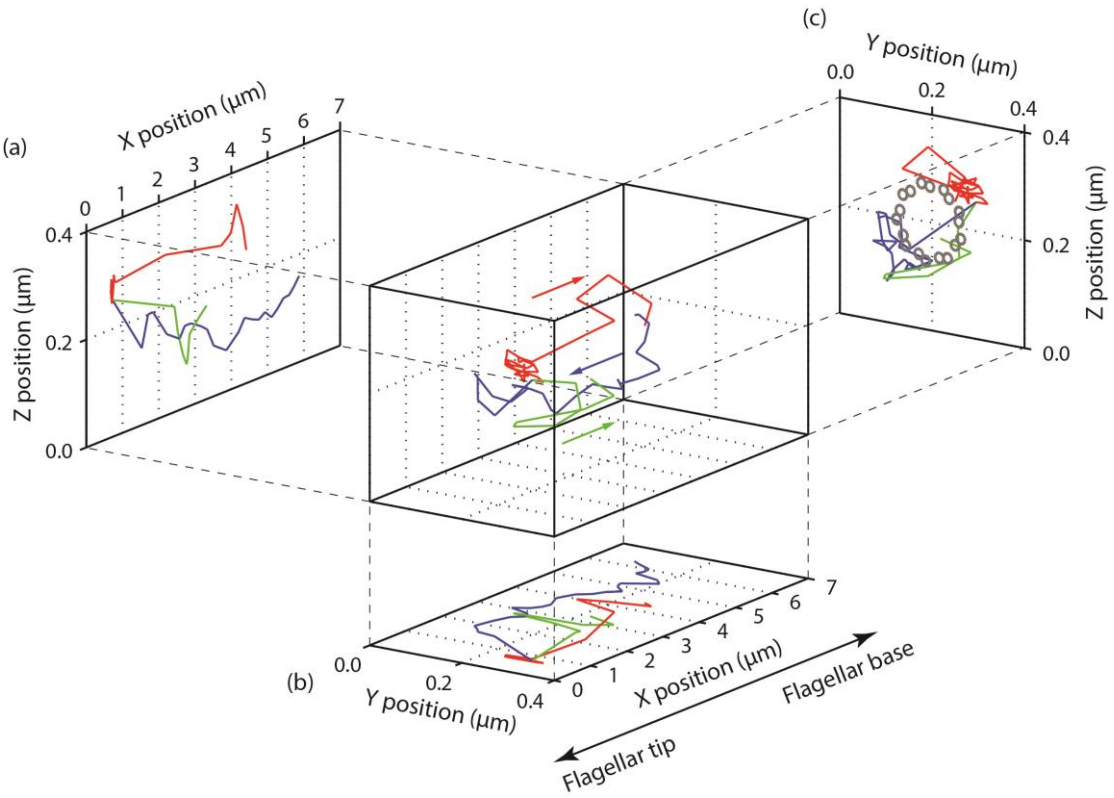


Figure 5.8 Sub-diffraction Limited Detection of IFT Trains

(A) 3D trajectory of an anterograde IFT train (blue) moving in –x direction and two resulting retrograde IFT trains (red, green) moving in +x direction. The z position was detected by fitting the PSF to obtain the aspect ratio. The data is projected on the xz plane (a), xy plane (b), and yz plane (c).

(B) yz projection of an anterograde IFT train and two resulting retrograde IFT trains showing that they moved on different microtubule doublet tracks.

(C) (D) Schematic drawing showing the tracks the trains moved on the cross section.

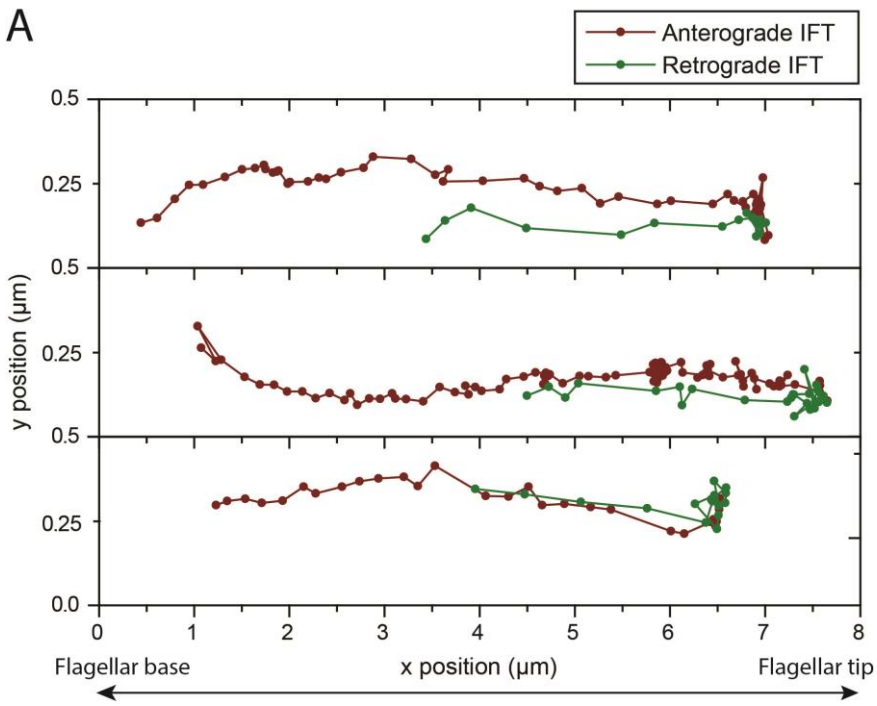


Figure 5.9 Additional Examples for High resolution Tracking of IFT27

Sub-diffraction limited positioning of IFT27-GFP on three individual cells. In the top and middle example, retrograde IFT trains return on different microtubule doublets than the ones that the anterograde trains moved on. The bottom example show a retrograde IFT train returned along the same lateral position with the anterograde IFT train, possibly on the same microtubule doublet.

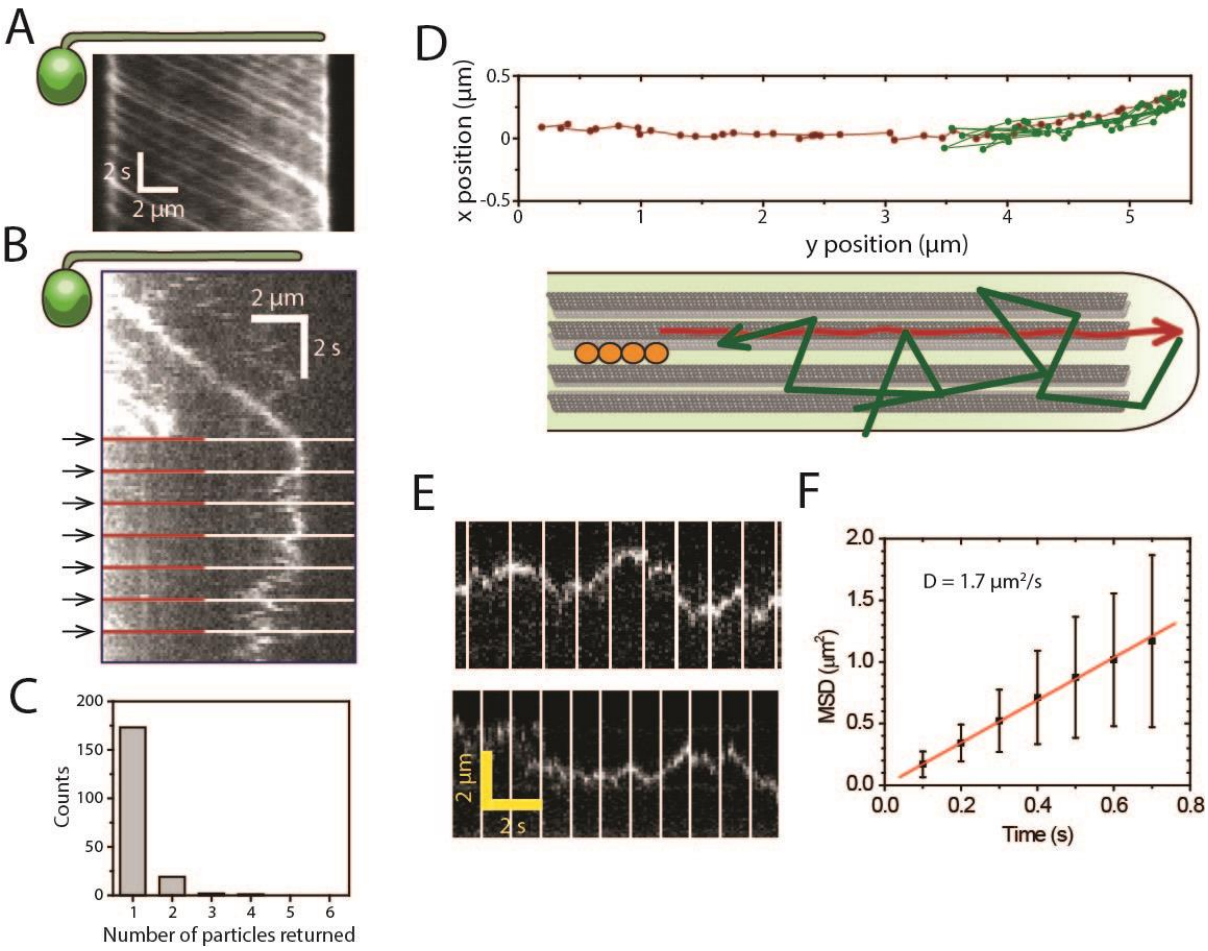


Figure 5.10 Return of single KAP clusters

(A) In a conventional TIRF assay, the KAP subunit of kinesin-2 was observed to move anterogradely, but the retrograde transport of KAP in kymographs was not observed. High GFP background was present in KAP-GFP flagella, increasing towards the tip.

(B) Kymograph analysis of a KAP-GFP cell imaged by the photobleaching gate assay. The KAP subunit of kinesin-2 undergoes active transport in the anterograde direction, pauses at the flagellar tip, and diffuses back to the flagellar base. Arrows indicate the bleaching events.

(C) KAP subunits release at the tip from IFT trains and diffuse in flagella without splitting.

(D) (Top) Trajectory of a KAP cluster moving from the flagellar base to the tip and diffusing back toward the flagellar base. (Bottom) Schematic drawing of a KAP cluster moving along a microtubule in the anterograde direction and diffusing back free in the flagellum .

(E) Two traces of single KAP clusters diffusing along the flagella.

(F) Mean squared displacement analysis of KAP movement after it leaves the flagellar tip (N = 27). The average diffusion constant is 1.7 $\mu m^2/s$.

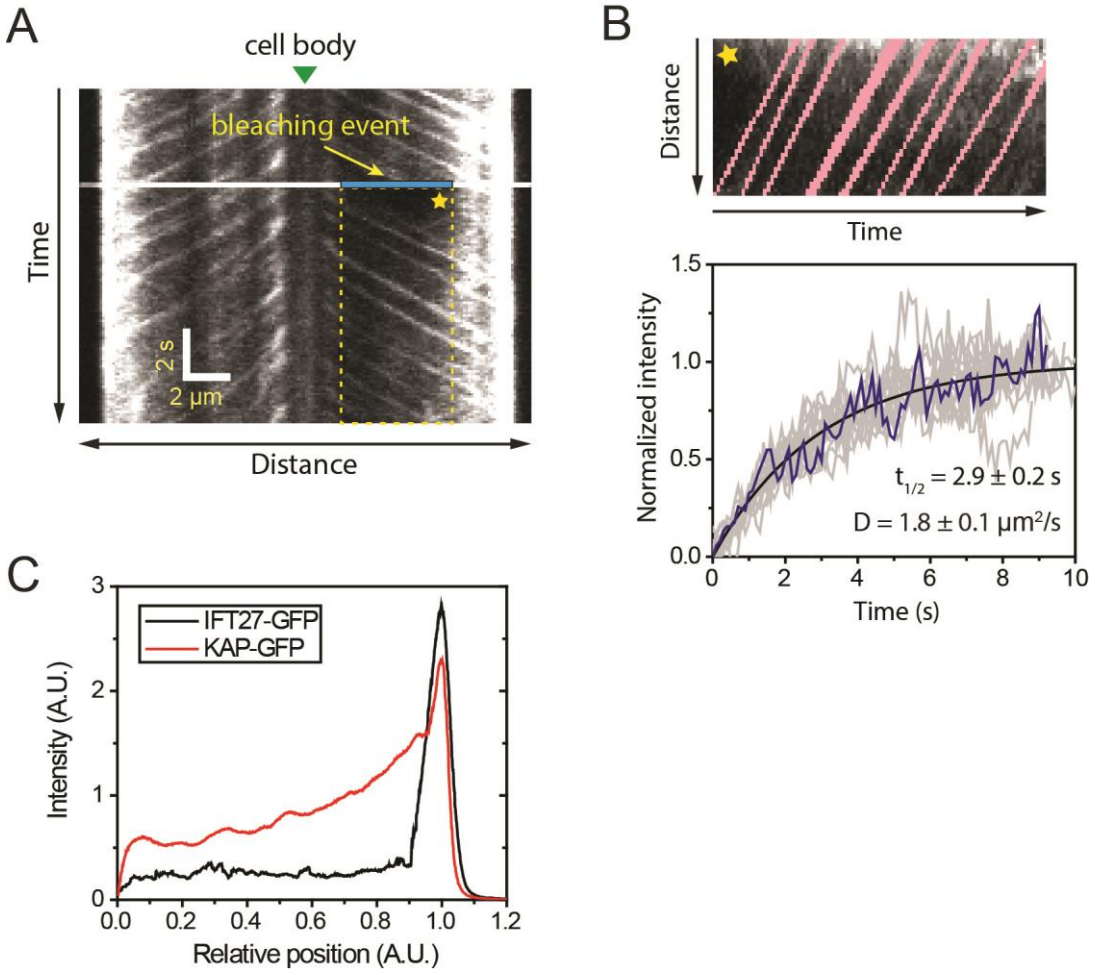


Figure 5.11 Measuring Diffusion Constant of KAP by the FRAP Assay

(A) Kymograph of KAP-GFP movement before and after photobleaching the middle section of the flagellum (blue area). While directed movement of KAP was evident from the flagellar base, the recovery of fluorescence from the tip region was due to diffusion of the GFP background (Movie S2).

(B) (Top) The GFP signal of anterograde traces (red) were manually subtracted from the rectangular area surrounded by yellow dashed line in (D). (Bottom) The intensity in the photobleached area shows recovery as a function of time (blue line). The average recovery signal of 13 cells (grey lines) was fitted to a one-dimensional diffusion equation (solid black line) with a half-time of 2.9 ± 0.2 s.

(C) The average GFP background intensity of KAP-GFP and IFT27-GFP cells along the length of a flagellum, after the removal of anterograde and retrograde transport traces from the kymographs.

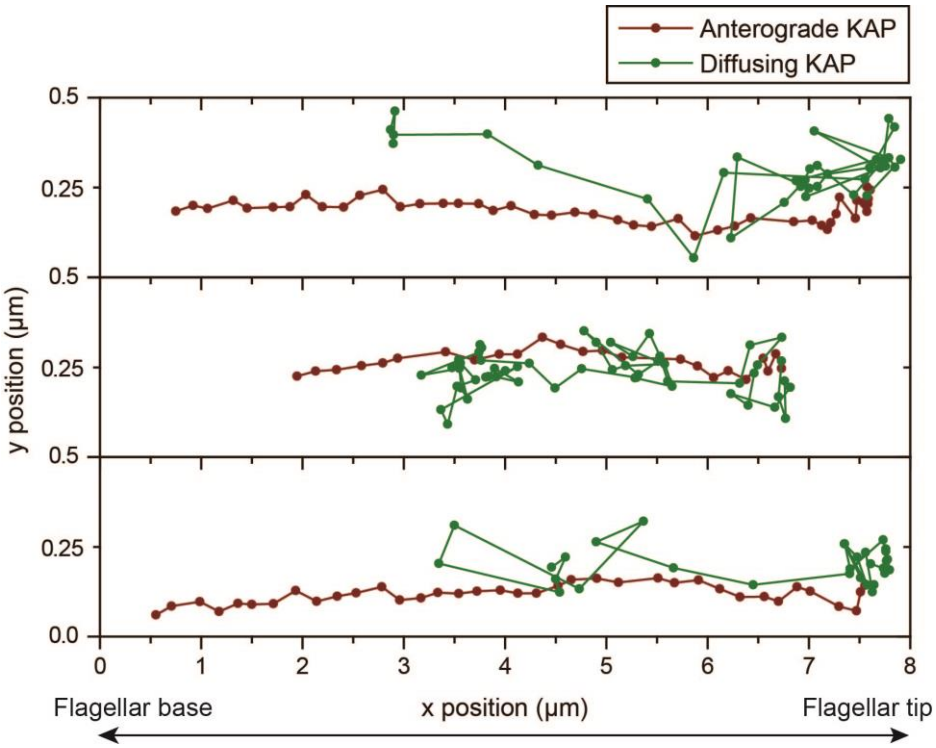


Figure 5.12 Additional Examples for High-resolution Tracking of KAP

Sub-diffraction positioning of KAP-GFP on three individual cells showing the returning KAP diffuses freely within the flagella.

References

Betzig, E. et al. Imaging intracellular fluorescent proteins at nanometer resolution. *Science* 313, 1642-1645 (2006).

Bloodgood, R.A. Motility occurring in association with the surface of the *Chlamydomonas* flagellum. *J Cell Biol* 75, 983-989 (1977).

Bloodgood, R.A. Flagellar surface motility: gliding and microsphere movements. Methods *Cell Biol* 47, 273-279 (1995).

Bloodgood, R.A. The *Chlamydomonas* Flagellar Membrane and Its Dynamic Properties. In "*The Chlamydomonas Sourcebook: Cell Motility and Behavior*", Vol 3, 2nd edn (San Diego, Academic Press) (2009).

Bloodgood, R.A., and Salomonsky, N.L. Calcium influx regulates antibody-induced glycoprotein movements within the *Chlamydomonas* flagellar membrane. *J Cell Sci* 96 (Pt 1), 27-33 (1990).

Bloodgood, R.A., and Salomonsky, N.L. The transmembrane signaling pathway involved in directed movements of Chlamydomonas flagellar membrane glycoproteins involves the dephosphorylation of a 60-kD phosphoprotein that binds to the major flagellar membrane glycoprotein. *J Cell Biol* 127, 803-811 (1994).

Bloodgood, R.A., and Salomonsky, N.L. Microsphere attachment induces glycoprotein redistribution and transmembrane signaling in the *Chlamydomonas* flagellum. . *Protoplasma* 202, 76-83 (1998).

Brunnbauer, M. et al. Regulation of a heterodimeric kinesin-2 through an unprocessive motor domain that is turned processive by its partner. *Proc Natl Acad Sci* U S A 107, 10460-10465 (2010).

Cole, D.G. et al. *Chlamydomonas* kinesin-II-dependent intraflagellar transport (IFT): IFT particles contain proteins required for ciliary assembly in Caenorhabditis elegans sensory neurons. *J Cell Biol* 141, 993-1008 (1998).

Deacon, S.W. et al. Dynactin is required for bidirectional organelle transport. *J Cell Biol* 160, 297-301 (2003).

Dentler, W. Intraflagellar transport (IFT) during assembly and disassembly of *Chlamydomonas* flagella. *J Cell Biol* 170, 649-659 (2005).

DeWitt, M.A., Chang, A.Y., Combs, P.A., and Yildiz, A. Cytoplasmic dynein moves through uncoordinated stepping of the AAA+ ring domains. *Science* 335, 221-225 (2012).

Dymek, E.E., Goduti, D., Kramer, T., and Smith, E.F. A kinesin-like calmodulin-binding protein in *Chlamydomonas*: evidence for a role in cell division and flagellar functions. *J Cell Sci* 119, 3107-3116 (2006).

Engel, B.D. et al. A cell-based screen for inhibitors of flagella-driven motility in *Chlamydomonas* reveals a novel modulator of ciliary length and retrograde actin flow. *Cytoskeleton* (Hoboken) 68, 188-203 (2011).

Engel, B.D, et al. The role of retrograde intraflagellar transport in flagellar assembly and function. *J Cell Biol* 199, 151-167 (2012).

Engel, B.D., Ludington, W.B., and Marshall, W.F. Intraflagellar transport particle size scales inversely with flagellar length: revisiting the balance-point length control model. *J Cell Biol* 187, 81-89 (2009).

Ferris, P.J. et al. Plus and minus sexual agglutinins from *Chlamydomonas* reinhardtii. Plant *Cell* 17, 597-615. (2005).

Gennerich, A., Carter, A.P., Reck-Peterson, S.L., and Vale, R.D. Force-induced bidirectional stepping of cytoplasmic dynein. *Cell* 131, 952-965 (2007).

den Hartigh, J.C., van Bergen en Henegouwen, P.M., Verkleij, A.J. & Boonstra, J. The EGF receptor is an actin-binding protein. *J Cell Biol* 119, 349-355 (1992).

Helenius, J. et al. The depolymerizing kinesin MCAK uses lattice diffusion to rapidly target microtubule ends. *Nature* 441, 115-119, (2006).

Hendricks, A.G. et al. Motor coordination via a tug-of-war mechanism drives bidirectional vesicle transport. *Curr Biol* 20, 697-702 (2010).

Hoffman, J.L., and Goodenough, U.W. Experimental dissection of flagellar surface motility in *Chlamydomonas*. *J Cell Biol* 86, 656-665 (1980).

Huang, B., Wang, W., Bates, M. and Zhuang, X. Three-dimensional super-resolution imaging by stochastic optical reconstruction microscopy. *Science* 319, 810-813 (2008).

Huang, K. et al. Function and dynamics of PKD2 in *Chlamydomonas* reinhardtii flagella. *J Cell Biol* 179, 501-514. (2007).

Iomini, C., Babaev-Khaimov, V., Sassaroli, M., and Piperno, G. Protein particles in *Chlamydomonas* flagella undergo a transport cycle consisting of four phases. *J Cell Biol* 153, 13-24 (2001).

Ishikawa, H., and Marshall, W.F. Ciliogenesis: building the cell's antenna. Nat Rev *Mol Cell Biol* 12, 222-234 (2011).

Jamison, D.K. et al. Two kinesins transport cargo primarily via the action of one motor: implications for intracellular transport. *Biophys J* 99, 2967-2977 (2010).

Jewett, T.J., and Sibley, L.D. Aldolase forms a bridge between cell surface adhesins and the actin cytoskeleton in apicomplexan parasites. *Mol Cell* 11, 885-894 (2003).

Klar, T.A. et al. Fluorescence microscopy with diffraction resolution barrier broken by stimulated emission. *Proc Natl Acad Sci U S A* 97, 8206-8210 (2000).

Kner, P. et al. Super-resolution video microscopy of live cells by structured illumination. *Nat Methods* 6, 339-342 (2009).

Kozminski, K.G., Beech, P.L., and Rosenbaum, J.L. The *Chlamydomonas* kinesin-like protein FLA10 is involved in motility associated with the flagellar membrane. *J Cell Biol* 131, 1517-1527 (1995).

Kozminski, K.G., Johnson, K.A., Forscher, P., and Rosenbaum, J.L. A motility in the eukaryotic flagellum unrelated to flagellar beating. *Proc Natl Acad Sci U S A* 90, 5519-5523 (1993).

Kuzmenko, A. et al. Single molecule tracking fluorescence microscopy in mitochondria reveals highly dynamic but confined movement of Tom40. *Sci Rep* 1, 195 (2011).

Laib, J.A., Marin, J.A., Bloodgood, R.A., and Guilford, W.H. The reciprocal coordination and mechanics of molecular motors in living cells. *Proc Natl Acad Sci U S A* 106, 3190-3195 (2009).

Lecuit, T., Lenne, P.F., and Munro, E. Force generation, transmission, and integration during cell and tissue morphogenesis. *Annu Rev Cell Dev Biol* 27, 157-184 (2011).

Leduc, C., Ruhnow, F., Howard, J., and Diez, S. Detection of fractional steps in cargo movement by the collective operation of kinesin-1 motors. *Proc Natl Acad Sci U S A* 104, 10847-10852 (2007).

Low-Nam, S.T. et al. ErbB1 dimerization is promoted by domain co-confinement and stabilized by ligand binding. *Nat Struct Mol Biol* 18, 1244-1249 (2011).

Matsuura et al. Kinesin-II is not essential for mitosis and cell growth in *Chlamydomonas*. *Cytoskeleton* 52, 195-201 (2002).

Mallik, R. et al. Building complexity: an in vitro study of cytoplasmic dynein with in vivo implications. *Curr Biol* 15, 2075-2085 (2005).

Morone, N. et al. Three-dimensional reconstruction of the membrane skeleton at the plasma membrane interface by electron tomography. *J Cell Biol* 174, 851-862 (2006).

Mueller, J. et al. The FLA3 KAP subunit is required for localization of kinesin-2 to the site of flagellar assembly and processive anterograde intraflagellar transport. *Mol Biol Cell* 16, 1341-1354 (2005).

Nan, B. et al. Myxobacteria gliding motility requires cytoskeleton rotation powered by proton motive force. *Proc Natl Acad Sci U S A* 108, 2498-2503 (2011).

Ou, G. et al. Functional coordination of intraflagellar transport motors. *Nature* 436, 583-587 (2005).

Pan, J., and Snell, W.J. Kinesin-II is required for flagellar sensory transduction during fertilization in *Chlamydomonas*. *Mol Biol Cell* 13, 1417-1426 (2002).

Pazour, G.J., Agrin, N., Leszyk, J., and Witman, G.B. Proteomic analysis of a eukaryotic cilium. *J Cell Biol* 170, 103-113 (2005).

Pazour, G.J., Dickert, B.L., and Witman, G.B. The DHC1b (DHC2) isoform of cytoplasmic dynein is required for flagellar assembly. *J Cell Biol* 144, 473-481 (1999).

Pazour, G.J., Wilkerson, C.G., and Witman, G.B. A dynein light chain is essential for the retrograde particle movement of intraflagellar transport (IFT). *J Cell Biol* 141, 979-992 (1998).

Pedersen, L.B., Geimer, S., and Rosenbaum, J.L. Dissecting the molecular mechanisms of intraflagellar transport in *Chlamydomonas*. *Curr Biol* 16, 450-459 (2006).

Pigino, G. et al. Electron-tomographic analysis of intraflagellar transport particle trains in situ. *J Cell Biol* 187, 135-148 (2009).

Piperno, G., and Mead, K. Transport of a novel complex in the cytoplasmic matrix of *Chlamydomonas* flagella. *Proc Natl Acad Sci U S A* 94, 4457-4462 (1997).

Porter, M.E. et al. Cytoplasmic dynein heavy chain 1b is required for flagellar assembly in *Chlamydomonas*. *Mol Biol Cell* 10, 693-712 (1999).

Qin, H., Diener, D.R., Geimer, S., Cole, D.G., and Rosenbaum, J.L. Intraflagellar transport (IFT) cargo: IFT transports flagellar precursors to the tip and turnover products to the cell body. *J Cell Biol* 164, 255-266 (2004).

Qin, H., Wang, Z., Diener, D., and Rosenbaum, J. Intraflagellar transport protein 27 is a small G protein involved in cell-cycle control. Curr Biol 17, 193-202 (2007).

Reits, E.A. & Neefjes, J.J. From fixed to FRAP: measuring protein mobility and activity in living cells. *Nat Cell Biol* 3, E145-147 (2001).

Rosenbaum, J.L., and Witman, G.B. Intraflagellar transport. Nat Rev Mol Cell Biol 3, 813-825 (2002).

Rust, M.J., Bates, M. & Zhuang, X. Sub-diffraction-limit imaging by stochastic optical reconstruction microscopy (STORM). *Nat Methods* 3, 793-795 (2006).

Shih, S.M. et al. Intraflagellar transport drives flagellar surface motility. *Elife* 2, e00744 (2013).

Shubeita, G.T. et al. Consequences of motor copy number on the intracellular transport of kinesin-1-driven lipid droplets. *Cell* 135, 1098-1107. (2008).

Signor D. et al. Role of a class DHC1b dynein in retrograde transport of IFT motors and IFT raft particles along cilia, but not dendrites, in chemosensory neurons of living Caenorhabditis elegans. *J Cell Biol* 147, 519–530 (1999).

Sun, M. et al. Motor-driven intracellular transport powers bacterial gliding motility. *Proc Natl Acad Sci U S A* 108, 7559-7564 (2011).

Vale, R.D. The molecular motor toolbox for intracellular transport. *Cell* 112, 467-480 (2003).

Vershinin, M. et al. Multiple-motor based transport and its regulation by Tau. *Proc Natl Acad Sci U S A* 104, 87-92 (2007).

Yildiz, A. et al. Myosin V walks hand-over-hand: single fluorophore imaging with 1.5-nm localization. *Science* 300, 2061-2065 (2003).